1·0

2·8

2·5

3·15

2·2

3·5

1·1

4·0

2·0

4·5

1·8

1·25

1·4

1·6

NATIONAL BUREAU OF STANDARDS
MICROCOPY RESOLUTION TEST CHART

AD-A154 149

An Investigation Of The Irradiation Swelling Mechanisms In Refractory Metals At High Temperatures

Phase I Report

Prepared For

AIR FORCE OFFICE OF SCIENTIFIC RESEARCH

Contract No. F49620-83-C-0120

FEBRUARY 1985

DTIC
ELECT
MAY 2 0 1985

B

DTIC FILE COPY

Westinghouse
Advanced Energy Systems Division
Large, P.O. Box 10864, Pittsburgh, PA 15236

DISCLAIMER

The views and conclusions contained in this document are
those of the authors and should not be interpreted as necessarily
representing the official policies or endorsements, either expressed
or implied, of the Air Force Office of Scientific Research
or the U.S. Government.

REPORT DOCUMENTATION PAGE

1a. REPORT SECURITY CLASSIFICATION Unclassified		1b. RESTRICTIVE MARKINGS	
2a. SECURITY CLASSIFICATION AUTHORITY		3. DISTRIBUTION/AVAILABILITY OF REPORT	
2b. DECLASSIFICATION/DOWNGRADING SCHEDULE		Unclassified Approved for public release; distribution unlimited.	
4. PERFORMING ORGANIZATION REPORT NUMBER(S) WAESD-TR-85-005		5. MONITORING ORGANIZATION REPORT NUMBER(S) AFOSR-TR- 85-0378	
6a. NAME OF PERFORMING ORGANIZATION Westinghouse-Advanced Energy Systems Division	6b. OFFICE SYMBOL (If applicable)	7a. NAME OF MONITORING ORGANIZATION Air Force Office of Scientific Research	
6c. ADDRESS (City, State and ZIP Code) P.O. Box 10864 Pittsburgh, PA 15236		7b. ADDRESS (City, State and ZIP Code) Bolling Air Force Base, DC 20332 (AFSC)	
8a. NAME OF FUNDING/SPONSORING ORGANIZATION Air Force Office of Scientific Research	8b. OFFICE SYMBOL (If applicable)	9. PROCUREMENT INSTRUMENT IDENTIFICATION NUMBER F49620-83-C-0120	

8c. ADDRESS (City, State and ZIP Code) Bolling Air Force Base, DC 20332	10. SOURCE OF FUNDING NOS			
	PROGRAM ELEMENT NO. 61102F	PROJECT NO. 2301	TASK NO. A7	WORK UNIT NO. N/A

11. TITLE *Include security Classification*) An Investigation of the Irradiation Swelling Mechanisms in Refractory Metals at High Temperatures Unclassified

12. PERSONAL AUTHOR(S) R. Bajaj, B.O. Hall and G.R. Fenske

13a. TYPE OF REPORT Final	13b. TIME COVERED FROM 1983 TO 1984	14. DATE OF REPORT (Yr., Mo., Day) Feb. 1985	15. PAGE COUNT 110

16. SUPPLEMENTARY NOTATION

17. COSATI CODES			18. SUBJECT TERMS (Continue on reverse if necessary and identify by block number)
FIELD	GROUP	SUB. GR.	Swelling, Radiation Effects, Ion Bombardment, Refractory Metals, Theory of Swelling, Ion-Simulation Irradiation

19. ABSTRACT (Continue on reverse if necessary and identify by block number)

This report presents the results of progress made during the first year of a three year program on the investigation of swelling mechanisms in refractory metals irradiated at elevated temperatures, i.e. $0.3 T_m - 0.6 T_m$ (where T_m = melting point in K). The objective of this work is to achieve an understanding of the elevated temperature swelling in these body centered cubic (bcc) metals by a close coupling of theoretical development and experimental verification.

20. DISTRIBUTION/AVAILABILITY OF ABSTRACT UNCLASSIFIED/UNLIMITED ☐ SAME AS RPT ☐ DTIC USERS ☐	21. ABSTRACT SECURITY CLASSIFICATION	
22a. NAME OF RESPONSIBLE INDIVIDUAL MAJ HENRY L. Pugh	22b. TELEPHONE NUMBER (Include Area Code) 202/767-4900	22c. OFFICE SYMBOL NP

DD FORM 1473, 83 APR EDITION OF 1 JAN 73 IS OBSOLETE

19. Abstract Contd.

During this period, a theoretical model based on the chemical reaction rate formalism was developed specifically for bcc metals. Calculations were performed for niobium, which was subsequently chosen for the experimental work based on theoretical, experimental and practical considerations. A special Nb ion source material was developed which produced Nb ions of sufficient energy and flux to permit, for the first time, ion bombardment of niobium with self-ions. A series of irradiations with 5.3 MeV Nb^{++} ions at temperatures ranging from 700°C to 1200°C were performed at the Argonne National Laboratory.

At a nominal dose of 50 dpa and a dose rate of approximately 6×10^{-3} dpa/s swelling was observed over a temperature range of 700° to 1200°C with peak swelling of 7% at 900°C. Comparison of these experimental results with previous investigations suggested that the use of Ni ions in earlier irradiations may account for the observed difference in the data.

The microstructural data, obtained from transmission electron microscopy (TEM) were compared to the predictions of the theoretical model. A reasonable agreement was obtained between experimental measurements of swelling and theoretical predictions by adjusting both the niobium-oxygen binding energy and the incubation dose for swelling to realistic values. Sink-strength ratios were also calculated from the data. The theory-experiment comparison indicated a need for further investigation in the areas of microstructural evolution at low dose, kinetics of cavity growth, and trapping effects due to oxygen.

AN INVESTIGATION OF THE IRRADIATION SWELLING

MECHANISMS IN REFRACTORY METALS AT HIGH TEMPERATURES
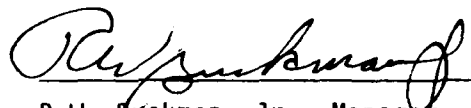
FINAL TECHNICAL REPORT

R. Bajaj

B.O. Hall

G.R. Fenske

Approved by: _____

S.A. Shiels, Manager

Materials Science

R.W. Buckman, Jr., Manager

Materials Technology

C.R. Adkins, Manager

Technology Department

Prepared for the Air Force Office of Scientific Research (AFSC)

Under Contract

F49620-83-C-0120

February 1985

Westinghouse Electric Corporation

Advanced Energy Systems Division

P.O. Box 10864

Pittsburgh, PA 15236

AN INVESTIGATION OF IRRADIATION SWELLING MECHANISMS
IN REFRACTORY METALS AT HIGH TEMPERATURES

R. Bajaj
Westinghouse Advanced Energy Systems Division

B.O. Hall
Westinghouse Research Laboratories

G.R. Fenske
Argonne National Laboratories

A-I

TABLE OF CONTENTS

Page

TABLE OF CONTENTS (Continued)

LIST OF FIGURES

LIST OF FIGURES (Continued)

LIST OF TABLES

ABSTRACT

This report presents the results of progress made during the first year of a
three year program on the investigation of swelling mechanisms in refractory
metals irradiated at elevated temperatures, i.e. $0.3\ T_m - 0.6\ T_m$ (where
T_m = melting point in K). The objective of this work is to achieve an
understanding of the elevated temperature swelling in these body centered
cubic (bcc) metals by a close coupling of theoretical development and
experimental verification.

During this period, a theoretical model based on the chemical reaction rate
formalism was developed specifically for bcc metals. Calculations were
performed for niobium, which was subsequently chosen for the experimental work
based on theoretical, experimental and practical considerations. A special Nb
ion source material was developed which produced Nb ions of sufficient energy
and flux to permit, for the first time, ion bombardment of niobium with
self-ions. A series of irradiations with 5.3 MeV Nb^{++} ions at temperatures
ranging from 700°C to 1200°C were performed at the Argonne National Laboratory.

At a nominal dose of 50 dpa and a dose rate of approximately 6×10^{-3} dpa/s
swelling was observed over a temperature range of 700° to 1200°C with peak
swelling of 7% at 900°C. Comparison of these experimental results with
previous investigations suggested that the use of Ni ions in earlier
irradiations may account for the observed difference in the data.

The microstructural data, obtained from transmission electron microscopy (TEM)
were compared to the predictions of the theoretical model. A reasonable
agreement was obtained between experimental measurements of swelling and
theoretical predictions by adjusting both the niobium-oxygen binding energy
and the incubation dose for swelling to realistic values. Sink-strength
ratios were also calculated from the data. The theory-experiment comparison
indicated a need for further investigation in the areas of microstructural
evolution at low dose, kinetics of cavity growth, and trapping effects due to
oxygen.

1.0 INTRODUCTION AND BACKGROUND

Refractory metals and their alloys offer distinct advantages for applications in nuclear systems where high temperatures are required because they exhibit high elevated temperature strength, better corrosion resistance in liquid metal coolants and better thermophysical properties than other structural materials. In applications where high temperatures are accompanied by high neutron fluxes, these materials are expected to experience swelling which is caused by the agglomeration of irradiation induced vacancies into cavities and by the production of gaseous transmutation products such as helium. Unfortunately swelling data for these materials are limited, also current theoretical treatments of swelling are not directly applicable to refractory metals since they were developed for face centered cubic (fcc) rather than body centered cubic (bcc) materials.

Recognizing the need for a mechanistic swelling model applicable to refractory metals, a three year research program was developed with the objective of achieving an understanding of the swelling phenomenon that would apply to all bcc metals. This program builds upon the understanding of swelling in fcc materials, which have been studied extensively since the first discovery of voids in stainless steel [1], and also on the available swelling information for refractory metals and their alloys.

In the experimental area, this program adopts the techniques of self-ion irradiations developed for austenitic, iron and nickel based alloys. This report summarizes the available literature on refractory metal swelling, details the development of the theoretical model and the experimental techniques and presents the experimental data generated in the first year of the program. The results of incorporating the data into the theoretical model are given and recommendations are made for work during the follow up phases of the program.

1

2.0 PROGRAM OBJECTIVE

The primary objective of this program is to further the understanding of high temperature (from $0.3\ T_m$ - $0.6\ T_m$) cavity swelling and microstructural response of refractory metals to neutron irradiation. The ultimate goal is to acquire a theoretical understanding of swelling and through this to demonstrate the practicality of a low swelling alloy for elevated temperature service. This goal will be achieved by a close coupling of theory development and controlled experimental studies. The neutron-induced swelling will be simulated by single and dual ion irradiations with self-ions, and self-ions plus helium, respectively.

3.0 SIMULATION TECHNIQUES

Over the last ten years, techniques have been developed for simulating neutron irradiation damage in small, transmission electron microscopy (TEM) size specimens. These techniques have been developed to a high degree of sophistication[5-9] and have been proven to be very useful in alloy design and modeling of microstructural evolution and swelling. Simulation techniques offer several advantages over in-reactor irradiations:

(a) They can be performed ex-reactor. Heavy ion bombardment is used to produce the simulated neutron damage. Ion bombardment can be performed at a number of accelerator facilities around the country.

(b) Irradiation times for a specific dose are three to four orders of magnitude shorter.

(c) Irradiation variables such as dose rate, temperature, helium to displacement-per atom ratio (He/dpa) can be varied in a controlled manner.

(d) The technique is significantly less expensive than in-reactor irradiations.

(e) The irradiated specimens are not radioactive.

The versatility of the simulation method is of major importance in the type of work proposed here since a wide variation in irradiation conditions can be achieved and can be tailored to investigate specific aspects of theoretical models.

An important modification to the heavy ion bombardment technique is the use of self-ions. Although difficult to accomplish for refractory metals, the use of self-ions prevents the possibility of chemical interactions which might influence swelling behavior.

A second modification proposed in this work is the simultaneous bombardment of the specimens with self-ions and helium. In earlier work the specimens were pre-injected with helium to simulate the transmutation-produced gas. More recently it was realized that nucleation of cavities and subsequent micro-structural evolution in pre-injected specimens differ significantly from that in specimens under simultaneous bombardment.

In this work the displacement damage produced by the energetic neutrons is simulated by high energy (5-6 MeV) self ions, and the transmutation produced helium is simulated by irradiating the specimen simultaneously with a beam of high energy self-ions and a beam of helium ions. The energy of the latter is adjusted so that the displacement damage and the deposition of helium occur in the same location in the specimen.

4.0 REVIEW OF IRRADIATION TESTS ON REFRACTORY METALS

The refractory alloy systems are based on vanadium, niobium, molybdenum, tantalum and tungsten. Swelling in these metals has received much less attention than in the austenitic materials, although some attention has been given to these metals because of their potential use in fusion reactors. Most of the studies have been limited to relatively low temperatures and the information in the range of 0.4-0.6 T_m is scant. The other drawbacks of these studies are that they deal with existing alloys or metals of uncontrolled purity and the ion irradiation studies utilized heavy ions of foreign metal (e.g., Ni in V, Ta in Mo) rather than self-ions. This latter factor clouds the

results of these studies, since foreign atoms are deposited in the damage region introducing microstructural features, such as precipitates, which would not be present in a neutron irradiation. Dual-ion irradiation data of refractory metals are very limited as shown below. In the following section, high temperature ion and neutron swelling results of Mo, Nb, V, Ta and W and their alloys are presented. Earlier studies on helium pre-injected or uninjected specimens are also included.

4.1 Vanadium

High purity vanadium was neutron irradiated by Weber et al.[10] at temperatures from 600° to 750°C (0.4 to 0.46 T_m) to damage levels from 1 to 5 dpa. Voids and precipitates of vanadium carbide, VC, were observed. The voids increased in size and decreased in density with increasing temperature. At the peak swelling temperature of 650°C, a swelling of 2.5% was observed at 5 dpa. It was recommended that carbon contamination be minimized to avoid VC precipitation.

Agarwal and Taylor[11] irradiated high purity vanadium with vanadium ions at 650° and 700°C to 55 dpa and found the swelling fraction increased at first, attained a maximum (2% at 34 dpa), and decreased with increasing dose. The reduced swelling was explained on the basis of a change in bias due to precipitates requiring excess vacancies for accommodation. The effects of interstitial impurities were very significant in the study of vanadium.

In another study (on self-ion irradiated, pre-injected vanadium), Agarwal et al.,[12] showed that nitrogen was most effective in controlling swelling with carbon and oxygen showing smaller effects. Fine precipitation was observed in specimens doped with C and O. The observations were analyzed in terms of solute segregation theory.

Santhanam et al.[13] investigated the effects of impurities and pre-injected helium content (10 and 100 ppm) on swelling of high purity and commercial vanadium ion irradiated with Ni ions at temperatures from 650°- 850°C (0.42 T_m to 0.51 T_m) to ~60 dpa. A maximum void swelling of 3.5% was observed

4

in commercial purity vanadium containing 10 appm He. The voids were cubic and their concentration was an order of magnitude larger in commercial purity material than high purity material at 650° and 700°C. The voids were smaller in the commercial purity material, however. The peak swelling temperatures (700°C for high purity and 750°C for commercial purity) coincided with the temperature at which precipitates were first observed. The effect of helium was significant only at 750°C (0.46 T_m) where the swelling decreased with increasing helium content. It was postulated that bubbles were formed by prior annealing at 750°C for one hour and acted as predominant sinks and competed with dislocations, thus causing low swelling. Also, it was suggested that helium bubbles were not good void nuclei in vanadium.

Lott et al.,[14] investigated the effect of substitutional nickel and interstitial nitrogen on vanadium bombarded with Cu^{+++} ions without the presence of helium at relatively low temperatures of 450° to 650°C (0.26 to 0.34 T_m). Both of these elements reduced swelling in vanadium. It was suggested that the reduction in swelling was caused by precipitation phenomena observed in nickel doped specimens. The precipitation increased the density of unbiased sinks and enhanced recombination. In the nitrogen doped specimens, it was speculated that the small black dot (dislocation loop) damage caused the same effects as the precipitates.

In studies of neutron irradiated vanadium, Bressers and van Witzenberg[15] irradiated single crystal and polycrystalline vanadium at 400°-800°C (0.31 - 0.49 T_m), after doping with 850 appm oxygen, to a fluence of 2.5 x 10^{22} n/cm^2 (E>1 MeV). A maximum swelling of 0.14% was observed in doped poly-crystalline material. The effect of interstitial oxygen was greatest in the annealed single crystals and at the higher temperature range. Void lattice formation was not observed in any of the specimens.

Tyler and Goodhew[16] conducted annealing studies on helium pre-implanted vanadium, to study the bubble growth mechanism. Isothermal anneals were conducted for times up to 100 h at 950°C. Bubbles produced during annealing were faceted. It was concluded that the growth of bubbles occurred by migration and coalescence. The rate limiting parameter was impurity sensitive nucleation of atomic ledges on the bubble facets.

The alloys of vanadium were evaluated in both the U.S. and West Germany as candidate cladding materials for LMFBRs, and are currently being evaluated for use in fusion devices. As a result, there are more vanadium alloy data at elevated temperatures than for any other refractory alloy.

Van Witzenberg et al.[17] investigated the effects of preimplanted-helium (up to 1000 ppm) on neutron irradiated vanadium and V-Cr-Ti alloys. The irradiations were carried out to 4.5×10^{22} n/cm^2 (E > 0.1 MeV) at a low temperature of 540°C (0.37 T_m). Helium caused decreased swelling and void concentrations and increased void sizes in pure vanadium irrespective of concentration, in qualitative agreement with oxygen in the previous study. In V-Cr-Ti, the opposite effect was found. Helium increased the void concentration and decreased the size irrespective of concentration. The swelling, however, was less in V-Cr-Ti than in pure vanadium with or without helium. The differences were explained on the basis of the critical cavity concept.

A number of vanadium alloys have been investigated in simulation tests to determine swelling behavior. These studies, reviewed by Gold et. al.[18], have concentrated on the V-Ti-Cr system which has shown a general resistance to void swelling in alloys containing titanium. In V-10Cr alloy, a maximum of 1% swelling was observed at a fluence of 1.5×10^{22} n/cm^2 at irradiation temperatures of 700 and 800°C. The VANSTAR-7 alloy has shown very low swelling. For alloys containing titanium, irradiated at temperatures from 470° to 780°C to fluences as high as 6×10^{22} n/cm^2, little or no swelling was observed.

The V-20 Ti composition is highly swelling resistant, however injection of 90-200 appm of helium results in void formation during subsequent neutron irradiation[19]. The swelling was low however, of the order of 0.03%, after 3×10^{22} n/cm^2. Recent ion bombardment experiments show that V-Cr binary alloys swell more than unalloyed vandium while alloys containing Ti were completely swelling resistant[20], thus confirming the swelling resistance of Ti containing vanadium alloys for the range of ion bombardment temperatures 400° to 700°C, and damage levels to 50 dpa.

6

4.2 Niobium

In uninjected niobium and its alloys irradiated with Ni ions, Loomis et al.,[21,22] found void swelling between 600° and 1150°C (0.31 T_m and 0.52 T_m respectively) with peak swelling occurring at 0.4 T_m in Nb and ~1025°C (0.47 T_m) in Nb-1 Zr. Oxygen impurities reduced the swelling, promoted void ordering and increased void nucleation.

Loomis and Gerber[23] irradiated niobium and its binary and ternary alloys with dual beams of Ni^+ and He^+ at temperatures as high as 950°C (0.47 T_m) and showed that Fe and Ni impurities that diffuse rapidly in Nb have a minor influence on swelling whereas those (e.g., Mo) that diffuse slowly decrease the swelling. Elements that getter oxygen (e.g., Ti) decreased the swelling, suggesting a strong role of oxygen in swelling in niobium.

Jang and Moteff[24] neutron irradiated Nb-1 Zr to 1×10^{22} n/cm^2 at temperatures varying from 430° to 1050°C (0.26 T_m to 0.48 T_m) and found void swelling at all temperatures. A maximum of 2% swelling was observed at 800°C (a shift of ~200°C from ion data) at this relatively low dose. The swelling was analyzed in terms of reaction rate theory with a good agreement.

Bartlett et al[25] reported results of swelling in Nb-5Zr and Nb-10Zr irradiated to a fluence of 3.6×10^{22} n/cm^2 at 450° to 600°C. They found no significant amount of swelling for any condition, although a few voids were observed for the irradiation at 550° and 600°C.

4.3 Tantalum

Unalloyed tantalum showed swelling under neutron bombardment between 400° and 1000°C[26]. At a fluence of approx. 2.5×10^{22} n/cm^2, a swelling of 2.5% was observed.[27] Murgatroyd[28] found swelling in tantalum irradiated at 500°C, however, the swelling decreased with increasing fluence. This recovery was attributed to the shrinkage of voids due to the transmutation of Ta to W, with a resulting reduction in lattice parameter.

Swelling in tantalum alloys has received little attention. No swelling was observed in T-111 irradiated at 450° and 600°C. The Ta-10W alloy showed some voids, but swelling was less than in the unalloyed metal.[29]

4.4 Molybdenum

Brimhall and Simonen[30] studied swelling in uninjected Mo single crystals at temperatures up to 900°C (0.4 T_m) by ion bombardment with 7.5 MeV Ta^{+++} ions to doses as high as 150 dpa. A void swelling of ~2% was observed at the highest dose. They found a maximum in void concentration occurring at relatively low dose and further swelling occurred by void growth. The dose dependence of swelling was less than linear. Void ordering was also observed.

Simonen and Brimhall[31] analyzed the swelling data on Mo irradiated to 1000°C (0.44 T_m) and concluded that he voids act as unbiased sinks. In another study, Bradley and Brimhall[32] found a good correlation between swelling with Ni ions and that with neutrons when the temperature shift was included. They also found little effect of free surfaces on the ion bombarded specimens of Mo single crystals.

Recently, Brimhall, et al.[33] irradiated Mo at high temperature (0.44 T_m) in a dual beam facility and injected Ta^{+++} and He^+ ions simultaneously to dose of 80 dpa. Simultaneous injection of helium caused continuous nucleation of voids. The helium had little effect on the absolute magnitude of the swelling which was approximately 0.5%, and the dose dependence was similar to neutron irradiations at low dose levels.

The effect of an oversized atom (Zr) on void swelling at 700°-900°C in Mo was investigated by Liou, et al.[34] Zr appeared to reduce the stacking fault energy and ease loop nucleation. Solute-defect flux coupling caused precipitation of an incoherent phase.

Stubbins and Moteff[35] studied Mo and its alloys irradiated at the highest temperatures to 1425°C (~0.55T_m). Their study on the uninjected Mo and TZM (an alloy with Ti, Zr and Mo) metal showed increasing swelling with increasing

temperatures. The dose dependence of swelling varied with temperature and was different in different alloys. Over a temperature range of 850°-1000°C, TZM showed lower swelling than Mo-0.5Ti; also swelling in TZM showed less temperature dependence than in Mo-0.5Ti alloy.

In Mo and its alloys, neutron irradiated from 330° to 850°C to fluences of 1 and 3×10^{20} n/cm^2, Bentley, et al.[36,37] observed voids at all temperatures, and void growth with increasing temperature. In TZM, however, void shrinkage was observed at 750° and 850°C and the damage structure consisted of dislocation loops and almost a complete absence of voids. A strong influence of impurities with damage structure was envisaged, with oversize alloying elements segregating to the dislocation core. Pard and Garr[38] irradiated TZM to 8×10^{22} n/cm^2 (E > 0.1 MeV); however, their temperatures of irradiation were low and very little void swelling was observed. Sprague et al.[39] and Gelles et al.[40] also studied low temperature (650°C, 0.32 T_m) swelling in Mo and its alloys. A value of 3% swelling was found in Mo at a fluence of 5.4×10^{26} n/cm^2 (E > 0.1 MeV) by Sprague et al. Gelles et al. reported a swelling of 3% in TZM alloy at a fluence of 1.47×10^{23} n/cm^2 (E > 0.1 MeV); however saturation was not predicted until 10^{24} n/cm^2 with 20% swelling.

4.5 Tungsten

Tungsten and its alloys have received the least amount of attention of the five refractory alloy systems. Neutron irradiated tungsten showed swelling over the temperature range of 450° to 1300°C (0.2 to 0.43 T_m). Matolich et. al.[41] observed swelling of approx. 2% at 750°C, however increasing swelling was suggested at temperatures > 1200°C.

A tungsten-rhenium (W-25Re) alloy examined after a range of irradiation conditions showed no swelling.[42] No void formation was observed in W containing 5 to 25% Re irradiated to a fluence of 4 to 5×10^{21} n/cm^2 at temperatures from 600°-1500°C.

A recent review paper by Wiffen[43] provides an excellent review of irradiation effects data in refractory metals.

4.6 Conclusions on the State of the Art of Refractory Metal Irradiation Data

From the literature survey of swelling in bcc refractory metals, it is clear
that no controlled and systematic study is available from which to draw any
definite conclusions on the swelling mechanisms in these metals. In addition,
the data base on high temperature swelling under controlled conditions is
meager at best. The present work is intended to fill the gap existing in the
understanding of high temperature swelling in these materials.

5.0 SELECTION OF MATERIAL FOR STUDY

The technologically important refractory metals can generally be classified
into two groups: i.e. Group V metals, vanadium, niobium and tantalum, and Group
VI metals, molybdenum and tungsten. All were considered in the selection of a
model material. The choice was based on three major considerations; (1)
theoretical, (2) experimental, and (3) practical i.e., those related to the
engineering application of these materials. In making the choice of material,
the third consideration was weighted less than the first two.

The theoretical considerations involved the availability of the parameters
needed for theoretical modelling of the swelling phenomenon. These parameters
are related to dislocation bias, point defect diffusivities, sink strengths,
binding energies, vacancy and interstitial migration and formation energies.
In addition, an important consideration was the probability of formation of
<100> loops. Based on these latter considerations V, Nb and Mo were more
desirable than Ta and W.

Among the experimental factors considered were the availability of a self-ion
beam with sufficient ion current in an energy range of 4   8 MeV, the depth of
penetration of the incoming self-ion, and susceptibility to contamination
during the irradiation. These considerations favored niobium over all of the
other candidates, since ion beams of sufficient current can be obtained using a
novel approach which is described in Section 6. Peak damage due to self-ions
in Nb occurs at a depth of approximately 1 μm, which is considered suffi-
ciently removed from the surface to avoid surface sensitive effects. Also, the

only other candidate material, V is very susceptible to contamination during ion irradiation. Ta, Mo and W were rejected because ion currents of sufficient intensity could not be obtained and because the penetration depth is limited due to their high atomic weights.

Practical or applications oriented considerations favored Nb and Ta because alloys of these materials can be utilized up to high temperatures, 1200° and 1350°C, respectively, whereas V alloys are only usable to < 800°C. W and Mo can be used at high temperatures, however fabrication of their alloys is difficult and they undergo a transition from ductile to brittle behavior at relatively high temperatures, especially in the irradiated condition.

Based on these considerations niobium was chosen as the material for study. Table I summarizes the matrix used to make the selection of material for study.

Model calculations, which predict the swelling in niobium are provided in the next section.

TABLE I
Summary of Choice of Material Considerations

Metal	Theoretical	Experimental	Practical
V	0	X	X
Nb	0	0	0
Ta	X	X	0
Mo	0	X	X
W	X	X	X

0-Favorable
X-Less Favorable

11

6.0 DEVELOPMENT OF A THEORETICAL MODEL FOR REFRACTORY METALS

Since the discovery of voids in irradiated stainless steel by Cawthorne and Fulton[1] in 1967, there has been considerable study of void and cavity nucleation and growth in metals. Classical steady-state nucleation theory has been extended to treat nucleation when supersaturations of both vacancies and interstitials are present, and has been used to calculate nucleation rates for various irradiation conditions.[44-46] Time dependent nucleation models, based on the chemical reaction rate formalism, have also been developed to predict nucleation rate as a function of time.[47,48] Experimental data suggest that the classical separation of cavity evolution into nucleation and growth regimes is not a bad approximation, and theoretical models have been developed to predict growth of an average void or cavity after nucleation is complete.[49,50] These growth models have recently been expanded to include equations that describe higher moments of the cavity size distribution function.[51]

Although the details of crystal structure are not emphasized in rate-theory model development, calculations are generally performed for face centered cubic metals and have been quite successful in reproducing qualitative trends in the experimental data, including the temperature dependence of the nucleation and growth behavior, the general form of the size distribution function, nucleation times, and gross impurity effects. Little attention, on the other hand, has been given to body centered cubic metals. In these metals, differences in the migration and formation energies of vacancies and interstitials, in surface energies, in development of the loop microstructure, and in impurity inter- actions can give rise to significant differences in cavity growth and swelling behavior. The purpose of the present work is to develop a cavity growth model specifically for body centered cubic metals and to calculate growth rates and swelling behavior in refractory metals. The results of this effort are pre- sented in this section.

6.1 Point-Defect Concentrations

The rate equations for the concentrations of point defects - vacancies and interstitials -- can be written as

$$\underset{\sim}{\nabla} \cdot (D_v \underset{\sim}{\nabla} C_v + \frac{D_v C_v}{kT} \underset{\sim}{\nabla} U_v) + G_v - RC_v C_I - K_v C_v = \frac{\partial C_v}{\partial t} \tag{1}$$

and

$$\underset{\sim}{\nabla} \cdot (D_I \underset{\sim}{\nabla} C_I + \frac{D_I C_I}{kT} \underset{\sim}{\nabla} U_I) + G_I - RC_v C_I - K_I C_I = \frac{\partial C_I}{\partial t} \tag{2}$$

where the subscripts I and v denote interstitials and vacancies, D is a diffusion coefficient, C is concentration of point defects per unit volume, k is Boltzmann's constant, T is absolute temperature, U is the interaction energy of point defects with a sink, G is a point defect production rate per unit volume, R is the recombination coefficient, and K is a reaction rate constant. Time-dependent solutions of Eqs. (1) and (2) can be obtained using standard numerical techniques. Treatment of void swelling, however, does not require this, since the relaxation times for changes in the point defect concentrations are short when compared with those required to change the microstructure. A quasi-steady-state condition is generally assumed to hold, and the time derivatives are neglected. A second approximation that is invoked to simplify the problem is that the real material with its set of inhomogeneous sinks can be replaced by a continuum with a uniform sink distribution whose integrated effect on the point defect concentrations is the same as that of the discrete set. The spatial derivatives in Eqs. (1) and (2) are then eliminated, and an analytic solution can be obtained for the quasi-steady-state point defect concentrations:

$$C_v = \frac{[K_I K_v + R(G_I - G_v)]}{2RK_v} \left(\left\{ 1 + \frac{4RG_v K_I K_v}{[K_I K_v + R(G_I - G_v)]^2} \right\}^{1/2} - 1 \right) \tag{3}$$

$$C_I = -\frac{[K_I K_v + R(G_v - G_I)]}{2RK_I} \left(\left\{ 1 + \frac{4RG_I K_I K_v}{[K_I K_v + R(G_I - G_v)]^2} \right\}^{1/2} - 1 \right) \tag{4}$$

The steady-state defect concentrations obtained from Eqs. (3) and (4) are functions of the point-defect production rates G_I and G_v and the sink strengths, K_I and K_v, which are determined by the microstructure. They

13

enter the rate equations that describe the microstructural evolution as
parameters that are self-consistently adjusted as the microstructure changes
with time.

6.1.1 Sink Strengths

The model material is assumed to contain a variety of sinks for point defects:
network dislocations (nd), interstitial dislocation loops (ℓ), cavities (c),
precipitates (p), and grain boundaries (gb). The strength S_j of a given sink j
is that quantity that, when multiplied by the point defect diffusion coeffi-
cient and concentration, gives the loss rate of defects to the sink. S_j is
generally written as the product of three factors: a geometric parameter
describing the sink, a capture efficiency Z_j, and a correction factor that
accounts for interactions between sinks. The expressions that were used for
S_j in the present work are

$$S_{I,v}^{nd} = L Z_{I,v}^{nd} , \tag{5}$$

where L is the network dislocation density;

$$S_{I,v}^{\ell} = 4\pi \ r_\ell^* N_\ell \ Z_{I,v}^{\ell} , \tag{6}$$

where N_ℓ is the loop density and r_ℓ^* is an effective capture radius,
defined by $r_\ell^{*2} = \delta r_\ell/2$, where δ is the dislocation core radius and
r_ℓ is loop radius;

$$S_{I,v}^{c} = 4\pi \ r_c N_c \ Z_{I,v}^{c} \tag{7}$$

where r_c is the cavity radius, and N_c is the cavity density;

$$S_{I,v}^{p} = 4\pi \ r_p N_p \ Z_{I,v}^{p} \tag{8}$$

where r_p is the precipitate radius, and N_p is the precipitate density; and

$$S_{I,v}^{gb} = \frac{6S^{1/2}}{d} , \tag{9}$$

where S is the sum of the strength of all sinks within the grain, and d is the grain diameter.

The capture efficiencies $Z_{I,v}$, which occur in Eqs. (5) through (9), are given by the ratio of the actual point-defect current to the sink to an ideal current, which would result if the sink were a perfect absorber and had no stress field to interact with that of the point defect. Attempts have been made to theoretically evaluate the capture efficiencies for a variety of sink types.[52-55] The problem is a difficult one, however, and these calculations can be criticized because of oversimplifications, invalid approximations, and inconsistencies.[56,57] For numerical calculations, the capture efficiencies are therefore treated as parameters: Z_v for a sink type is generally assumed to be 1, and Z_I for dislocations ranges between roughly 1.02 and 1.5, with Z_I for other sinks assumed to be 1.

The reaction-rate constants $K_{I,v}^{j}$ for each sink are obtained by multiplying the sink strengths by the appropriate point-defect diffusion coefficient:

$$K_{I,v}^{j} = S_{I,v}^{j} \, D_{I,v} , \tag{10}$$

and the rate constants $K_{I,v}$, which appear in the equations for the point defect concentrations, are

$$K_{I,v} = \sum_{j} K_{I,v}^{j}$$

The point-defect diffusion coefficients D_I and D_v are given by

$$D_{I,v} = D_{I,v}^{0} \exp\left[-Q_{I,v}/kT\right] , \tag{12}$$

where $D_{I,v}^{0}$ is the pre-exponential factor, and $Q_{I,v}$ is the activation energy.

15

6.1.2 Defect Production Rates

In many swelling models, the production rates for interstitials and vacancies are assumed to be equal. The steady-state defect concentrations can then be written as

$$C_V = \frac{K_I}{2R} \left(\left\{ 1 + \frac{4RG}{K_I K_V} \right\}^{1/2} - 1 \right) \tag{13}$$

$$C_I = \frac{K_V}{2R} \left(\left\{ 1 + \frac{4RG}{K_I K_V} \right\}^{1/2} - 1 \right) , \tag{14}$$

where $G_I = G_V = G$ is the production rate, and the ratio of concentrations, C_I/C_V, is equal to K_V/K_I. This assumption is valid in certain physical situations, specifically when vacancy loop formation in cascades is negligible and when interstitial injection does not occur. Most generally, the production rates can be written as

$$G_V = (1 - \epsilon_V) G \tag{15}$$

and

$$G_I = (1 + \epsilon_I) G, \tag{16}$$

where ϵ_V is the fraction of vacancies that form vacancy loops and ϵ_I is the fraction of additional interstitials due to self-ion injection. The latter parameter ϵ_I is non-zero only near the end of range, where the implanted ions come to rest.

6.2 Interstitial Dislocation Loops

Interstitial loops observed in body centered cubic metals after irradiation are of two types. The type most frequently found is a perfect loop with $\frac{a}{2}$ <111> Burgers vector and a {111} habit plane.[58-61] After ion or electron irradiation at high temperatures, however, perfect loops with a <100> Burgers vectors and {100} habit planes are seen in α-iron[62] and ferritic alloys.[63]

Eyre and Bullough[64] proposed a mechanism for formation of interstitial
loops in the body centered cubic lattice. They suggested that <110> split
dumbbell interstitials aggregate on {110} planes to form faulted loop nuclei
with $\frac{a}{2}$ <110> Burgers vector. Due to a high stacking fault energy, the loops
unfault by either of two reactions:

$$\frac{a}{2} \; [110] + \frac{a}{2} [1\bar{1}0] \rightarrow a \, [100] \tag{17}$$

or

$$\frac{a}{2} \; [110] + \frac{a}{2} [001] \rightarrow \frac{a}{2} [111] \tag{18}$$
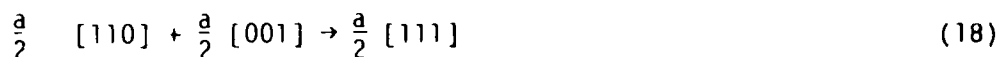
The elastic energy of either product loop is further reduced by a rotation of
the habit plane from {100} and {111} respectively. Bullough and Perrin[65]
verified this model using a computer simulation of the α-iron lattice and
found that $\frac{a}{2}$ <111> loop formation was energetically favored at all irradiation
temperatures. In addition, their results showed that unfaulting occurred at
very small loop sizes, below the resolution limit for conventional trans-
mission-electron microscopy.

Little, Bullough, and Wood[63] have recently used these ideas to explain the
evolution of the damage structure and the observed swelling resistance in FV
448 martensitic stainless steel. After neutron irradiation to damage levels of
30 displacements per atom (dpa) at temperatures in the range 380° to 480°C, a
homogeneous population of loops with a <100> Burgers vector was observed to
exist in domains, which lay within the martensite matrix that retained a high
(preirradiation) network dislocation density. The overall swelling of the
alloy, estimated from measurements of void statistics, was <<0.1%, a value in
agreement with bulk density determinations.[2] The mechanism that Little,
Bullough, and Wood proposed for the observed swelling suppression is based on
theoretical calculations of bias factors for interstitial dislocation
loops.[52-55] According to these calculations, the bias of a dislocation
depends on the magnitude of its Burgers vector. Hence, the bias of an a <100>
type dislocation with $|\underset{\sim}{b}| = a$ is larger than that of an $\frac{a}{2}$ <111> type
dislocation with $|\underset{\sim}{b}| = \sqrt{3} \, a/2$.

The $\frac{a}{2}$ <111> dislocations are relatively neutral sinks when compared with the a <100> dislocations and act to absorb the excess vacancies that would be available for void formation in their absence.

The mechanism of swelling suppression that occurs in the ferritic steels is applicable to the general class of body centered cubic materials, including the technologically important refractory metals such as Nb, Mo, W, V, Ta, and their alloys. The requirements for the mechanism to be effective are (1) the presence of a high initial dislocation density, and (2) a sufficiently high probability for a <100> loop formation. Table II, which was taken from reference (63), contains a list of body centered cubic metals with their lattice parameters, shear moduli, and the relative probability P for <100> loop formation, calculated from

$$P = \exp \left[(E^{<100>} - E^{<111>})/kT \right] , \tag{19}$$

where the loop energies $E^{<100>}$ and $E^{<111>}$ are given by

$$E^{<100>} = \frac{\mu a^3}{4\pi} (\alpha + \sin \alpha) + a^2 \Upsilon (\sin \alpha \cos \alpha - \alpha) \tag{20}$$

Table II

Lattice Parameters, Shear Moduli and Calculated Relative
Probabilities for <100> Loop Formation in a Range of BCC Metals

Metal	Lattice Parameter, a (nm)	Shear Modulus μ (x 10GPa)	Relative Probability, P
Nb	0.330	3.96	4.3×10^{-5}
V	0.304	4.73	5.5×10^{-5}
Fe	0.287	8.60	5.7×10^{-9}
Ta	0.330	7.07	7.9×10^{-11}
Mo	0.315	12.3	1.9×10^{-19}
W	0.317	16.0	1.4×10^{-27}

18

$$E^{<111>} = \frac{\mu a^3}{8\pi} \ (\beta + \sin \beta) + a^2 \Upsilon \ (\sin \beta \cos \beta - \beta), \qquad (21)$$

with

$$\alpha = 2 \sin^{-1} \ (\frac{\mu a}{16\pi\Upsilon})$$

$$\beta = 2 \sin^{-1} \ (\frac{\mu a}{32\pi\Upsilon}) \ ,$$

where a is the lattice parameter, Υ is the stacking fault energy, and μ is the shear modulus.

V and Nb are clearly good candidates for swelling suppression via the loop mechanism, since the probability of <100> loop formation in these metals is roughly four orders of magnitude larger than that for α-iron. In Ta, Mo, and W, the mechanism should be relatively unimportant.

6.2.1 Rate Equations

The differential equations that describe the time evolution of the two types of interstitial loop are

$$\frac{dr_{\ell i}}{dt} = a^2 \ \{Z_I^{\ell i} \ D_I C_I - Z_v^{\ell v} \ D_v \ (C_v - C_{v\ell i}^{th})\} \ . \qquad (22)$$

where $r_{\ell i}$ is the mean radius of the loops of type i.

$C_{v\ell i}^{th}$ is the thermal vacancy concentration at the loop, which is given by

$$C_{v\ell i}^{th} = C_v^{th} \ \exp \ [- \ (\Upsilon + E_{\ell i} - \sigma a) \ a^2/kT], \qquad (23)$$

where C_v^{th} is the bulk thermal vacancy concentration, and σ is the hydro-static stress. The elastic energy $E_{\ell i}$ of a circular loop is given by[66]

$$E_{\ell i} = A_1 \ \{A_2 \ [\ell n \ (p/\delta) - \ell n \ (\pi/4) -2] + A_3\} \ , \qquad (24)$$

where p is the loop perimeter, and

$$A_1 = [\mu p / 4\pi \ (1-\nu)]$$

$$A_2 = [(1-\nu/2) \ (b^2-b_z^2) + b_z^2]$$

$$A_3 = [-(1-2\nu) \ (b^2-b_z^2) + 2(3-2\nu)b_z^2]/8 \ (1-\nu) \ ,$$

where ν is Poisson's ratio, b is the Burgers vector, b_z is the z-component of the Burgers vector, with the z-axis perpendicular to the loop plane, and δ is the dislocation core radius.

6.3 Helium

The presence of helium in a metal during irradiation can have a substantial effect on cavity nucleation.[67,68] It is relatively insoluble, and the binding energy between vacancies and helium atoms is high, of the order of 3 eV. Helium is consequently trapped by small vacancy clusters. The gas then stabilizes the clusters by reducing the vacancy emission rate, and the clusters can grow until they reach the critical size. At this size, the excess flux of vacancies over interstitials is sufficient for continued growth.

The critical cavity size depends on temperature. At low temperatures, clusters with two or three vacancies are stable and the effect of helium is small. At higher temperatures, however, when clusters require ten or more vacancies to be stable, the presence of helium can determine whether cavity formation is possible.

As currently included in the theory of cavity growth the effect of helium is simply to decrease the thermal emission rate of vacancies from the cavity. The gas exerts a pressure opposing the surface tension, and the thermal equilibrium vacancy concentration C_{vc}^{th} at the cavity surface becomes

$$C_{vc}^{th} = C_v^{th} \ \exp \ [-(P_g - 2\Upsilon/r_c) \ \Omega/kT] \ , \tag{25}$$

where P_g is the gas pressure, and Ω is the atomic volume. The decrease in the thermal concentration, as given by Eq. (25), leads to cavity growth at higher temperatures.

Helium can also interact with other components of the microstructure, for example, dislocations and precipitates. Both experimental evidence[69] and theoretical calculations,[51,70] however, indicate that vacancies or cavities are the dominant sink for the gas. In the present work, therefore, helium is assumed to be either mobile and occupying an interstitial site or trapped in a cavity, with the possibility of emission either by thermal detrapping or by knockout. The sink strength S of a cavity for helium is taken by

$$S_{He}^C = 4\pi \ r_c N_c \ . \tag{26}$$

The rate equation that governs the concentration of mobile helium is

$$\frac{dC_{He}}{dt} = \dot{n}_{He} - K_{He}^V \ C_{He} + X \tag{27}$$

for the concentration of free helium, where $\dot{n}_{He}$ is the helium injection rate, K_{He}^V is the reaction rate constant for loss of helium to cavities, and X is the rate at which helium is emitted from cavities. The equation for the concentration of helium trapped in cavities is

$$\frac{dC_{He}^T}{dt} = K_{He}^V \ C_{He} - X \tag{28}$$

The detrapping rate X is given by

$$X = \dot{n}_d + \nu_d C_{He}^T \ , \tag{29}$$

where $\dot{n}_d$ is the radiation displacement rate for helium from cavities, and ν_d is the thermal detrapping rate for a single helium atom.

6.4 Solutes

Solutes that interact with point defects can affect cavity growth in a metal in several ways. The most widely studied phenomenon is that of solute segregation to cavities,[71,72] which occurs because of the coupled diffusion of point defects and solutes to sinks during irradiation. Theoretical calculations have shown that the presence of a solute at the cavity surface can decrease the vacancy capture efficiency of the cavity, leading to a reduction in the growth rate. This effect is difficult to model, however, and has not been substantiated by experimental evidence. It is therefore not included in the present work.

Solutes can also act as traps for either interstitials or vacancies or both types of point defect. As traps, solutes hinder diffusion and change the time scales of the basic nucleation and growth processes. Modification of the basic swelling model to include defect trapping is accomplished by means of an effective diffusion coefficient, D^+, which is given by[73]

$$D_{I,v}^+ = D_{I,v} / [1 + 4\pi C_T R_T D_{I,v} (\tau_T - \tau_H)] \ , \tag{30}$$

where C_T is trap concentration, τ_H is the time spent at a host atom site during the diffusion process, τ_T is the time spent at a trap site, and R_T is the capture radius of the trap. A square-well interaction potential is assumed, with a capture radius equal to a single jump distance. The time τ_T and τ_H are given by

$$\tau_T^{-1} = \nu_T = \nu_0 \exp [-(E_{I,v}^m + E_B)/kT] \tag{31}$$

and

$$\tau_H^{-1} = \nu_H = \nu_0 \exp (-(E_{I,v}^m /kT) \tag{32}$$

where ν_T and ν_H are jump frequencies, ν_0 is the attempt frequency, $E_{I,v}$ are motion energies, and E_B is the solute-point defect binding energy.

Vacancy trapping by solute atoms generally leads to longer incubation times for cavity nucleation and higher cavity number densities.[73] The cavity growth rate is reduced, and total swelling at a fixed fluence is lowered.

6.5 Cavities

The swelling rate $\dot{S}$ is given by

$$\dot{S} = 4\pi \, N_c \, r_c^2 \, \frac{dr_c}{dt} \tag{33}$$

where the time rate of change $\frac{dr_c}{dt}$ of the mean cavity radius r_c is

$$\frac{dr_c}{dt} = \frac{\Omega}{r_c} \, \{Z_v^c \, D_v \, (C_v - C_{vc}^{th}) - Z_I^c \, D_I C_I\} \, , \tag{34}$$

where the thermal vacancy concentration C_{vc}^{th} at the cavity surface is given by Eq. (25).

Eqs. (22), (27), (28), and (34) are the basic set of differential equations for modelling swelling in body centered cubic metals. They can be solved numerically using standard techniques such as those in the GEAR package.[74]

6.6 Calculations for Niobium

As mentioned previously, one of the features that distinguishes the irradiation-induced microstructure in body centered cubic metals from that found in face centered cubic metals is the existence of two types of dislocation loops. The dominant type is of <111> orientation, but <100> loops can also form. The presence of several sinks in the system with positive but differing biases for interstitials complicates the microstructural evolution during irradiation. The relative values of the bias factors for the network dislocations, the <111> loops, and the <100> loops, for example, determine whether <100> loops grow or shrink in a given microstructural environment and affect the cavity growth

23

rate. One purpose of the model was to quantitatively evaluate the effects of the loop bias or preference factors on the loop and cavity growth rates.

A second goal was to numerically assess the effect of helium on cavity growth. As in face centered cubic metals, the presence of helium in sufficient quantity in body centered cubic metals enhances the cavity growth rate and leads to increased swelling. The chemical reaction rate model was used to calculate cavity growth rates for cavities with different gas contents. The growth rates show a clear dependence on the gas content, and the impact of the results on the temperature dependence of cavity swelling in the presence of helium is outlined.

In the following section, numerical results of calculations performed with parameters appropriate for niobium are presented. Values that are used are presented in Table III .

6.7 Results of Calculations

6.7.1 Loop Capture Efficiencies

Calculations were performed to determine the sensitivity of the growth rates of voids and loops to the values assumed for the interstitial capture efficiencies $Z_I^{\ell 1}$ and $Z_I^{\ell 2}$ of the <100> and <111> interstitial dislocation loops. Values of $Z_I^{\ell 1}$ and $Z_I^{\ell 2}$ between 1.0 and 1.3 were considered; the capture efficiency Z_I^{nd} of the network dislocations was held fixed at 1.05, a value that is typically used for modeling work and is supported by experimental data in face centered cubic metals.[18] A listing of the possible cases for values $Z_I^{\ell 1}$ and $Z_I^{\ell 2}$ with respect to each other and to the value of the network capture effi- ciency Z_I^{nd} is given in Table IV and a schematic representation of these these cases is shown in Fig. 1. Theoretical considerations may be used to limit the possibilities. Calculations of bias factors in several approxi- mations[52,82,83] suggest that the capture efficiency of small dislocation

Table III. Parameters for Niobium

Quantity	Value
Lattice parameter, a	3.29×10^{-8} cm [75]
Atomic volume, Ω	1.78×10^{-23} cm^3 [75]
Nearest neighbor distance, d	2.85×10^{-8} cm [75]
Dislocation core radius, δ	2.85×10^{-8} cm
Shear modulus, μ	3.96×10^{11} dynes/cm^2 [76]
Poisson's ratio, ν	0.392 [76]
Surface energy, Υ	2.7×10^3 ergs/cm^2 [63]
Vacancy formation energy, E_v^f	2.53 eV [77,78]
Vacancy migration energy, E_v^m	1.09 eV [77,78]
Vacancy formation prefactor, C_{vo}^{th}	$4/\Omega$
Vacancy diffusion prefactor, D_{vo}	0.008 cm^2/s [78]
Interstitial migration energy, E_I^m	0.115 eV [79]
Interstitial diffusion prefactor, D_{Io}	$10^{13}\, d^2/6$ cm^2/s [77]
Helium migration energy, E_{He}^m	0.2 eV [80]
Helium diffusion prefactor, D_{Heo}	$10^{13}\, d^2/6$ cm^2/s
Helium detrapping frequency, ν_D	$10^{13}\, e^{-\frac{3.8}{kT}}$/s [79]

Table IV. Possible Regimes for Capture Efficiencies (see Fig. 1)

(Condensed notation: $Z_I^{\ell 1} > Z_1$; $Z_I^{\ell 2} = Z_2$; $Z_I^{nd} = Z_n$)

Regime	Definition	Dimensionality
I	$Z_1 = 1$; $Z_2 = 1$	point
IIa	$Z_1 = 1$; $1 < Z_2 < Z_n$	line
IIb	$Z_1 = 1$; $Z_2 = Z_n$	point
IIc	$Z_1 = 1$; $Z_2 > Z_n$	line
IIIa	$Z_2 = 1$; $1 < Z_1 < Z_n$	line
IIIb	$Z_2 = 1$; $Z_1 = Z_n$	point
IIIc	$Z_2 = 1$; $Z_1 > Z_n$	line
IVa	$1 > Z_1 > Z_n$; $Z_2 < Z_1$	area
IVb	$Z_1 = Z_2 < Z_n$	line
IVc	$Z_1 = Z_2 = Z_n$	point
IVd	$1 < Z_1 < Z_n$; $Z_1 > Z_2$	area
IVe	$1 < Z_1 < Z_n$; $Z_2 = Z_n$	line
IVf	$1 < Z_Z < Z_n$; $Z_1 = Z_n$	line
Va	$1 < Z_1 < Z_n$; $Z_2 > Zn$	area
Vb	$Z_1 = Z_n$; $Z_2 > Z_1$	line
VIa	$Z_n < Z_1$; $1 < Z_2 < Z_n$	area
VIb	$Z_n < Z_1$; $Z_2 = Z_n$	line
VIIa	$Z_n < Z_1$; $Z_n < Z_2 < Z_1$	area
VIIb	$Z_n < Z_1$; $Z_2 = Z_1$	line
VIIc	$Z_n < Z_1$; $Z_2 > Z_1$	area
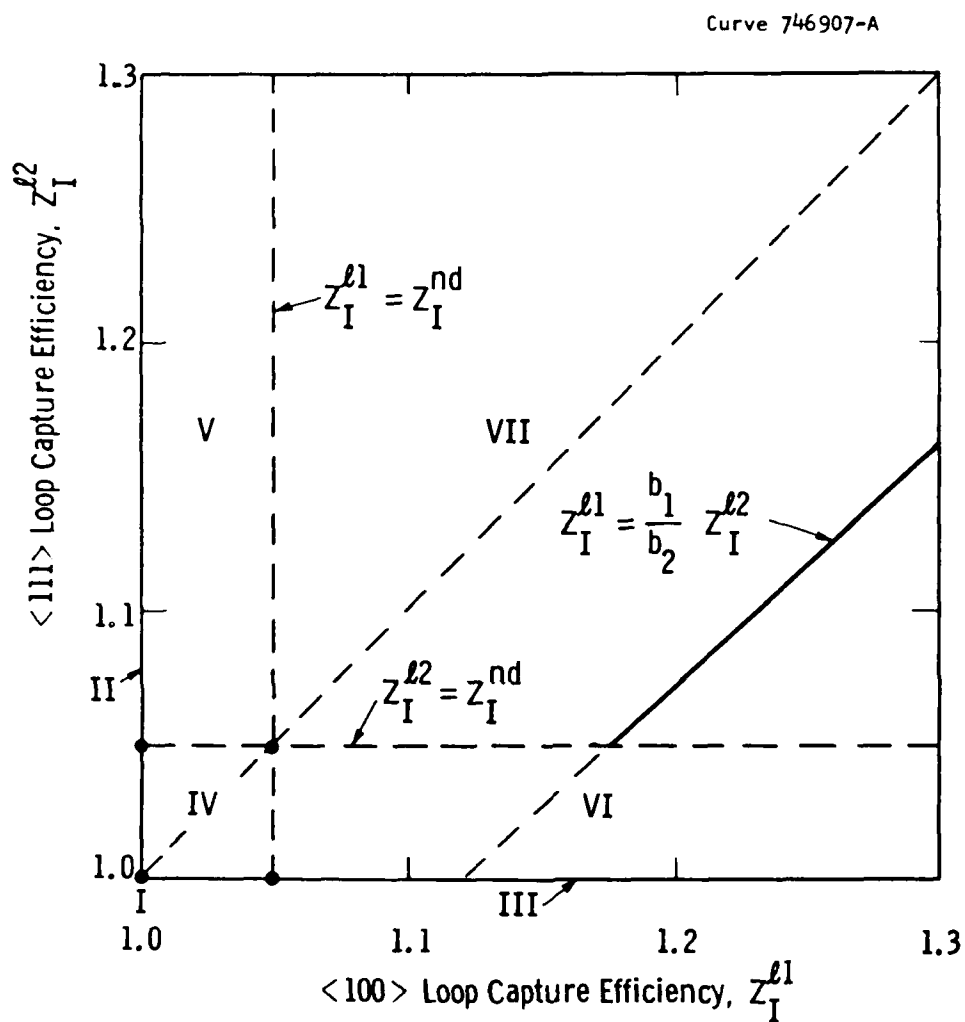
Fig. 1. Schematic of regimes for loop capture efficiencies $Z_I^{\ell 2}$ and $Z_I^{\ell 2}$. Solid line indicates values consistent with current theories.

27

loops is larger than that for network dislocations. In addition, the capture efficiency for a loop is proportional to the magnitude of its Burgers vector $\underline{b}$; one may assume, therefore, that $Z_I^{\ell 1} > Z_I^{\ell 2}$ and, other factors being equal, $Z_I^{\ell 1}/Z_I^{\ell 2} = b_1/b_2$. These two considerations yield potential ($Z_I^{\ell 1}$, $Z_I^{\ell 2}$) values along the solid line in Fig. 1.

It should be noted that calculations of capture efficiencies for loops have been done using approaches and approximations that are subject to criticism. Nichols[57], in a recent review of bias factor calculations, concluded that "bias factor estimates are quantitatively unreliable" and that "bias factors used in swelling analyses must be considered empirical". In light of this conclusion, it is useful to view the bias factor as a model parameter and to determine the range of values that is required to reproduce experimental results -- specifically, the necessary conditions for obtaining growth of <100> loops and shrinkage of <111> loops, as seen in FV 448 steel with a high network dislocation density[84].

According to Eq. (22), the growth rate of an interstitial loop when bias effects dominate depends on the difference between two terms, which represent the two defect fluxes:

$$\frac{dr_{\ell i}}{dt} = a \; (Z_I^{\ell i} D_I C_I - D_v C_v) \tag{35}$$

where $r_{\ell i}$ is the loop radius, $Z_I^{\ell i}$ is the capture efficiency, D is a defect diffusion coefficient, and C is a defect concentration. In a system with four types of sink -- network dislocations, <100> loops, <111> loops, and cavities -- a positive growth rate for a loop requires

$$Z_I^{\ell i} > \frac{S_I}{S_v} \; , \tag{36}$$

where S is a defect sink strength. Equation (36) is obtained from Eq. (35) above and Eqs. (10), (11), (13) and (14).

As defined in Section 5.1.1

$$S_I = LZ_I^{nd} + 4\pi r_{\ell 1}^{*} N_{\ell 1} Z_I^{\ell 1} + 4\pi r_{\ell 2}^{*} N_{\ell 2} Z_I^{\ell 2} + 4\pi r_c N_c \qquad (37)$$

and

$$S_v = L + 4\pi r_{\ell 1}^{*} N_{\ell 1} + 4\pi r_{\ell 2}^{*} N_{\ell 2} + 4\pi r_c N_c \qquad (38)$$

where capture efficiencies for vacancies have been taken as 1 for all sink types, as has the capture efficiency for interstitials at cavities. The notation in Eqs. (37) and (38) is that used before, L is the network density, N is a microstructural defect density, $r_{\ell 1}^{*}$ is an effective capture radius for loops, and r_c is the cavity radius.

When bias effects dominate, the change in cavity radius r_c with time is given by

$$\frac{dr_c}{dt} = \frac{\Omega}{r_c} (D_v C_v - D_I C_I), \qquad (39)$$

and a positive growth rate requires that

$$1 < \frac{S_I}{S_v}. \qquad (40)$$

This condition is obtained in a straightforward manner from Eq. (39) above and Eqs. (10), (11), (13) and (14).

Bias effects determine the cavity growth rate when the thermal vacancy term in Eq. (34) is small and can be neglected. A comparison of the total vacancy concentration with the thermal vacancy concentration is shown as a function of temperature in Fig. 2 for three values of the defect production rate and two values of the network dislocation density. Other parameters that were used: $\dot{n}_{He} = 0$, $N_c = 10^{14}/cm^3$, $N_{\ell 1} = 10^{10}/cm^3$, $N_{\ell 2} = 10^{15}/cm^3$, $Z_I^{nd} = 1.05$, $Z_I^{\ell 1} = 1.176$, $Z_I^{\ell 2} = 1.05$, $r_c = 10^{-7}$ cm, $r_{\ell 1} = 10^{-7}$ cm, and $r_{\ell 2} = 10^{-7}$ cm. From the the figure, it is apparent that the bias-dominated growth regime occurs at low temperatures, and extends toward higher temperatures as either network density decreases or defect production rate increases.

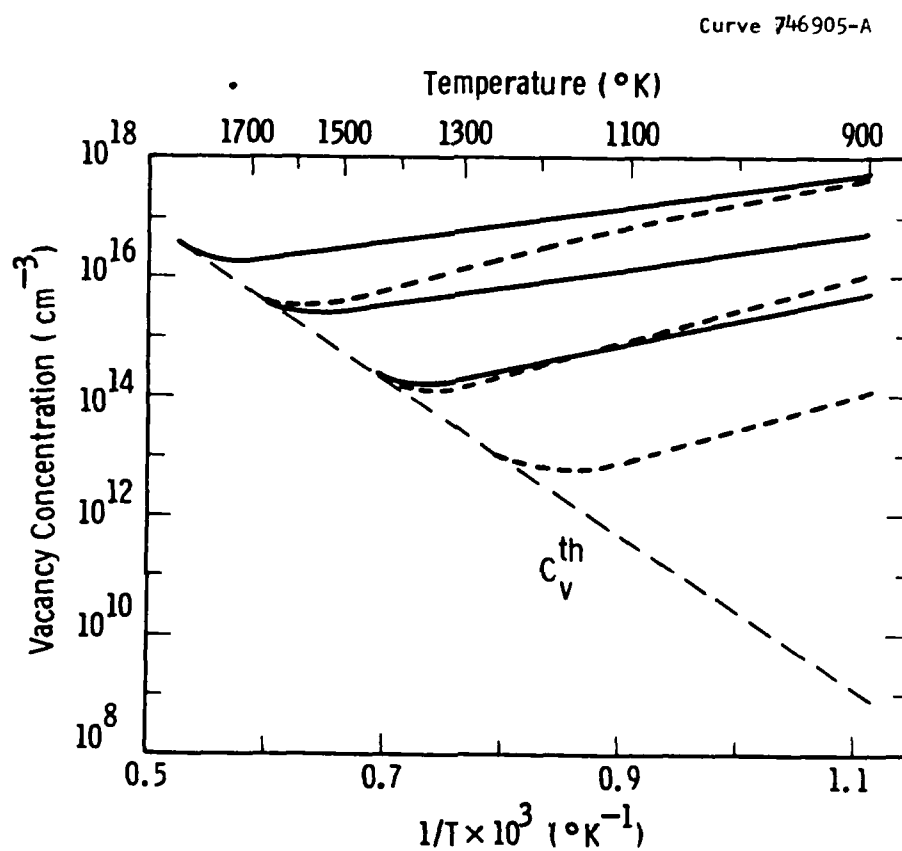Fig. 2.   Vacancy concentration as a function of temperature for
production rates G of 10^{20}, 10^{18}, and 10^{16}/cm^3-s, in
descending order. Solid curves are for network density L =
10^6/cm^2, dashed curves for L = 10^{11}/cm^2.

The growth and shrinkage regimes defined by Eqs. (36) and (40) are illustrated schematically in Fig. 3. It is apparent that the sink strength ratio S_I/S_v must lie between $Z_I^{\ell 2}$ and $Z_I^{\ell 1}$ for <111> loops to shrink and <100> loops to grow. In this region, voids grow.

Equations (36), (37), (38), and (39) can be used to evaluate the values of capture efficiencies necessary for growth, stability or shrinkage of the various microstructural components for a given microstructure. Conversely, for fixed values of the capture efficiencies, the microstructural conditions, parameterized by L, $r^\star_{\ell 1}$, $r^\star_{\ell 2}$, r_c, $N_{\ell 1}$, $N_{\ell 2}$, and N_c, can be varied in order to investigate the possible values of the sink strength ratio, S_I/S_v.

The latter was done for the ranges of microstructural parameters given in Table V. $Z_I^{\ell 1}$ was assumed equal to $b_1 Z_I^{\ell 2}/b_2$ and Z_I^{nd} to 1.05.

Table V. Microstructural Parameters Used for Calculations of Sink Strength Ratio S_I/S_v

Network Density, L	10^8-10^{12}/cm^2
Cavity Density, N_c	10^{13}-10^{18}/cm^3
<100> Loop Density, $N_{\ell 1}$	$10^{-5} N_{\ell 2}$
<111> Loop Density, $N_{\ell 2}$	10^{13}-10^{18}/cm^3
Capture areas, $4\pi r$	10^{-6}cm

The results for S_I/S_v are plotted in Figs. 4 through 6, for $Z_I^{\ell 1}$ equal to 1.02, 1.05, and 1.1 respectively. Although much detail can be extracted from these figures, several general features are important for this analysis. First, since the ranges of microstructural parameters were selected so that all physically observed microstructural densities are included, the results in Figs. 4 through 6 establish the values of the sink strength ratio that are obtainable in practice. These lie, in the three cases considered, between 1.0 and either Z_I^{nd} or $Z_I^{\ell 2}$, whichever is larger. The former is obtained when the network dislocation density and the <111> loop density are relatively low, and the cavity density is high. The upper limit value, if Z_I^{nd}, occurs when the

31

ℓ1 Loops Grow — ℓ1 Loops Shrink

ℓ2 Loops Grow — ℓ2 Loops Shrink

Voids Shrinks — Voids Grow

0 — 1 — $Z_I^{\ell 2}$ — $Z_I^{\ell 1}$

Sink Strength Ratio, S_I/S_V
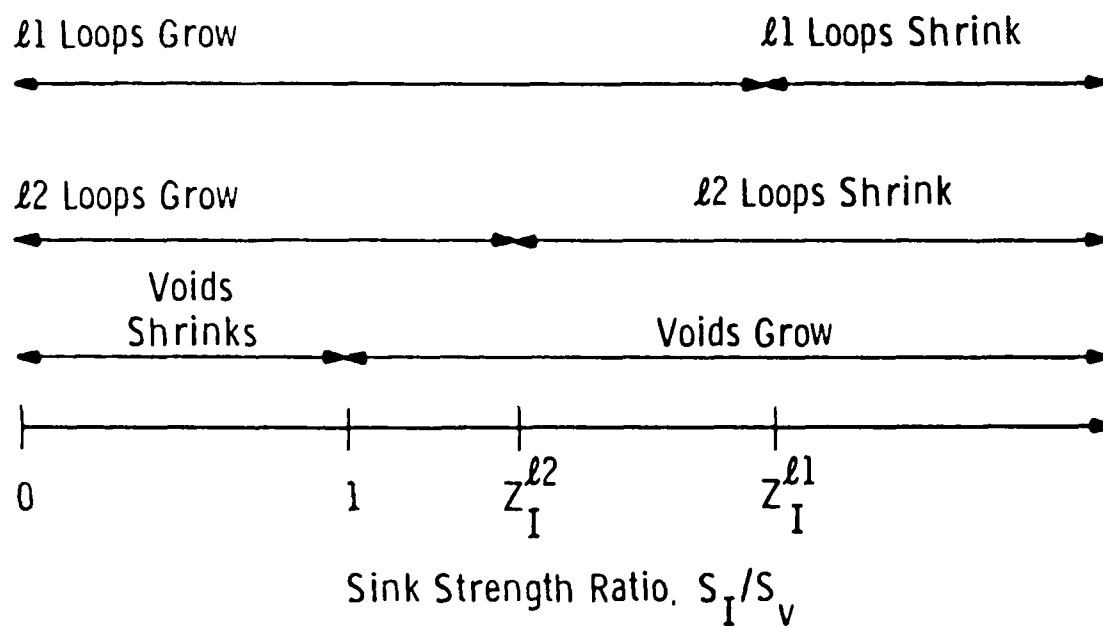
Fig. 3. Schematic of growth and shrinkage regimes for loops and voids as a function of sink strength ratio S_I/S_V

32
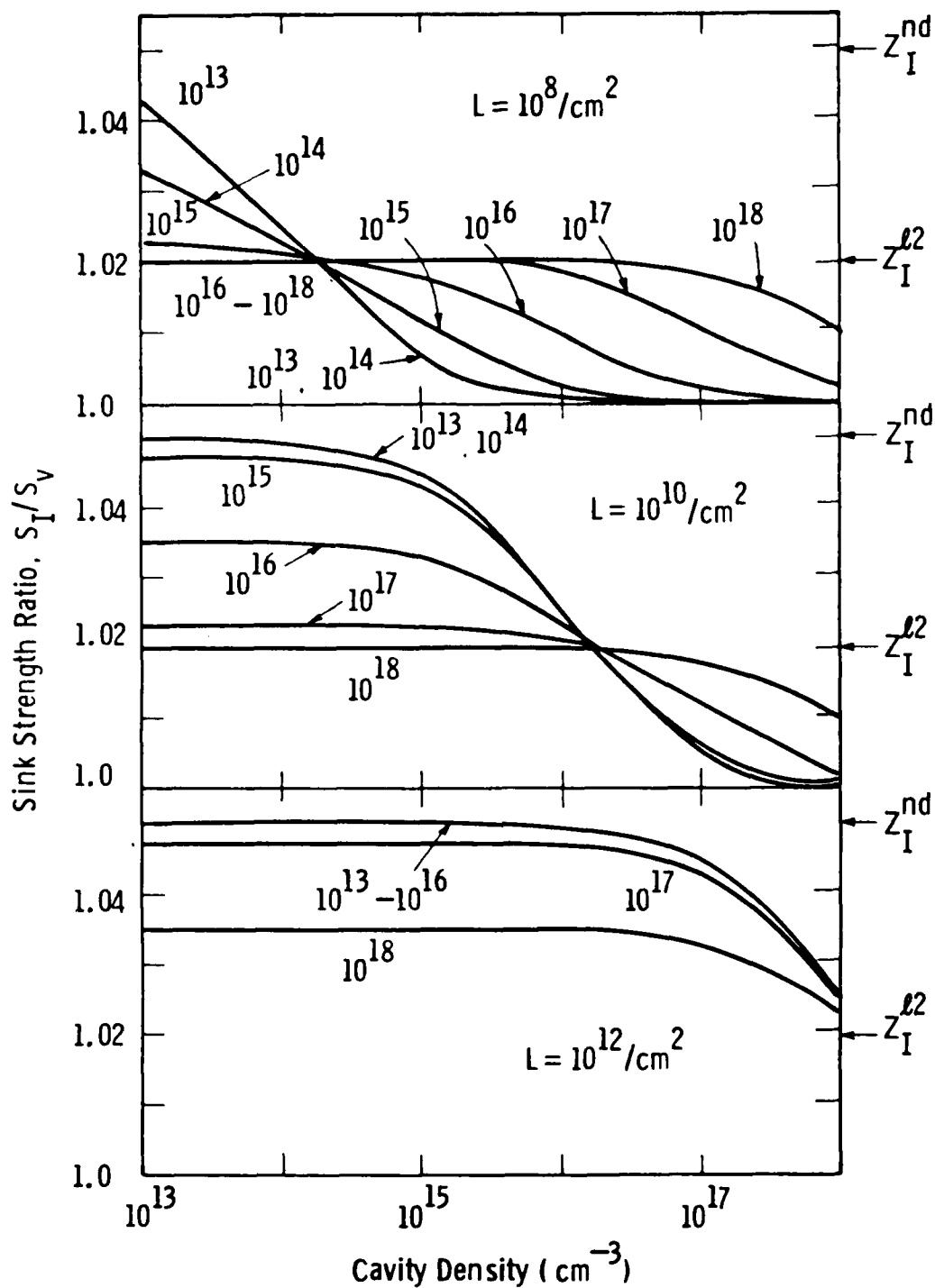
Fig. 4. Sink strength ratio S_I/S_V as a function of cavity density N_c for $Z_I^{\ell 2} = 1.02$, $Z_I^{\ell 1} = b_1 Z_I^{\ell 2}/b_2$, and $Z_I^{nd} = 1.05$. Panels are labeled by network density L, and individual curves by the value of $N_{\ell 2}$. $N_{\ell 1} = 10^{-5} N_{\ell 2}$.
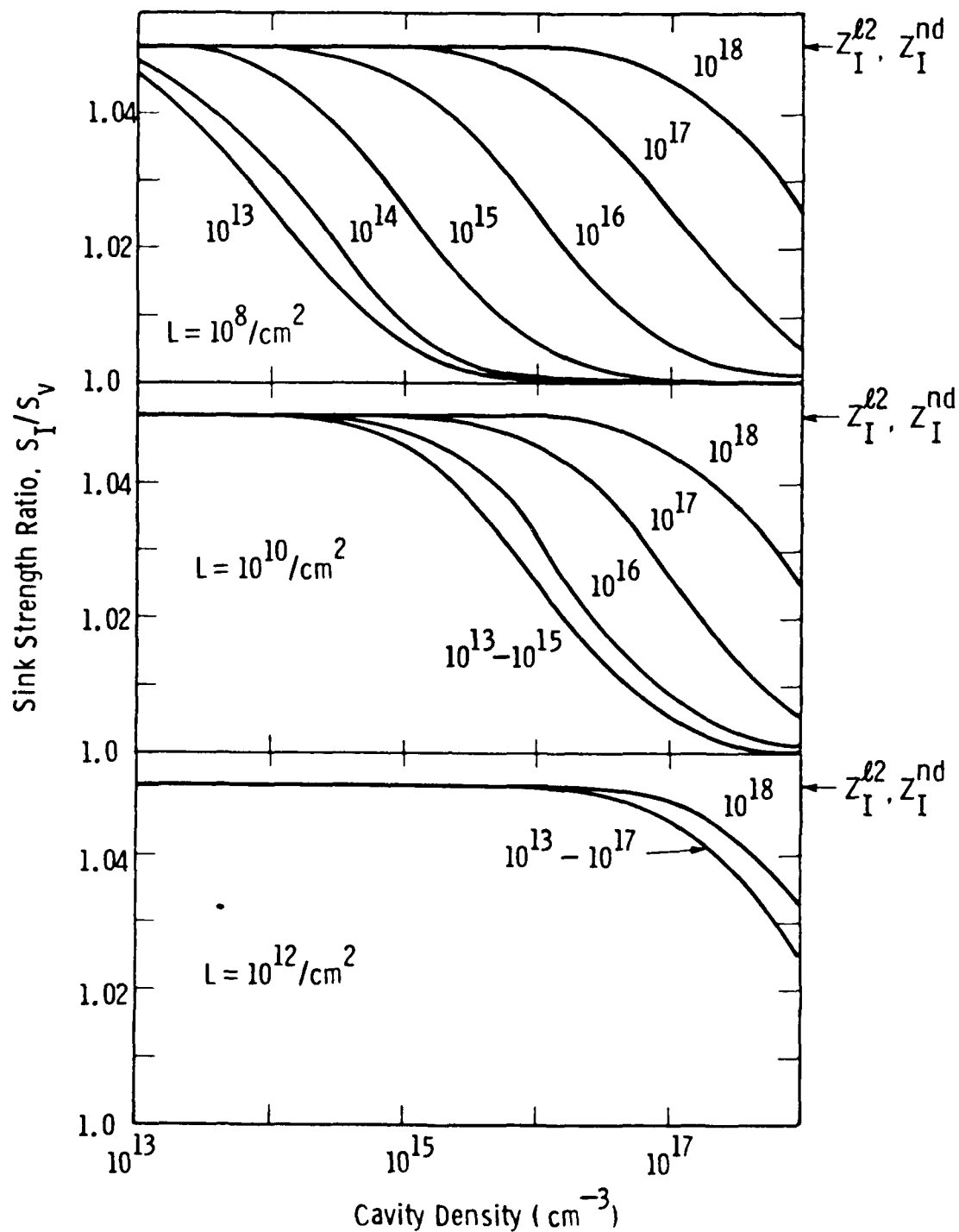
Fig. 5. Sink strength ratio S_I/S_V as a function of cavity density N_c for $Z_I^{\ell 2} = 1.05$, $Z_I^{\ell 1} = b_1 Z_I^{\ell 2}/b_2$, and $Z_I^{nd} - 1.05$. Panels are labeled by network density L, and individual curves by the value of $N_{\ell 2}$. $N_{\ell 1} = 10^{-5} N_{\ell 2}$.
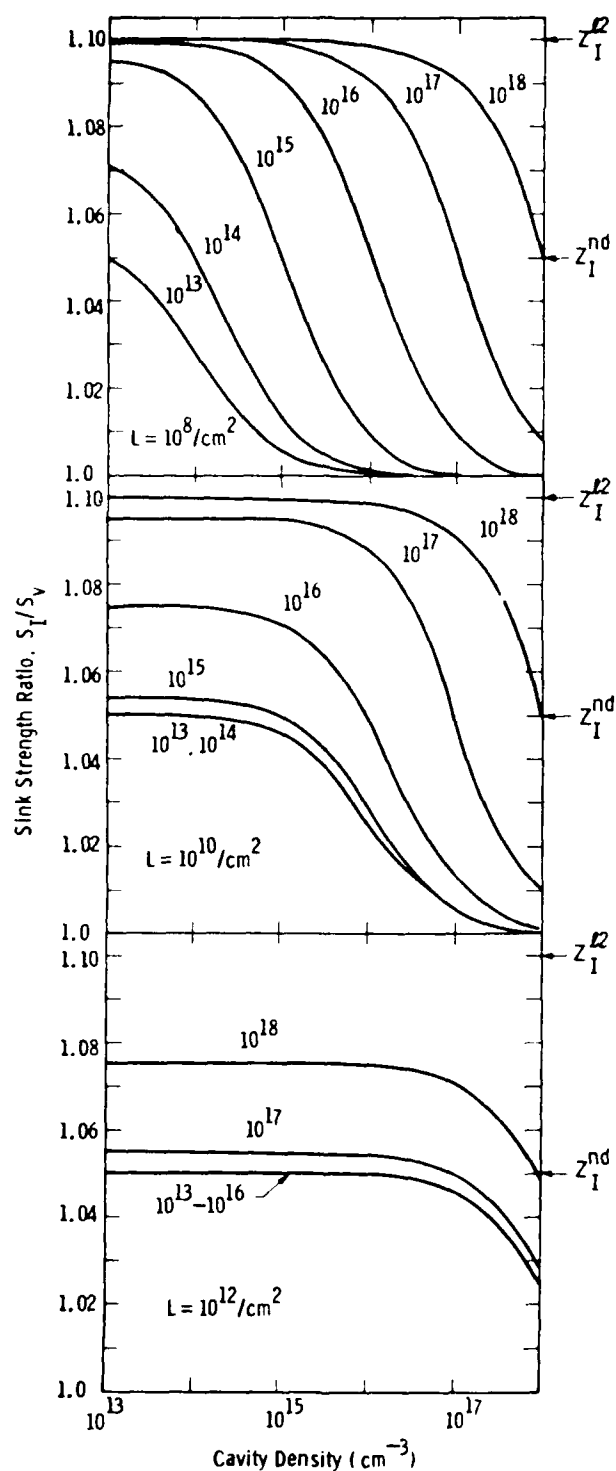
Fig. 6. Sink strength ratio S_I/S_V as a function of cavity density N_c for $Z_I^{\ell 2} = 1.10$, $Z_I^{\ell 1} = b_1 Z_I^{\ell 2}/b_2$, and $Z_I^{nd} = 1.05$. Panels are labeled by network density L, and individual curves by the value of $N_{\ell 2}$. $N_{\ell 1} = 10^{-5} N_{\ell 2}$.

35

network density is high and the <111> loop and cavity densities are relatively low. In the case where $Z_I^{\ell 2} > Z_I^{nd}$ (see Fig. 6), S_I/S_v approaches $Z_I^{\ell 2}$ when the network and cavity densities are low, and the <111> loop density is high.

The second point to be made regarding the results in Figs. 4 through 6 is that they establish the microstructural conditions under which <111> loops shrink, while <100> loops grow. As was stated previously, this requires that $Z_I^{\ell 2} < S_I/S_v < Z_I^{\ell 1}$ in the bias-driven growth regime. The condition is satisfied if $Z_I^{\ell 2} < Z_I^{nd}$ and if the network dislocation density dominates the sink strength ratio. Figure 4 shows that for a network density of $10^8/cm^2$, S_I/S_v is in the appropriate range if the cavity density is less than $\sim 10^{14}/cm^3$ and the <111> loop density is $\sim 10^{15}/cm^3$ or lower. When the network density is is $10^{10}/cm^2$, cavity densities of $\sim 10^{16}/cm^3$ or lower and <111> loop densities of $10^{17}/cm^3$ or lower will satisfy the requirement. Finally, if the network density is high, i.e. $10^{12}/cm^2$, $S_I/S_v > Z_I^{\ell 2}$ for all cavity and loop densities considered. This is consistent with experimental observations in FV 448[63,84], but requires a value for the bias factor $Z_I^{\ell 2}$ of <111> loops that is not in accord with current theoretical arguments.

In addition to Nichols' critique of theoretical calculations of bias factors, it should also be noted that these calculations treat a single sink that is isolated in a medium that possesses some averaged properties, which are assumed to account for the multiple-sink nature of the material. This approach may not give the appropriate bias factor for a sink whose absorption of defects is strongly influenced by the surrounding sink structure. In the calculations of void and cavity growth rates, therefore, values of $Z_I^{\ell 2}$ were not restricted to those greater than or equal to the network bias Z_I^{nd}.

6.7.2 Loop and Void Growth Rates

Growth rates for loops and voids were calculated as a function of temperature for network dislocation densities of 10^8 and $10^{11}/cm^2$ and bias factors $Z_I^{\ell 2}$ of 1.0, 1.02, 1.05, and 1.1. Values assumed for the microstructural parameters were $N_c = 10^{14}/cm^3$, $N_{\ell 1} = 10^{10}/cm^3$, $N_{\ell 2} = 10^{15}/cm^3$, $r_c = 10^{-7}$ cm, $r_{\ell 1} = 10^{-7}$ cm, and $r_{\ell 2} = 10^{-7}$ cm. $Z_I^{\ell 1}$ was equal to $b_1 Z_I^{\ell 2}/b_2$, the network bias factor

Z_I^{nd} equaled 1.05, and the displacement rate G was $10^{20}/cm^3$. The results are given in Figs. 7 through 9.

For the low network density, the growth rate of <100> loops increases monotonically with temperature as shown in Fig. 7, and, at a given temperature, increases slightly as $Z_I^{\ell 2}$ increases from 1.0 to 1.1.

When the network density is high, the growth rate increases with temperature from 625° to ~925°; at higher temperatures it maintains a constant value. The dependence of the growth rate on $Z_I^{\ell 2}$ is stronger, again increasing as $Z_I^{\ell 2}$ increases from 1.0 to 1.1.

As shown in Fig. 8, the temperature dependence of the <111> loop growth rate at low and high network dislocation densities is similar to that of the <100> loop growth rate. The magnitude and sign, however, depend on the choice of loop bias factor, as discussed in the previous section. When $L = 10^8/cm^2$ and $Z_I^{\ell 2} = 1.0$, the <111> loop shrinks at a rate of ~2 x 10^{-9} cm/s at 625°C and ~6 x 10^{-8} cm/s at 1425°C. For $Z_I^{\ell 2} = 1.02$, the shrinkage rate is an order of magnitude less at all temperatures. When $Z_I^{\ell 2} = 1.05$, <111> loops grow at rates which are comparable in magnitude to the shrinkage rates for $Z_I^{\ell 2} = 1.0$. An increase of the bias factor to 1.1 leads to roughly a factor of two increase in the growth rate over the $Z_I^{\ell 2} = 1.05$ values.

At the high network density, the growth rate is negative for $Z_I^{\ell 2} = 1.0$ and 1.02, with a decrease in magnitude for the latter values of less than a factor of two. The growth rate for $Z_I^{\ell 2} = 1.05$ is positive, but small -- three orders of magnitude lower than that for $Z_I^{\ell 2} = 1.1$.

The effects of network dislocation density and loop bias factors on the growth rate of voids are illustrated in Fig. 9. All of the curves are qualitatively

Fig. 7. Growth rate for <100> loops as a function of temperature. Solid
curves are for a network dislocation density L of 10^8/cm^2;
dashed curves are for L = 10^{11}/cm^2. Curves in each set are
for bias factors $Z_I^{\ell 2}$ = 1.0, 1.02, 1.05, and 1.1 in an ascending
sequence, with $Z_I^{\ell 1}$ = $b_1 Z_I^{\ell 2}/b_2$. Irradiation and microstructural
parameters are given in the text.

38

Fig. 8.   Growth rate for <111> loops as a function of temperature. Solid
curves are for a network dislocation density L of $10^8/cm^2$;
dashed curves are for $L = 10^{11}/cm^2$. Curves in each set are
for bias factors $Z_I^{\ell 2}$ values, with the sign indicating growth (+)
or shrinkage (-). Irradiation and microstructural parameters are
given in the text.
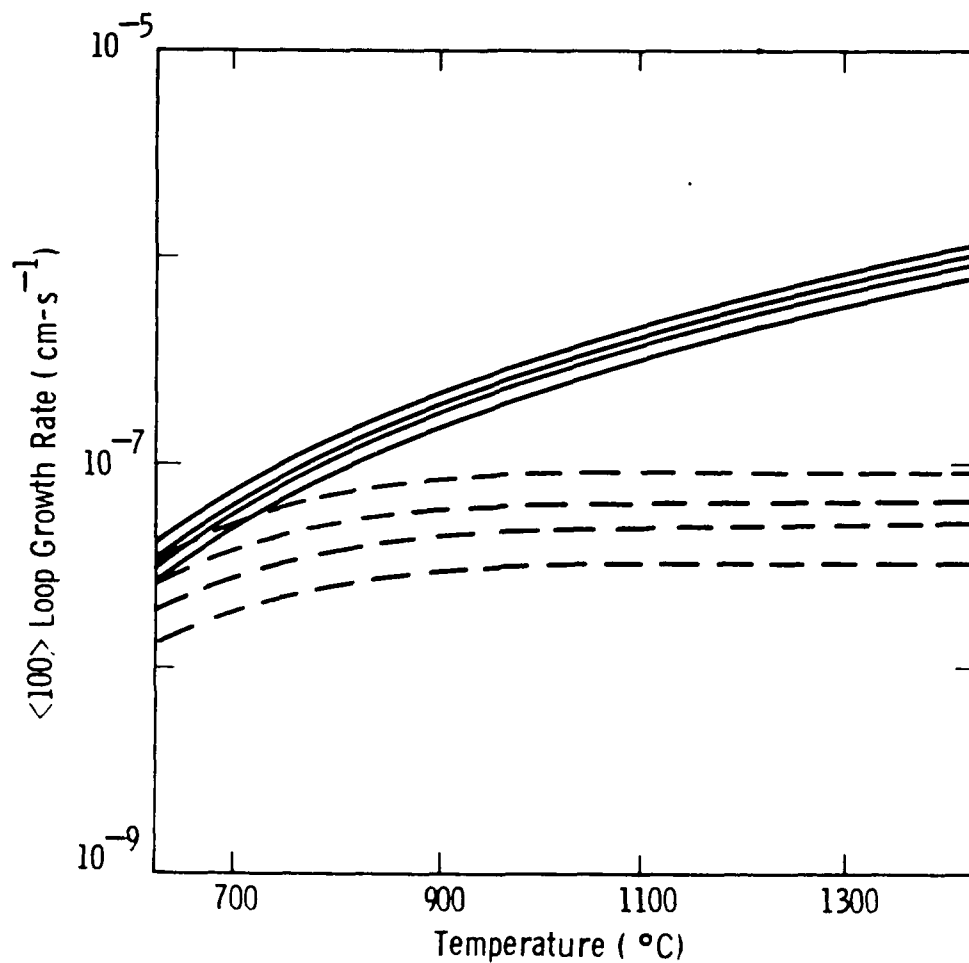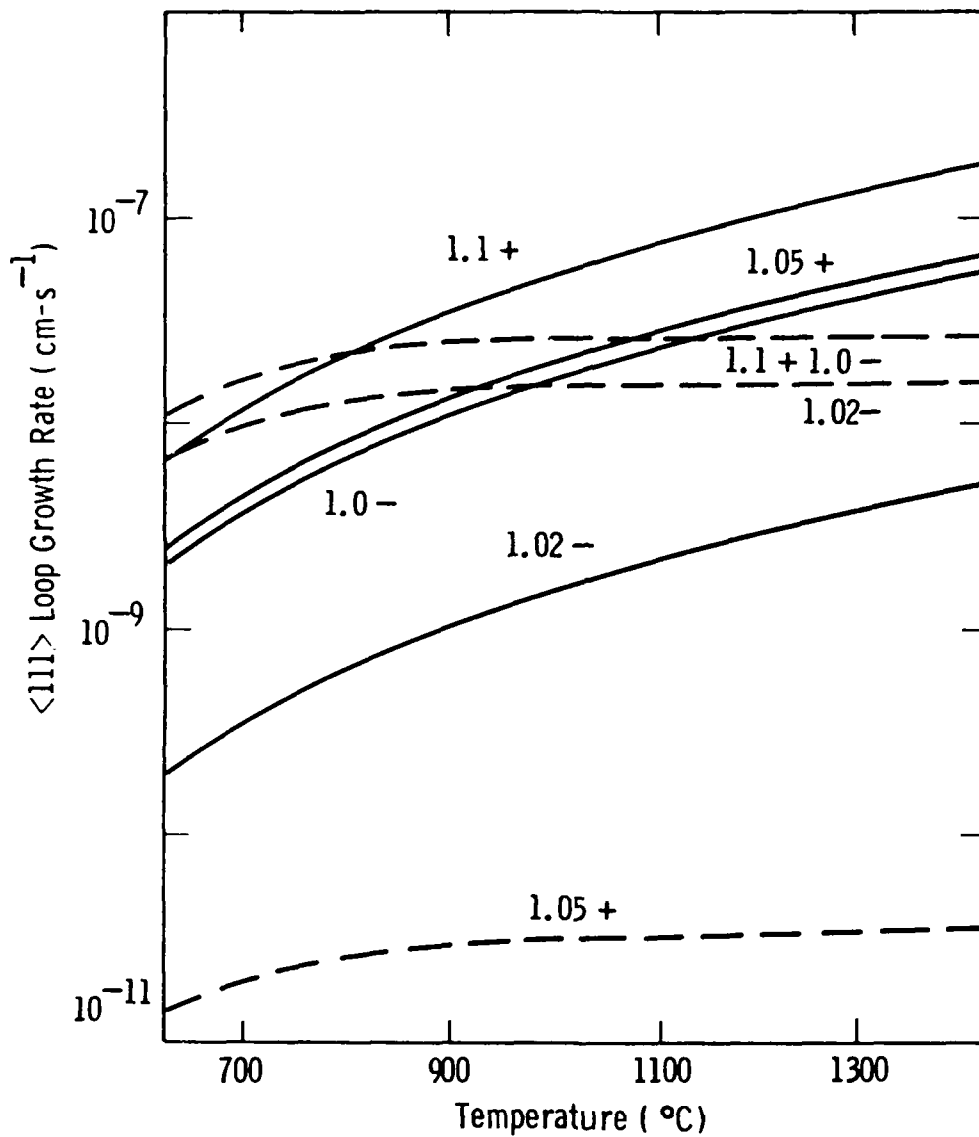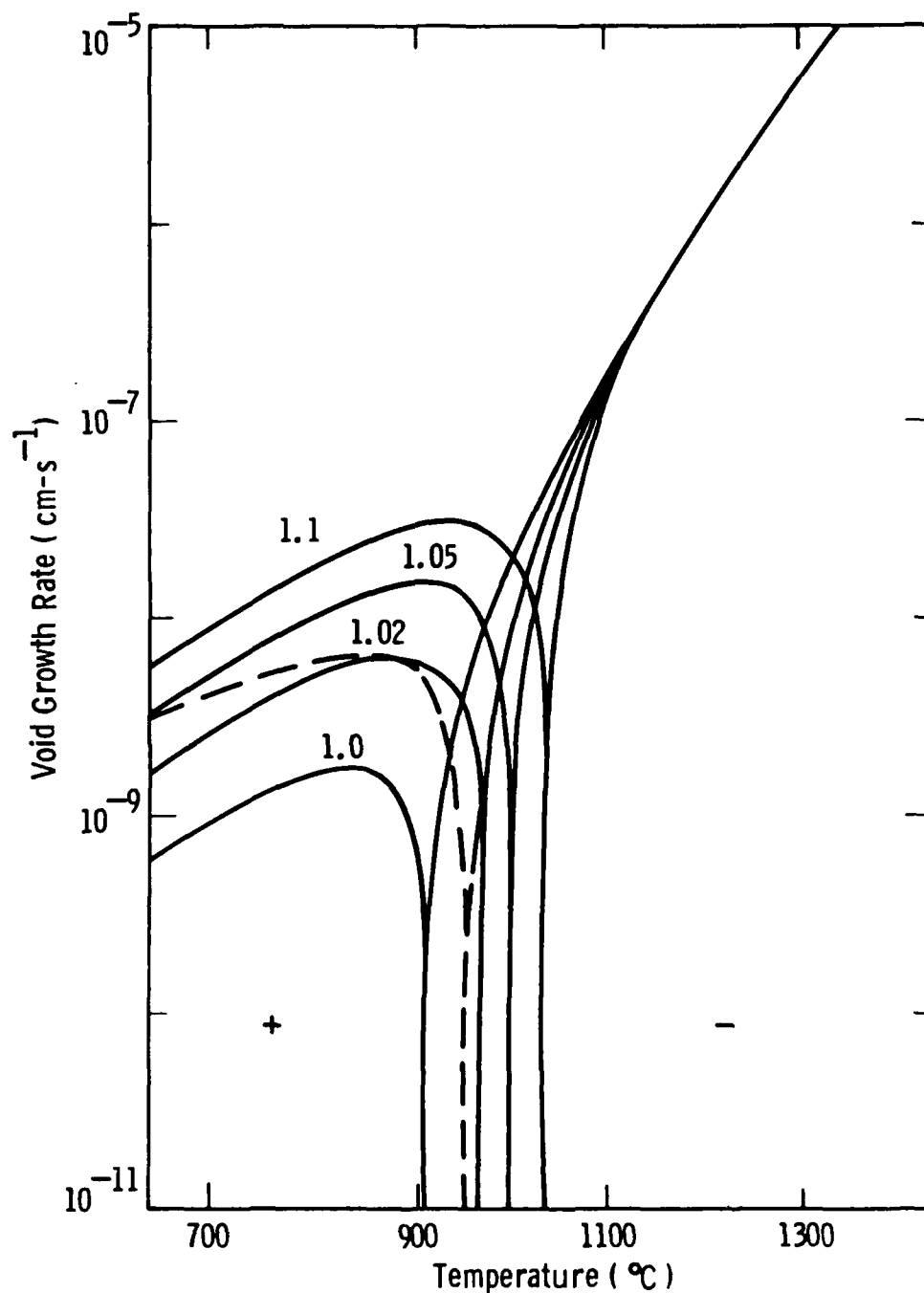
Fig. 9. Growth rate for voids as a function of temperature. Solid curves are for a network dislocation density L of 10^8/cm^2 and are labeled by assumed $Z_I^{\ell 2}$ values. Dashed curve is for a network density L = 10^{11}/cm^2, and for all values of $Z_I^{\ell 2}$ investigated. (+) sign indicates growth regime; (-) sign indicates shrinkage regime.

similar: at low temperatures the growth rate is positive, increases with increasing temperature, then peaks and decreases rapidly to zero, at a temperature which will be henceforth referred to as the critical temperature T_c. At temperature above T_c, the growth rate is negative and the void shrinks at an increasing rate. Above ~1100°C, the shrinkage rate is independent of both dislocation density and the values of $Z_I^{\ell 1}$ and $Z_I^{\ell 2}$ since in this regime, the thermal emission term in Eq. (34) is dominant. For a network density of $10^8/cm^2$, the void growth rate depends on the values of the loop bias factors, increasing by roughly an order of magnitude at low temperatures as $Z_I^{\ell 2}$ increases from 1.0 to 1.1. The peak temperature T_p increases as $Z_I^{\ell 2}$ increases, having values of 850°C, 875°C, 910°C and 935°C for $Z_I^{\ell 2}$ values of 1.0, 1.02, 1.05, and 1.1 respectively. T_c also increases with increasing bias factor, with values of 900°, 950°, 990°, and 1025°C. For the assumed microstructural conditions, the <111> loops are the dominant sink for interstitials and increasing bias on the loops means increasing absorption of interstitials. The vacancy supersaturation and void growth rate therefore increase.

For a network density of $10^{11}/cm^2$, the void growth rate is controlled by the absorption of interstitials at network dislocations and is independent of the loop bias factors. The peak temperature is ~860° and T_c is ~950°C.

6.7.3 Helium

The effect of helium on the cavity growth rate is illustrated in Fig. 10. The curves were obtained for an assumed bias factor $Z_I^{\ell 2}$ of 1.02, although the results are qualitatively similar for other values as well. The microstructural parameters and irradiation conditions used for the calculations were identical to those for Figs. 7 through 9, with network density $L = 10^8/cm^2$. Each of the curves in Fig. 10 is labeled by the ratio of the gas pressure P_g in the cavity to the equilibrium pressure given by $P_g^{eq} = 2\Upsilon/r_c$. The helium was treated as an ideal gas.

Three trends are immediately evident as the gas pressure in the cavity increases: the peak temperature T_p increases, the maximum growth rate
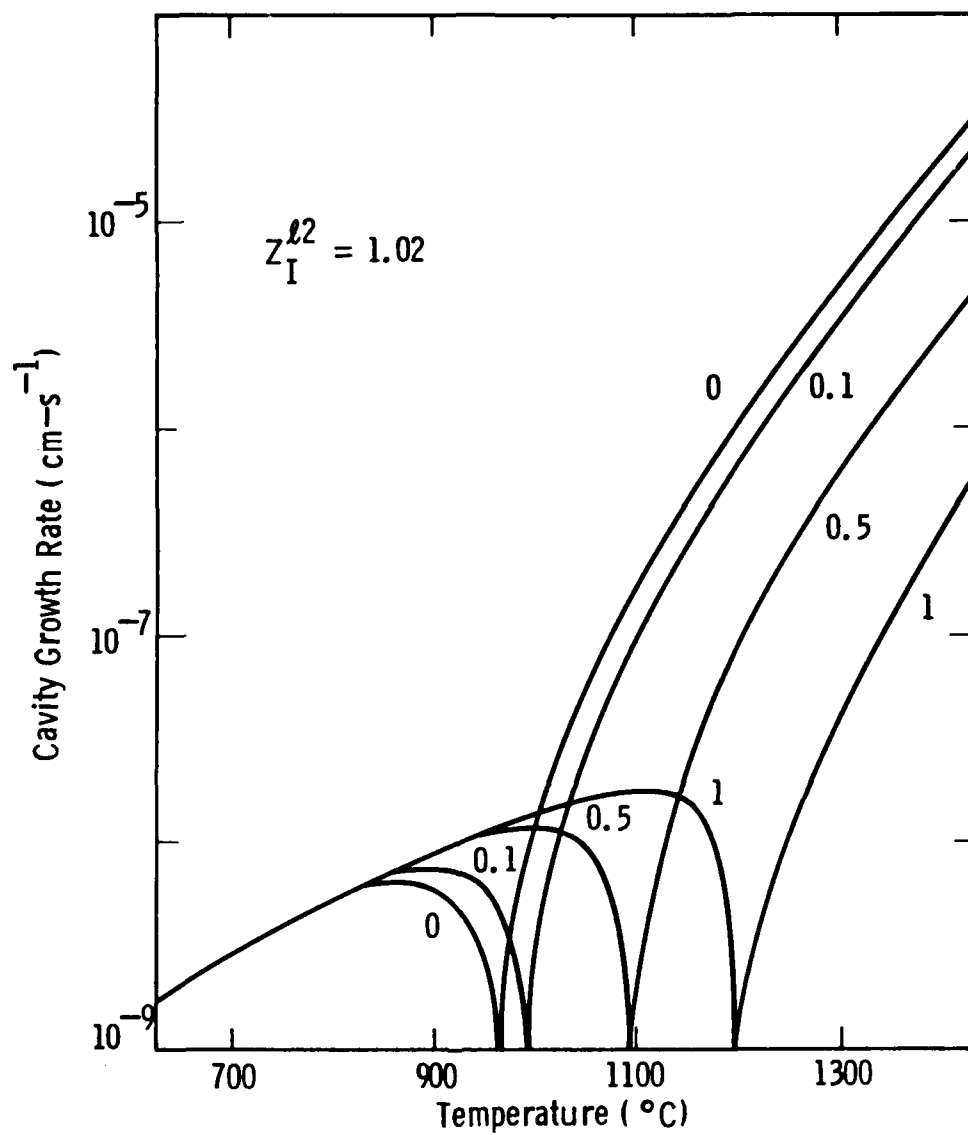
41

Fig. 10. Cavity growth rate as a function of temperature for $L = 10^8/cm^2$, $Z_I^{\ell 2} = 1.02$, and other parameters as given in text. Curves are labeled by ratio P_g/P_g^{eg}.

increases, and the critical temperature T_c increases. In Fig. 11, T_c and T_p are plotted as a function of the ratio P_g/P_g^{eq}. Both increase linearly, with T_c having a greater slope.

Swelling vs temperature or S(T) plots for various helium injection rates can only be obtained from a full model calculation, where the size distribution functions for cavities are calculated as a function of irradiation time at various temperatures. Figures 10 and 11, however, can be used to predict several qualitative features of these plots. First, for temperatures between 625°C and 825°C, Fig. 10 shows that the cavity growth rate does not depend on gas pressure, for the range of pressures considered. In this temperature regime, the rate of vacancy emission from cavities is small, cavity growth is determined by the bias, and S(T) plots will be insensitive to the helium injection rate.

Second, since the peak cavity growth rate increases in magnitude and occurs at higher temperatures as gas pressure increases, a temperature shift will be observed for the peak swelling temperature as helium injection rate increases. Third, since T_c increases more rapidly with gas pressure than T_p, the high temperature end of the S(T) plot will broaden as helium injection rate increases.

6.8 Summary of Results of Calculations

When microstructural evolution in body centered cubic metals is described using the formalism of the chemical-reaction-rate theory, the details of dislocation loop and void or cavity growth depend strongly on the interstitial preference or bias factors of the dislocations in the system. Whether loops of <100> type grow or shrink, the magnitude of loop and cavity growth rates, and the temperature dependence of the cavity growth rate are determined by the (relative) values assumed for these factors, when they are treated as size-independent model parameters. Over the range of microstructural and irradiation conditions investigated, however, shrinkage of cavities in the bias-driven regime (i.e. at low and moderate temperatures) was not observed. For this to occur with the model presented here, a low dislocation density, a high <111> loop density, and a bias factor for <111> loops less than 1 would be required.
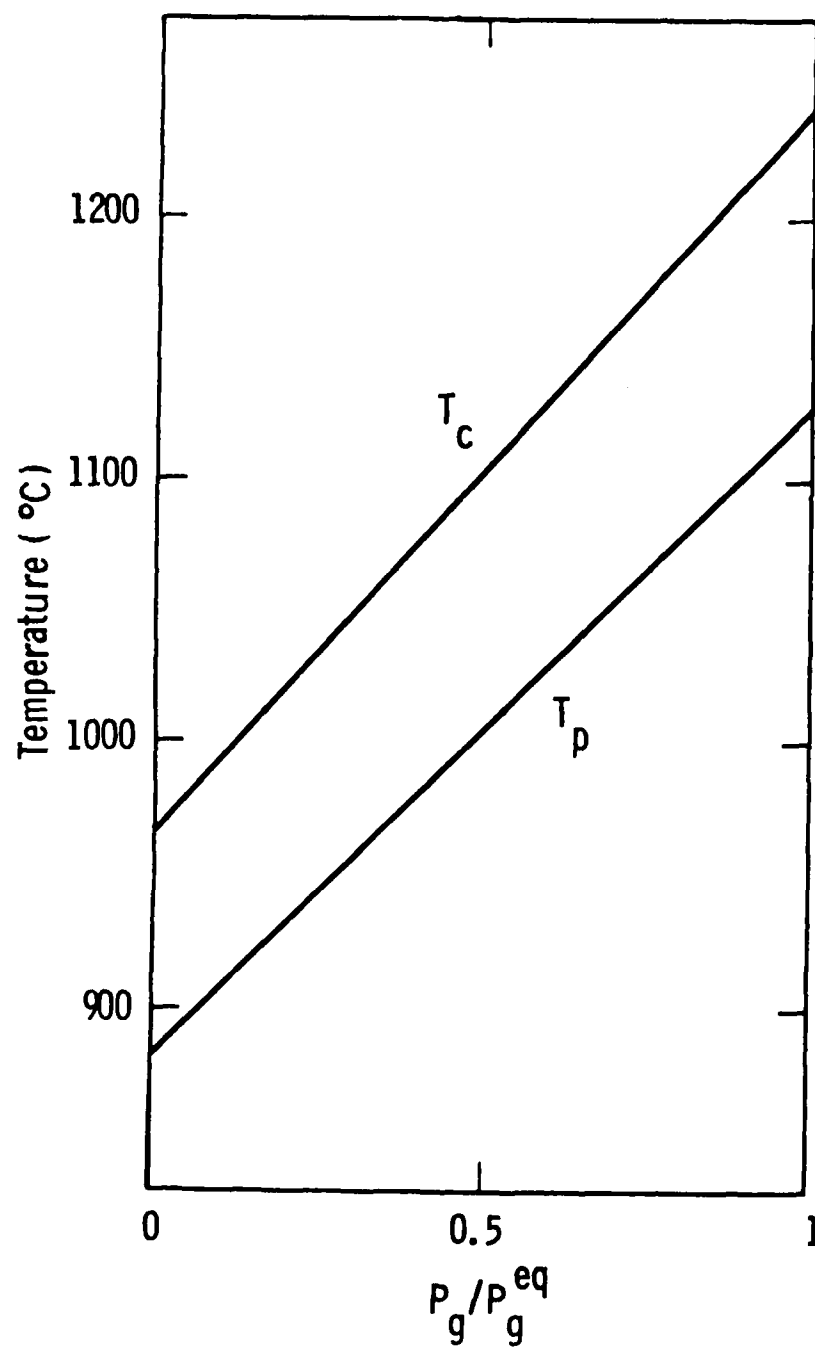
43

Fig. 11. Critical temperature T_c and peak growth temperature T_p as a function of ratio P_g/P_g^{eg}

The sensitivity of microstructural evolution to the dislocation bias factors in the body centered cubic metals over the midrange of temperatures suggests that this would be a fruitful regime for experimentation. In this regime, critical tests of theories on bias factors, which provide the fundamental basis for current models of cavity swelling, may be possible.

The model calculations presented here predict that, when helium is present, the temperature range for swelling is increased at the high temperature end and the peak temperature shifts to a higher temperature. These effects of helium in body centered cubic metals are qualitatively similar to those observed in face centered cubic metals.

7.0 EXPERIMENTAL

7.1 Irradiation Facility

The investigation of high temperature swelling in refractory metals requires a facility capable of providing high current beams of heavy ions and helium, which can simultaneously bombard a specimen heated to a high temperature ($0.6T_m$, approx. 1375°C for Nb). Experimental facilities capable of meeting these stringent requirements, together with high vacuum capability, high isotopic purity of incoming ions and diagnostics ability, are limited in number. A survey of existing accelerator facilities was therefore conducted to evaluate the best facility for this work. The evaluation also included turnaround times, schedular availability and unit costs. The following four facilities were considered as candidates

1. Dual-ion irradiation facility at the Oak Ridge National Laboratory
2. HVEM-Tandem Facility at the Argonne National Laboratory (ANL)
3. Irradiation Facility at the Pacific Northwest Laboratory
4. High Energy Ion Bombardment Studies (HEIBS) Facility at the University of Pittsburgh.

Of these four facilities only the HVEM-Tandem facility at ANL satisfied all of the program requirements and therefore was contracted to perform the irradiations. A brief description of the facility is provided below.

The HVEM Tandem facility consists of a Kratos 1.2 MV high voltage transmission electron microscope, a National Electrostatics 2-MV Tandem type universal ion accelerator, and a Texas Nuclear 300 KV ion accelerator. The two accelerators together provide ion beams of essentially all elements with energies from approx. 10 KeV to 8 MeV. The facility is located in the Materials Science and Technology Division at Argonne National Laboratory.

7.1.1 2-MV Tandem Accelerator

The National Electrostatics Type 2 UDHS 2.0-MV Tandem accelerator is equipped with one internal and two external negative ion sources for helium and metal ions, respectively. The specifications are given in Table VI.

Table VI. Specifications of Tandem Accelerator

Terminal Voltage	180-2000 kV
Charging System	1 pelletron chain
Energy Stability	$\pm$250 eV
Internal Ion Sources	Danfysik Models 910 & 911 Duoplasmatron

External Ion Sources
  He$^-$
  metal Ions
	
	NEC Alphatros
	Wisconsin SNICS Type

Ion Beams	All stable isotopes in the periodic table
UHV Beam Transport System	

Target Room Beam Lines
  West Lines
  East Lines
	
	45°(220)*, 30°(480), 8°(6560)
	10°(4200), 20°(1060), 30°(480), 45°(220)

* Numbers in parentheses indicate mass-energy products (amu•MeV).

The accelerator may be operated in conjunction with the HVEM or separately for ion implantation/bombardment and ion-beam-analysis studies. Independently

46

powered internal positive ion and external negative ion sources are provided
both to obtain all ion species in the periodic table and to minimize downtime
caused by ion source malfunction. Available positive ion sources are Danfysik
models 910 and 911, a duoplasmatron, a sputter source, and an rf source.
Negative ion sources presently available are an NEC Alphatros rf source for
He^- ions and a Wisconsin type SNICS source for producing negative ions of
selected metals. All ion sources are controlled by fiber-optic telemetry,
which also provides direct readout of source parameters at the control
console. Access to the internal source may be gained within one hour with use
of the high-throughput gas-recovery system which serves both the HVEM and the
accelerator. Typical ion-beam currents will range from ~10 µA for protons
to 0.1 µA for $^{204}Pb^{\pm}$. The mass-energy product of the East and West 30°
beam lines provides for singly charged ions with an atomic mass of 240 at an
energy of 2 MeV.

The 300-KV ion accelerator is a modified Texas Nuclear high-current unit that
has been equipped with sources for metal and gaseous positive ions. This
accelerator will be used to provide helium ion beam for the present program.

The NEC/University of Wisconsin SNICS (Source of Negative Ions through Cesium
Sputtering) and negative ion source, with ANL modifications to facilitate
target mounting and to provide target cooling, was used to perform the
experiments. The source yielded a ion current of ~40 nA with a metallic Nb
target. The flux of ions was too low to perform high fluence (~60 dpa)
irradiations in a reasonable amount of time. Therefore, a novel approach was
required to achieve a higher ion output. After a considerable effort, a
procedure analogous to the production of titanium ions was successful in
achieving high ion currents of niobium. This procedure requires a hydride
target material. A special hydriding method was developed at ANL to obtain
Nb-hydride. The process involves heating the Nb sample to high temperature
under vacuum, backfilling the vacuum chamber with high purity hydrogen at room
temperature to absorb the hydrogen and form a Nb-hydride compound. Use of
Nb-hydride target improved the output of the SNICS source from ~40 nA of Nb^-
with a metallic source to ~5-10µA of Nb ions (Nb^-, NbH^-, NbH_2^-, NbH_3^-,
etc.) with a hydrided target.

7.1.2 Material Procurement and Specimen Preparation

Niobium used in this investigation was Marz-grade foil (0.5 mm thick) obtained from the Materials Research Corporation. The material was received in an annealed condition, (1150°-1200°C for 0.5 h). The chemical composition of the material, as certified by the vendor is shown in Table VII. Overcheck analysis was conducted for the interstitial elements C, O and N, with results also shown in Table VII. A substantial disagreement is apparent between the vendors analysis and the overcheck analysis.

The preparation of the specimen surfaces to be used for ion irradiations is a delicate and painstaking operation consisting of a number of polishing steps and optical examinations. This process was made more difficult in the case of high purity niobium because of its low hardness, and therefore, susceptibility to surface smearing and cold work. The cold work of the surface was manifested by "mounds" on the specimens. These "mounds" were more numerous near the specimen edges than towards the center, and were always found whenever diamond abrasives were used. The polishing procedure had to be modified to avoid use of high hardness abrasives, and the material removal from the surface to be irradiated was minimized to 50 μm (0.002 in).

Disc specimens, 3 mm (0.12 in) in diameter, were punched from the foil, deburred and mounted with crystal bond wax and cold mount in a stainless steel holder with a 0.38 mm (0.015 in) recess and polished using a 600 grit paper to a thickness of 0.23 mm (0.009 in) with a final polish with 1 μm alumina. The specimens were then demounted and remounted with the flat 1 μm polished surface facing down, onto a stainless steel holder with 0.18 mm (0.007 in) recess. Two adhesives were then used to mount the specimens flat on the holder. First, specimens were placed on the holder in molten crystal bond wax. Each specimen was pressed to assure that the flat side was against the holder as the wax cooled. The wax from around the specimens was then removed and replaced with epoxy. This procedure assured a good and flat bonding of the specimens.

The specimens were then polished on 400 grit paper until they were flat and then gently polished with 6 μm and 1 μm alumina abrasive. During and after

TABLE VII   Chemical Analysis of Niobium Foil*

Element	Wt. ppm	
	Vendor Analysis**	Overcheck Analysis
H	<1	
C	25	33
N	<5	
O	15	120+
Na	0.07	
Mg	0.45	
Si	17.0	
P	<0.1	
Al	3.6	
S	1.4	
Cl	0.7	
K	0.2	
Ca	0.1	
Ti	<0.1	
Cr	1.8	
Fe	3.4	
Ni	1.0	
Cu	<0.1	
Zn	0.5	
Ga	<0.1	
Zr	<0.1	
Mo	<0.1	
Pd	<0.1	
Ag	5.9	
In	<0.1	
Sn	<0.1	
Sb	<0.1	
Ta	200	
W	<0.1	
Pt	<0.1	
Au	<0.1	
Pb	<0.1	

*   Marz Grade, Lot No. 41/2064, Foil 0.200 in thick x 1 in wide x 6 in long

** Analysis by mass spectrography, Leco method (gases and conductometric (carbon)

*** Analyzed by vacuum fusion analysis

\+   Average of two analyses.

each polishing step specimens were examined for flatness, scratches and cold work. The final polishing step consisted of 12-15 h polishing with 0.05 µm alumina in a vibratory polisher. No cold work was observed on any specimens following the above procedure. Following the polishing, the specimens were demounted and cleaned ultrasonically in multiple baths of acetone and methanol.

The cleaned specimens were lacquered on one side and then electropolished for 20 s in a solution containing 12% HF and 88% HNO_3 maintained at 0°-5°C. This step removed approx. 6 µm from the polished surface and produced a clean surface free of nearly all embedded abrasive. An additional 6-10 µm of material was removed from this surface by ion milling to assure scratch and deformation free surface.

Prior to irradiation each specimen was annealed at 1200°C for 0.5 h in the vacuum chamber of the accelerator. This further assured that the irradiated surface was in the fully annealed condition, devoid of any deformation due to specimen preparation. The temperature was monitored by an infra-red temperature monitor (IRCON 300 HCS). After cleaning the specimens, they were stored in 200 proof ethanol to avoid oxidation.

7.2 Irradiation Procedure

The specimens were loaded into a tantalum holder. The holder consists of a tantalum strip with 5 holes approx. 2.3 mm in diameter and with a 3 mm recess on one side. The specimens were secured by four tantalum tabs spot welded to the specimen holder. The tabs held the specimen by friction, therefore the specimen was free to move in all directions during annealing and irradiation. This avoided any deformation due to clamping. Four specimens were loaded at one time into the holder (the fifth hole was used to align the beams). The specimen holder had freedom in the x and y directions to enable accurate alignment with the beams. A photograph of the specimen holder and the electron gun heater is shown in Fig. 12.

The specimens were irradiated with 5.3 ± 0.1 MeV Nb^{++} ions at a nominal maximum displacement rate of approx. 6×10^{-3} dpa/s (displacements per atom per sec.). The target peak dose was approx. 60 dpa. The energy deposition
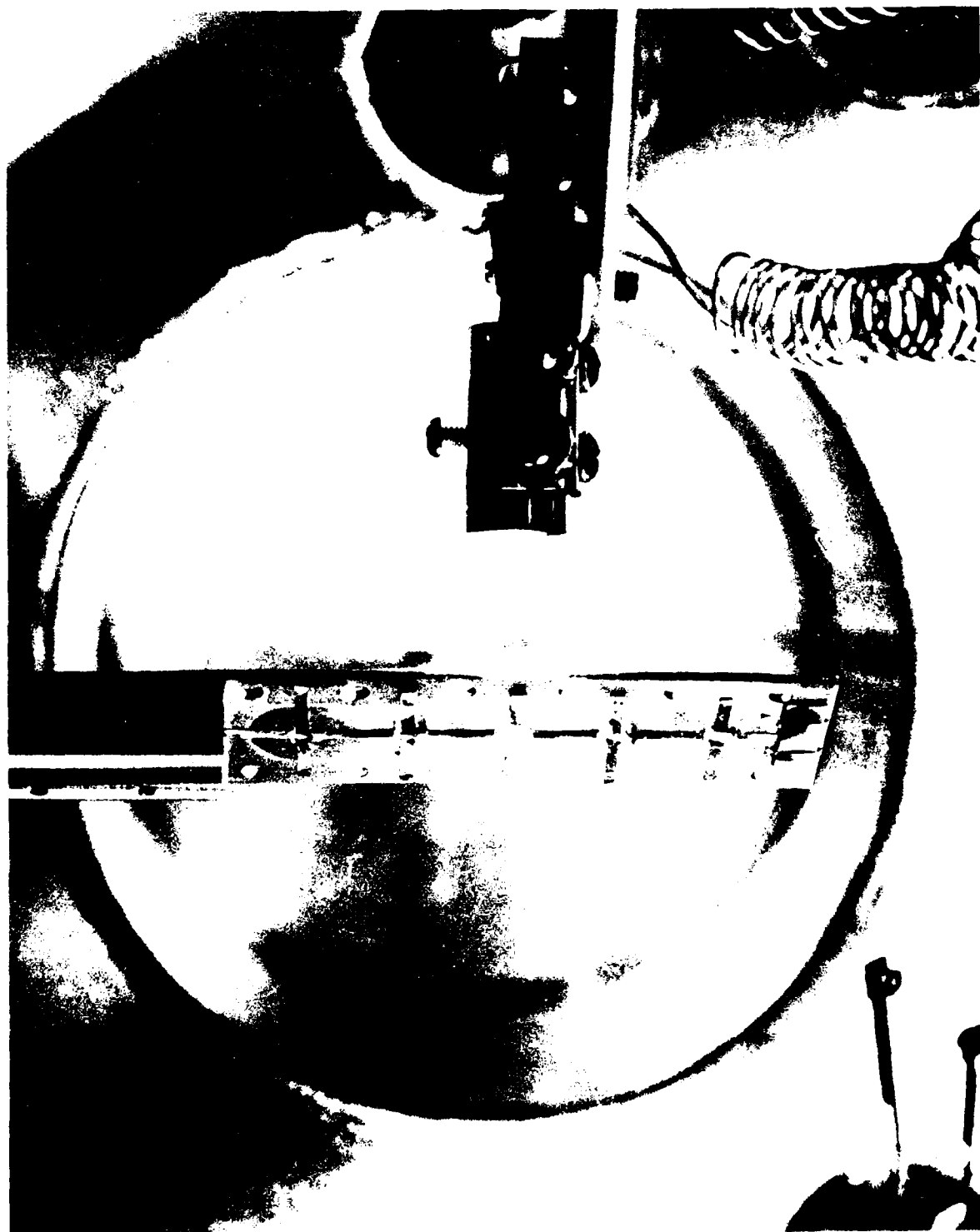
Fig. 12. A photographic view of the target holder and electron beam heating arrangement.

profile for Nb was calculated using Biersack's TRIM Monte Carlo program. Figure 13 shows the energy deposition and projected range probabilities for Nb in Nb at an incidence angle of 10°. The maximum energy deposition for 5.3 MeV Nb^{i++} bombardment was computed to occur at depth of ~900 nm. The calculated dpa values have an accuracy of $\pm$ 10%. In calculation of dpa, a displacement energy of 40 eV and an atomic density of 5.6×10^{22} atoms/cm^3 were assumed for Nb.

The implantations were performed at target temperatures ranging from 700° to 1300°C. The samples were individually heated to the desired temperatures using an electron beam heating system designed at ANL. The temperature was controlled using a feedback signal from an infrared pyrometer (IRCON 300 HCS) to the electron beam heater. The surface emissivity was assumed to be 0.19 independent of temperature and direction. The temperatures were controlled to within $\pm$ 5°C.

Prior to the irradiation and with the sample at room temperature, the all-metal vacuum sorption pumped system was evacuated to a base pressure of $\sim$2-5 $\times$ 10^{-9} torr. Typical vacuum levels achieved during annealing and irradiation are shown in Table VIII. Residual gas analysis of the chamber gases was performed during the annealing and irradiation stages using a Micromass QX200 quadrapole mass spectrometer. The major peaks during the irradiations were identified as being associated with nitrogen, water, and hydrogen.

Table VIII

Vacuum Conditions During Annealing and Irradiation

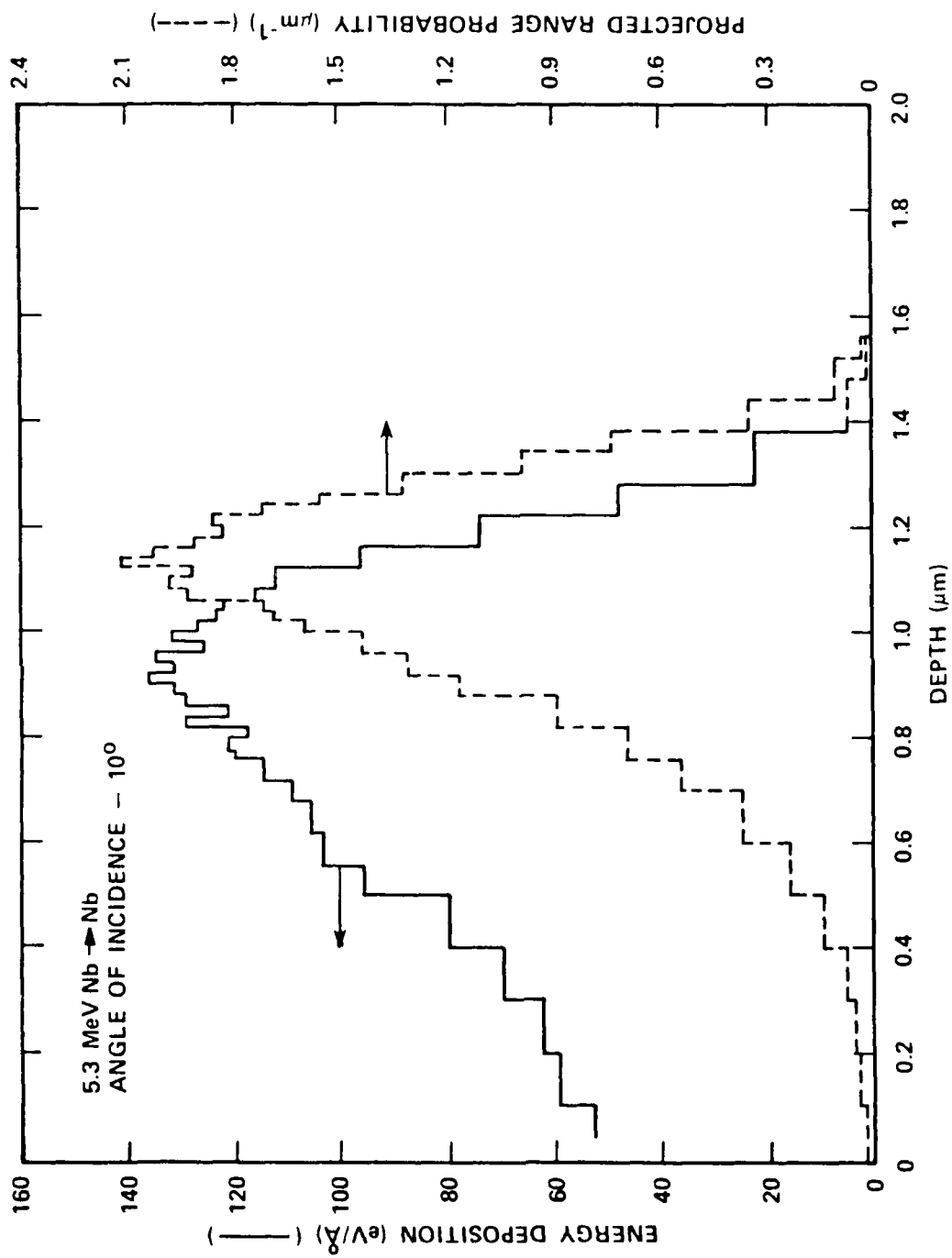| Irradiation Temperature (°C)	Vacuum During Annealing (torr)	Vacuum During Irradiation (torr)
700	5.0×10^{-8}	4.0×10^{8}
800	1.0×10^{-7}	4.0×10^{8}
900	2.0×10^{7}	2.0×10^{-8}
1000	4.0×10^{-8}	2.0×10^{8}
1100	6.0×10^{8}	6.0×10^{8}
1200	6.0×10^{8}	7.0×10^{8}
1300	4.5×10^{8}	5.0×10^{-8}
700 (10 dpa)	3.0×10^{8}	3.0×10^{8}

Fig. 13. Energy deposition and projected range probability for niobium irradiated with 5.3 MeV Nb^{++} at an incidence angle of $10°$.

The first 700°C specimen irradiation was performed at incidence angles of 10° and 45° to the specimen normal for equal times to spread the damage zone. However, it was realized that gradient effects may introduce microstructural changes which may be difficult to interpret; therefore, in subsequent experiments the irradiations were conducted at a single incidence angle of 10°.

7.3 Post-Irradiation Specimen Preparation and TEM Observations

Post irradiation specimen preparation involved removal of a controlled amount of material from the front surface (sectioning) so that the peak or near peak region of the damage could be examined in the transmission electron microscope (TEM). This method yielded data in the region of high damage away from the region most susceptible to surface effects. A Siemens Elmiskop 101 TEM operating at 100kV was used in this work.

The sectioning was accomplished using an ion milling technique. Ion milling involves removal of material by ion sputtering using inert gas ions, such as argon or krypton, accelerated to approx. 1 KeV. In our experiments ion milling was accomplished using argon gas accelerated to 800 eV. The specimens were rotated and tilted continuously during milling to achieve a uniform milling of surfaces. Prior to sectioning of irradiated specimens, the ion milling rate was calibrated using the same surface finish as the pre-irradiated specimens. Figure 14 shows a plot of ion milling depth as a function of milling time. This master plot was used to determine the time required for sectioning. All specimens except one were sectioned to remove 750 nm.

The irradiated surfaces of the ion milled specimens was protected by stop-off lacquer and the specimen was back-thinned using a modified Fischione Jet Polisher. One jet of the twin-jet polisher was removed to enable polishing from only the back side of the specimen. Considerable effort was expended in arriving at an appropriate thinning method for the specimens. A number of chemical solutions and conditions were investigated before a satisfactory polish was obtained. A solution of approximately 10% saturated NH_4F in 90% methanol at -30°C was found to produce a good polish in a reasonable time. A current of 12 mA at 100 V was required to polish a 1 mm diameter area in the
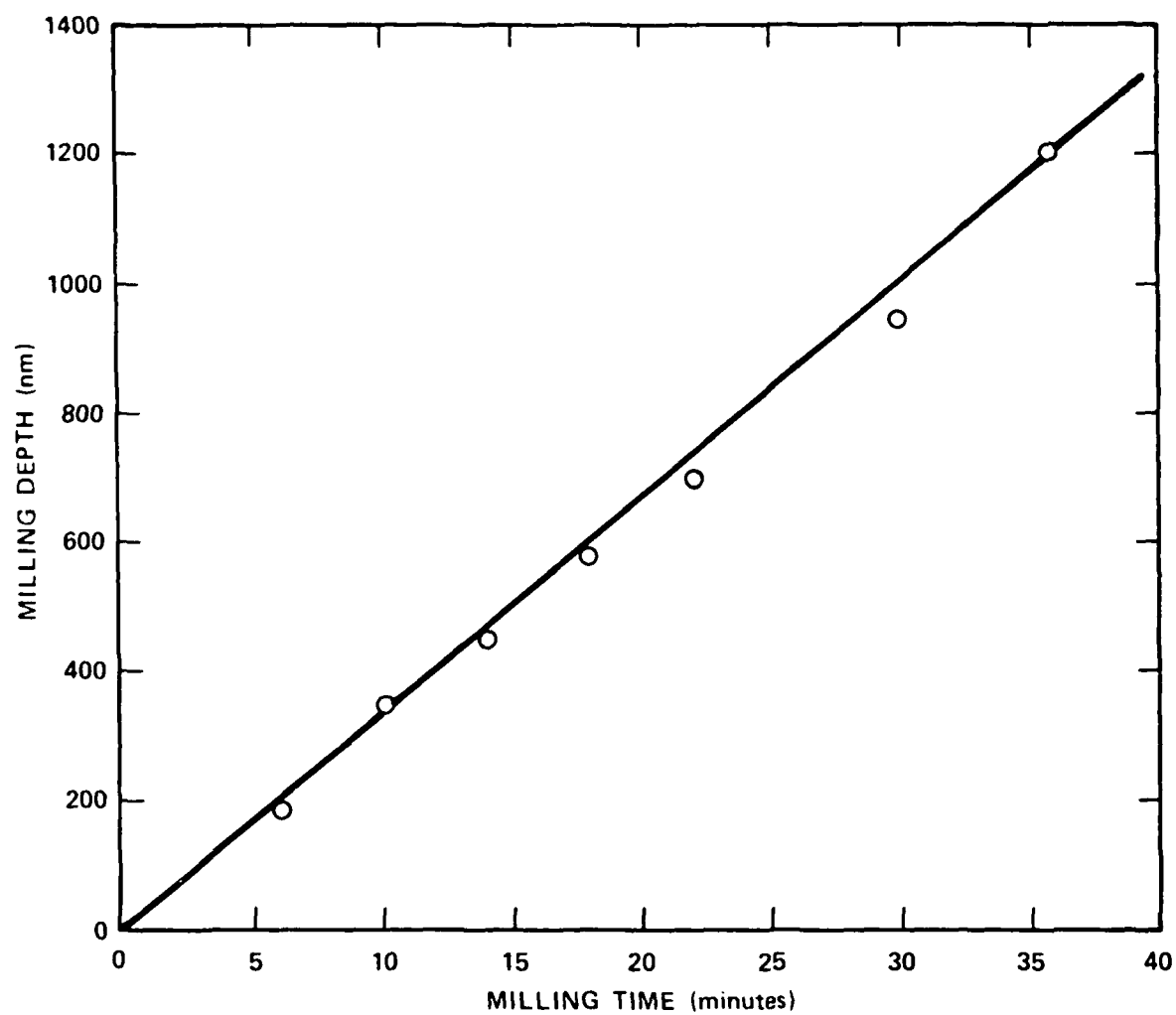
54

Fig. 14. Ion milling calibration curve for niobium

modified Fischione holder. The latter modification was deemed necessary to insure that the perforation and therefore the TEM observation was made in the area of the specimen where the ion beam was most uniform in intensity.

After removal of the specimen from the polishing holder, a gentle concave bowing of the top surface was observed. This may be indicative of some deformation of the specimen due to its softness. The bow was not considered to be a major problem.

TEM observation of an as-prepared specimen showed a thin oxide layer on the surface. This oxide layer was effectively removed by ion milling both surfaces for a duration of 5 minutes each at a low glancing angle of approx. 10° in a Gatan ion miller. It was estimated that this process removed ~10-20 nm from each surface.

7.4 Analysis of Data Obtained from TEM

TEM micrographs were taken at typical magnifications 40,000X and 75,000X. The voids were imaged in kinematic diffraction conditions in a slightly defocussed condition to obtain the true size of the voids. The dislocations and loops were imaged in two beam (dynamical diffraction) conditions. The voids were imaged in stereo-pairs to enable the determination of foil thickness. The dislocation and loops were imaged in the same areas as the voids to enable the determination of their densities.

The photographic plates were enlarged to a final magnification of 100,000X to 500,000X. Foil thickness was determined by using the following formula:

$$t = \frac{P}{2M \, \sin\theta/2},$$

where P is the parallax between surface features in a stereo-pair, M is the magnification, θ is the tilt angle, and t is the foil thickness.

The size and number of microstructural features were analyzed using a Zeiss particle size analyzer.

From the micrographs, the following parameters were evaluated.

(1) Diameter of the voids, d_i, in a size classification.

(2) Number of voids per cm^3, n_i, in a size classification.

(3) Void density $\rho_v = \Sigma F_{ti} \cdot n_i/\text{foil volume}$, where F_{ti} is
     the correction factor for surface intersection.

(4) Number of loops per cm^3.

(5) Average swelling defined by $\dfrac{\pi}{6} \sum_i F_{ti} n_i d_i^3$

(6) Weighted average diameter, d_v, of void, defined as

$$= \left(\frac{\sum_i F_{ti} n_i d_i^3}{\sum_i F_{ti} n_i} \right)^{\frac{1}{3}}$$

The void parameters were calculated from the void diameters measured on the
micrographs. Most of the foils were oriented with the normal in a <111>
direction. The diameter of the void was taken as the diameter of a circle
inscribed within the black fringe around the void. This void dimension gives
an upper bound estimate of swelling, especially at high temperatures
(> 1000°C) where voids showed less truncation of the cuboidal shape. Assuming
a perfect cube projected on a (111) plane the measured equivalent sphere
diameter is $a\sqrt{2}$ (where a is the cube edge). The corresponding swelling is
therefore over- estimated by 32%. In reality, however, not all voids showed
perfect cuboidal shapes and therefore the errors are estimated to be less than
30% in swelling and less than 10% in weighted average diameter. At low
temperatures, where voids were truncated in the <100> and <111> directions,
the errors are even less since they can be more closely approximated as
spheres.

57

For each specimen (except for those irradiated at 700°C) at least four micrographs were analyzed for void swelling to obtain a statistical estimate of the swelling parameters.

7.4.1 Correction Factor F_t for Surface Intersections

Voids exposed at the foil surface during electropolishing quickly erode to larger sizes and more irregular shapes, and may lose observable contrast. This occurrence was quite common in the niobium specimens examined, especially those with large voids. ASTM[85] has recommended corrections for obtaining bulk representative void densities from TEM micrographs. This correction involves exclusion of the voids whose centers lie within 0.5 d_i (d_i = void diameter) of each foil surface. This approach is not practical in many cases where a large number of measurements are required from many areas of foils at different magnification, and where a non-homogeneous distribution of cavities occurs or where thin areas of foils are examined. A correction factor suggested by Spitznagel et al.,[86] which avoids many of the problems, was therefore used here. The correction factor, F_t is defined such that

$$F_t = n_i = U_c \cdot A_A = \frac{2D_i}{2D_i + 3t} A_A$$

where n_i = number of cavities in size class i

U_c = Underwood correction factor to the specific projected area of the particle per unit test area, A_A

D_i = diameter of cavities in size class i

t = foil thickness

it can be shown[87] that

$$F_t = \frac{3t}{2D_i} \frac{2D_i}{2D_i + 3t}$$

58

If the number of cavities in each size class is multiplied by F_t, a volume fraction corrected for truncation of cavities, with centers either inside or outside of the foil volume imaged, is obtained. Every feature thought to be an image of a cavity, regardless of its proximity to the foil surface, can thus be counted and sized on the projected image. A numerical exclusion at void size of $D_i > t$ further ensures that an unrealistically large reduction in cavity volume fraction is not introduced. The factor F_t was included in all calculations of parameters defined in section 6.4 above.

8.0 RESULTS

The results from the transmission electron microscopy (TEM) of the Nb specimens irradiated from 700°C (0.35 T_m) to 1300°C (0.57 T_m) are presented in Table IX. This table lists the damage levels, swelling, void number density, void size and dislocation density for each of the specimen examined. Additionally, ranges in swelling, void number densities and void sizes are included. These ranges were obtained from the analysis of multiple areas of a specimen.

Figure 15 shows swelling as a function of irradiation temperature. Swelling was observed at temperatures from 700° to 1200°C. No voids were observed in the specimen irradiated at 1300°C. As seen in Fig. 15 the swelling increased from 700° to 900°C, reached a peak of 7% at 900°C and decreased slowly thereafter, with increasing temperature, to zero at 1300°C.

The void number density, expressed as voids per cm^3, is plotted as a function of irradiation temperature, in Fig. 16. The maximum void density was observed at the lowest irradiation temperature of 700°C, where the density was 1×10^{16} cm^{-3}. The void density decreased gradually, to 1×10^{15} cm^{-3}, over a temperature range 700°-900°C. From 900° to 1000°C the void density decreased rapidly to 5×10^{13} cm^{-3} and then decreased gradually from 1000° to 1200°C.

The decrease in void density was accompanied by an increase in the average void size as shown in Fig. 17. At 700°C, the average diameter of voids was 10 nm. The void diameter increased to ~ 45 nm at 900°C and then increased to 110 nm

Table IX. Summary of Swelling Data

Irradiation Temp., °C	Dose dpa	Swelling Range, %	Swelling Avg., %	Number Density Range, cm^{-3}	Number Density Avg., cm^{-3}	Diameter Range, nm	Diameter Avg., nm	Dislocation Density Avg., cm^{-2}
700	10 ± 2	-	0.5	-	4.8×10^{16}	-	6	-
700*	32 ± 4	0.6-0.8	0.7	$1-1.2 \times 10^{16}$	1.1×10^{16}	10.5-10.8	10.7	-
800	54 ± 9	2.3-2.9	2.6	$4.1-6.9 \times 10^{15}$	5.9×10^{15}	19.3-22.5	20.7	6×10^{10}
900	50 ± 9	5.8-7.9	7.0	$1-1.8 \times 10^{15}$	1.4×10^{15}	44.1-49.9	47.0	4×10^{10}
1000	57 ± 10	3.6-4.9	4.3	$4.1-6.3 \times 10^{13}$	5.52×10^{13}	107.5-118.3	115.9	3×10^{10}
1100	53 ± 9	2.4-3.2	2.7	$2-3.4 \times 10^{13}$	2.8×10^{13}	118.2-135.4	125.5	3×10^{10}
1200	52 ± 9	1.24-2.74	2.15	$1.9-3.1 \times 10^{13}$	2.75×10^{13}	92.7-140.8	116.5	2×10^{10}
1300	54 ± 9	-	-	-	-	-	-	-

*Specimen irradiated at incidence angles of 10° and 45° for equal times.
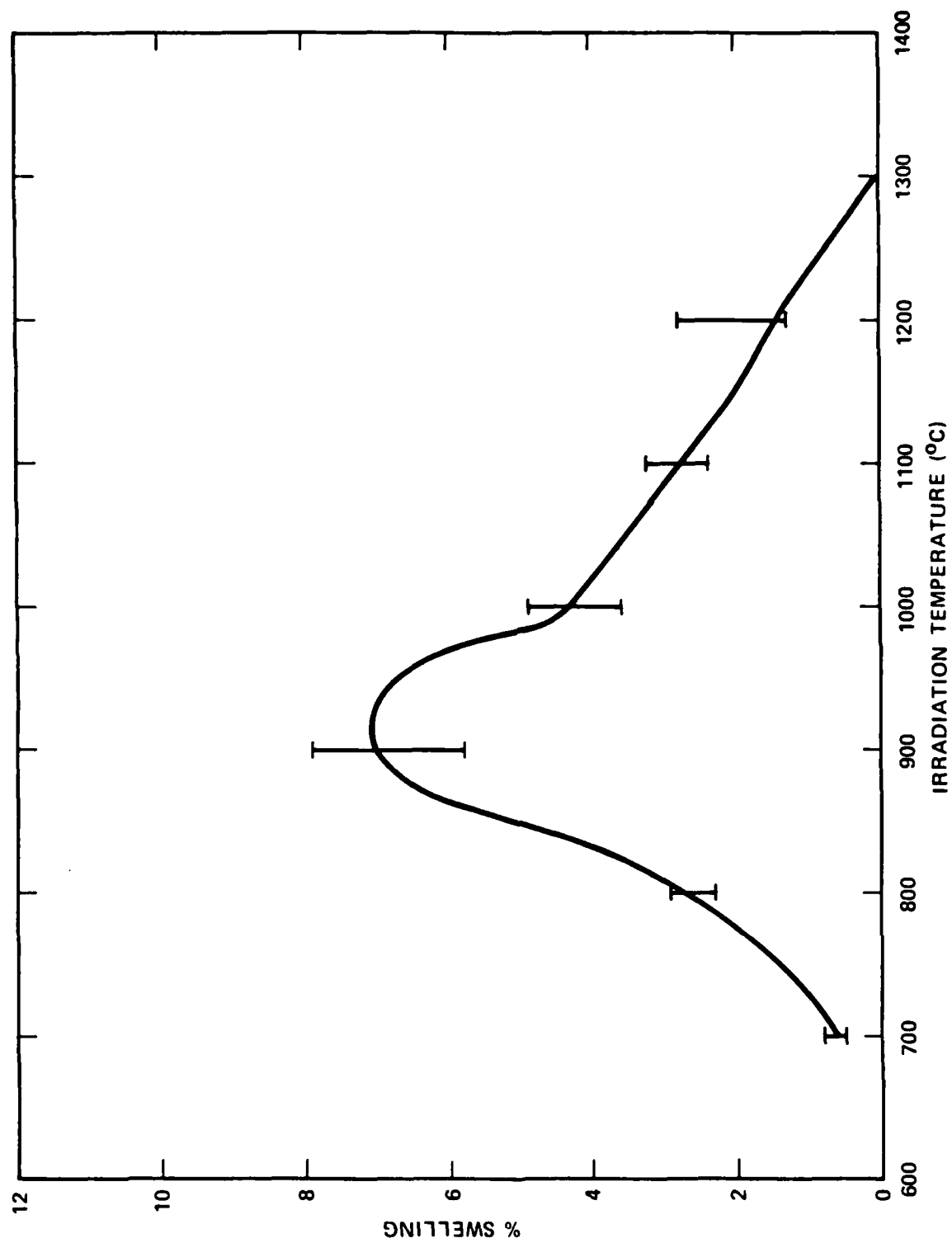
60

Fig. 15. Swelling as a function of irradiation temperature for self-ion irradiated niobium
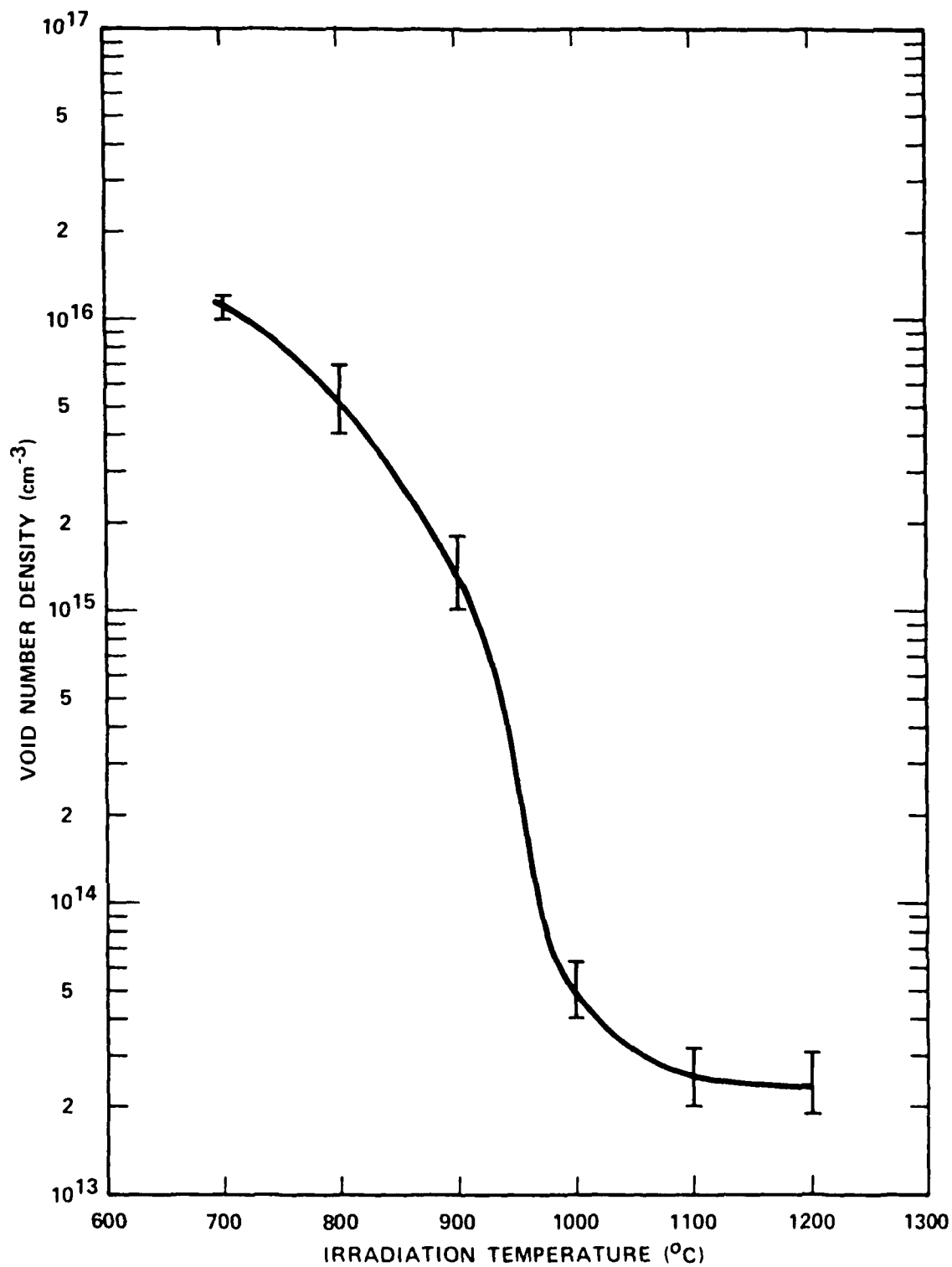
Fig. 16. Void number density as a function of irradiation temperature for self-ion irradiated niobium
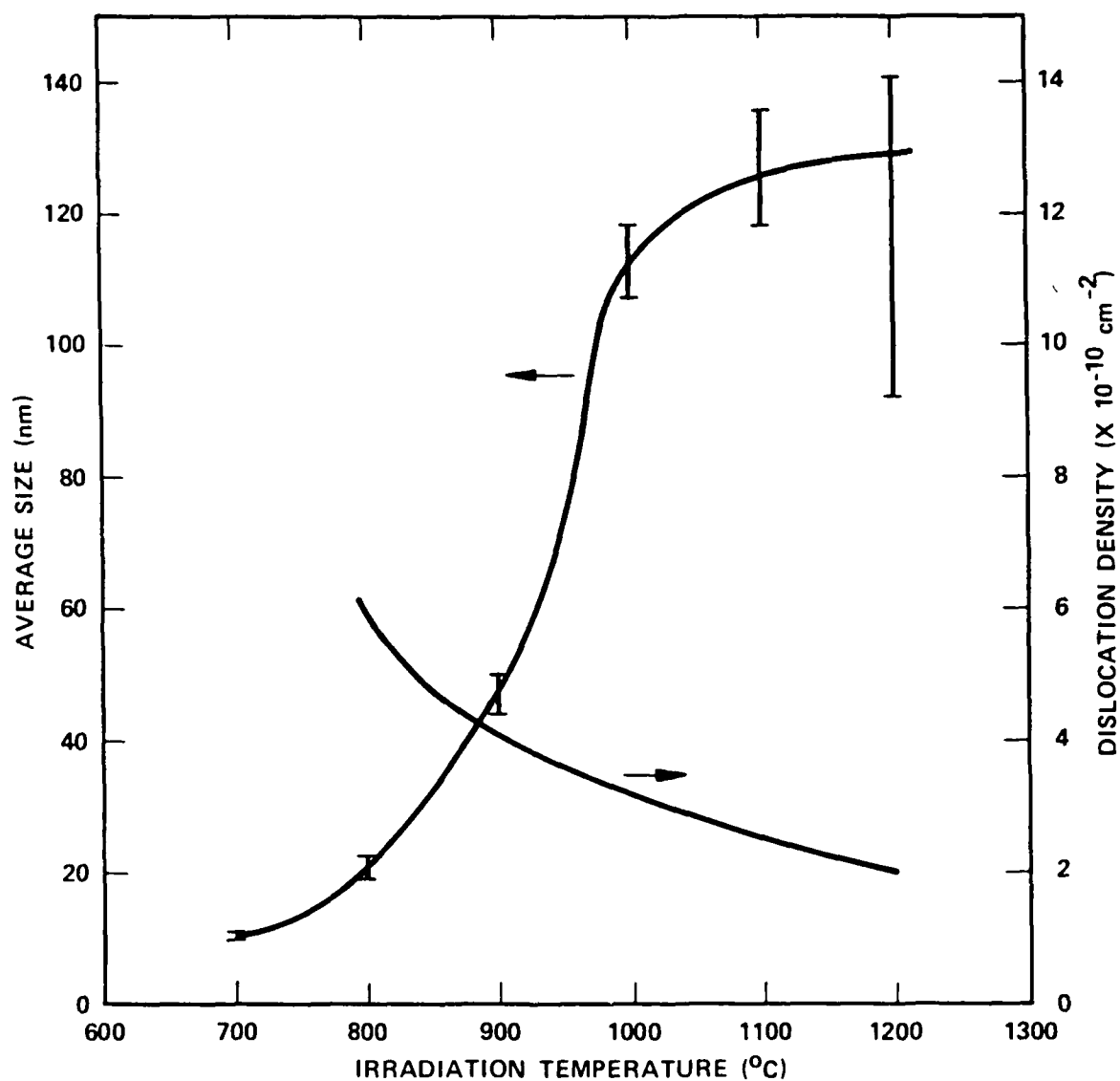
Fig. 17. Average void size and dislocation density as a function of
irradiation temperature for self-ion irradiated niobium

at 1000°C. Thereafter, the diameter increased slowly with increasing temperature. At 1200°C, a large scatter in void diameter was obtained from area to area in the specimen. A part of this scatter is attributed to enlargements of surface voids due to attack of the electropolishing agent on the large voids. The dislocation densities are also shown in Fig. 17. The dislocation densities varied from 6×10^{10} to $2 \times 10^{10} cm^{-2}$ for irradiation temperatures of 800° to 1200°C.

Figures 18-23 show typical photomicrographs of voids in Nb irradiated from 700 to 1200°C. Dislocations are also shown in the insets in these figures. The dislocations were imaged in a two beam condition, mostly with a diffraction vector $\vec{g}$ = <110>. Note the differences in magnifications of the micrographs.

The void size distributions are shown in Figs. 24-29. At low temperatures, the distributions showed single, relatively sharp peaks at 10 nm, 20 nm and 30 nm for 700°, 800° and 900°C. With increasing temperatures the void distribution shifted to larger sizes and broadened considerably. At the highest temperature (1200°C) the size distribution showed multiple small peaks which are again attributed to the attack on the voids by the electropolishing solution.

Micrographs from specimens irradiated at 700°, 800° and 900°C were carefully examined under a stereoscope for void ordering (void lattice formation) in all the three directions. No ordering was observed in any of the specimens. Void ordering was also absent in specimens irradiated at higher temperatures.

The loop size and density determinations were hampered by the presence of a high density ($>10^{16}$ cm^{-3}) of small (<10 nm) size loops produced by ion milling[88]. These loop sizes and densities were comparable to those expected at irradiation temperatures <800°C. At temperatures of 900°C the density of loops >30 nm in diameter was estimated to be 5×10^{14} cm^{-3}. At temperatures of 1000° - 1200°C they were 2-3 $\times 10^{14}$ cm^{-3}.

Table IX lists data for a specimen irradiated at 700°C to 10 dpa. The purpose of this experiment was to analyze the characteristics of dislocation

Fig. 18. Voids and dislocations (inset) in niobium irradiated to 32 ±4 dpa at 700°C. For voids $\vec{Z} \sim$ [113], for dislocations $\vec{g}$ = [110], $\vec{Z} \sim$ [113].
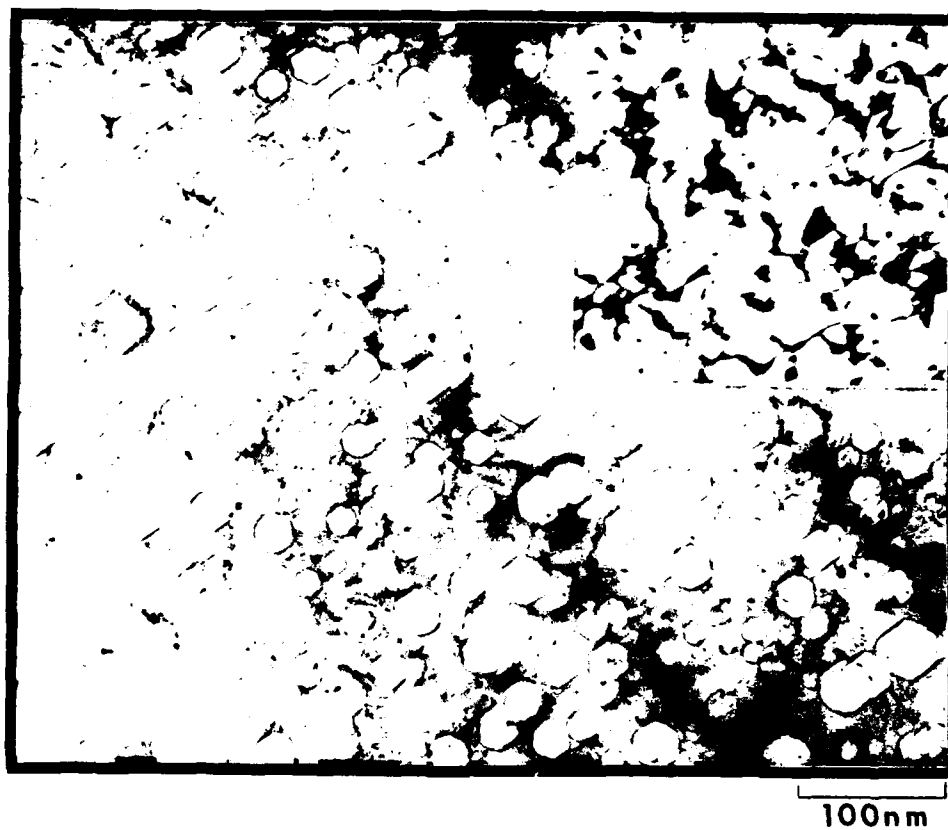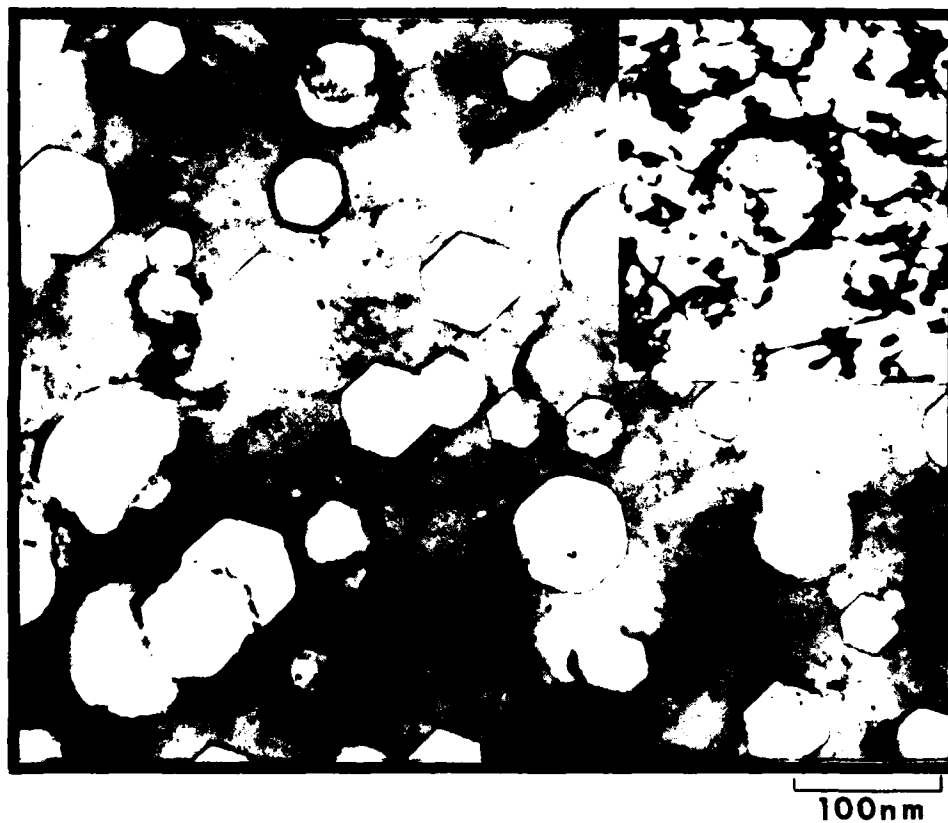
100nm

Fig. 19. Voids and dislocations (inset) in niobium irradiated to 54 ±9 dpa
         at 800°C. For voids $\vec{z}$ ~ [111], for dislocations $\vec{g}$ = [110],
         $\vec{z}$ ~ [111].

66

Fig. 20. Voids and dislocations (inset) in niobium irradiated to 50 ±9 dpa at 900°C. For voids $\vec{Z} \sim [111]$, for dislocations $\vec{g} = [110]$, $\vec{Z} \sim [111]$.
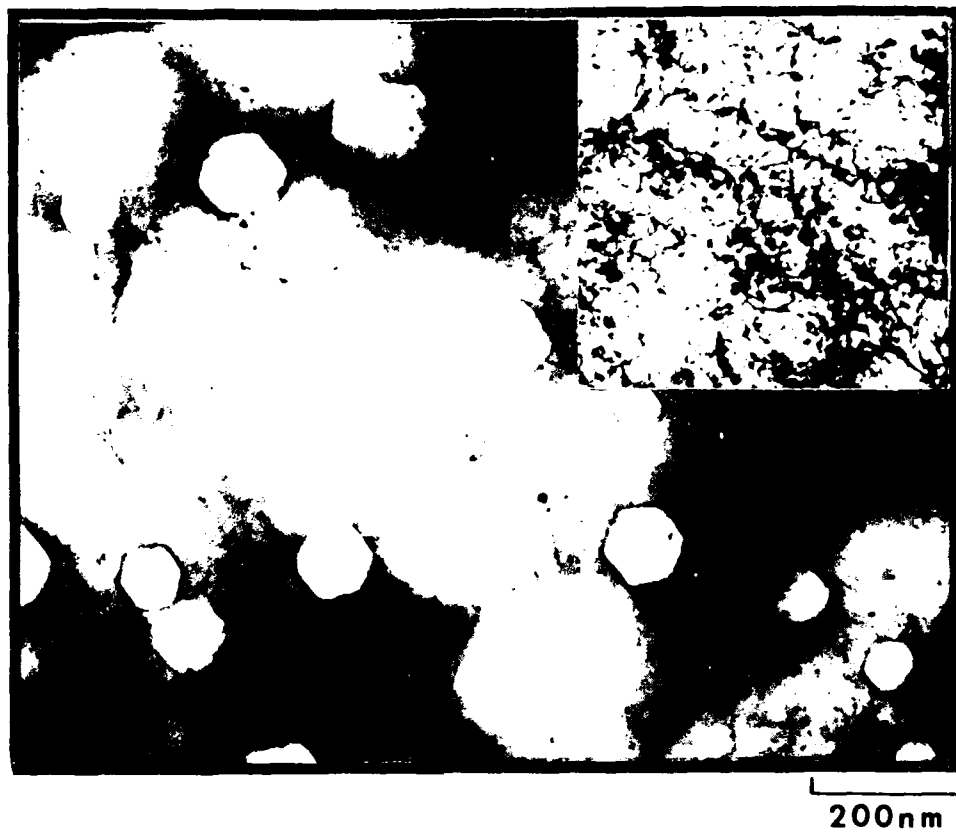
Fig. 21. Voids and dislocations (inset) in niobium irradiated to 57 ±10 dpa
dpa at 1000°C. For voids $\vec{z} \sim [111]$, for dislocations $\vec{g} = [110]$,
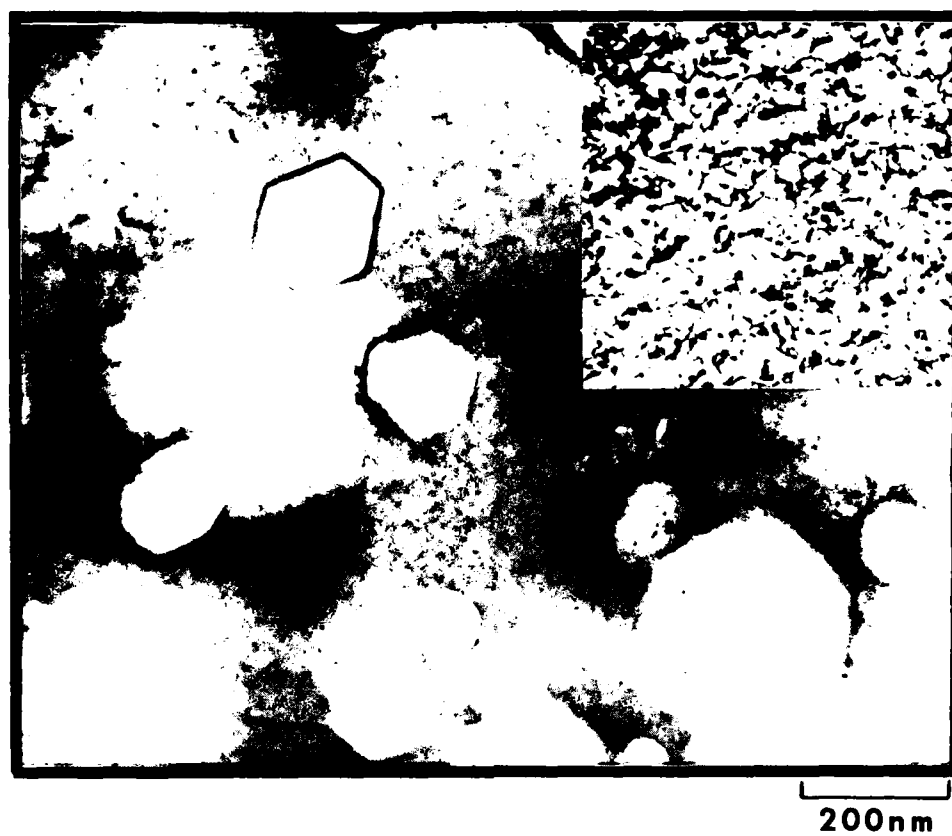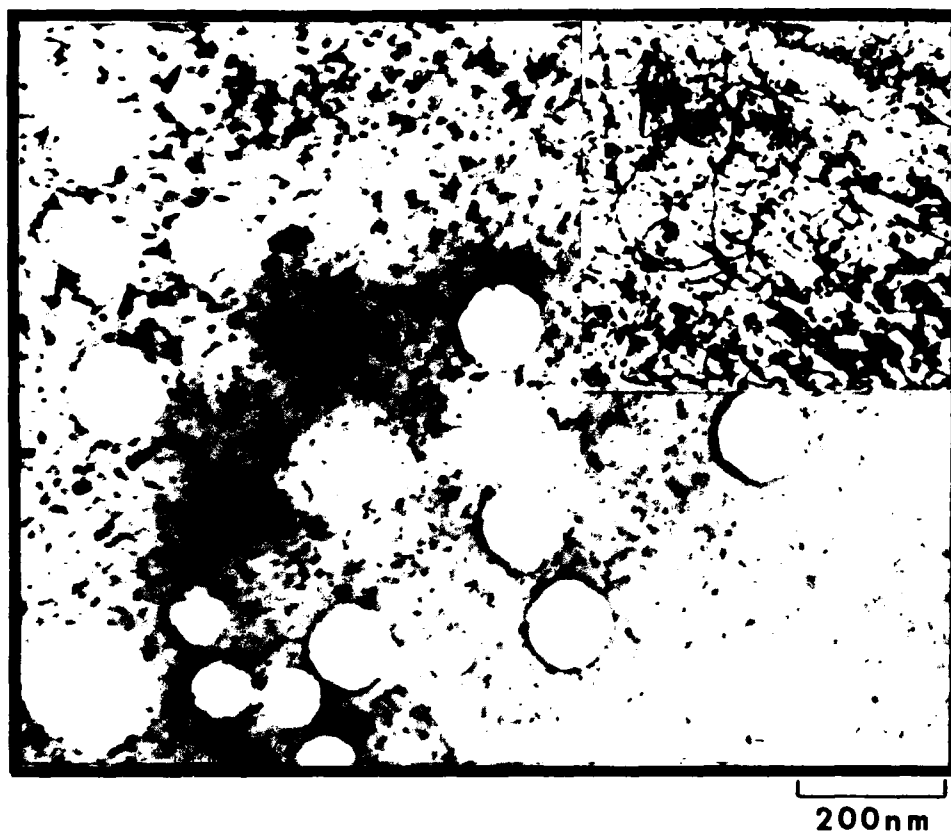$\vec{z} \sim [111]$.

Fig. 22.   Voids and dislocations (inset) in niobium irradiated to 53 $\pm$9 dpa
at 1100°C.   For voids $\vec{Z} \sim$ [111], for dislocations $\vec{g}$ = [110],
$\vec{Z} \sim$ [111].

Fig. 23. Voids and dislocations (inset) in niobium irradiated to 52 ±9 dpa at 1200°C. For voids $\vec{Z} \sim [111]$, for dislocations $\vec{g} = [110]$, $\vec{Z} \sim [111]$.
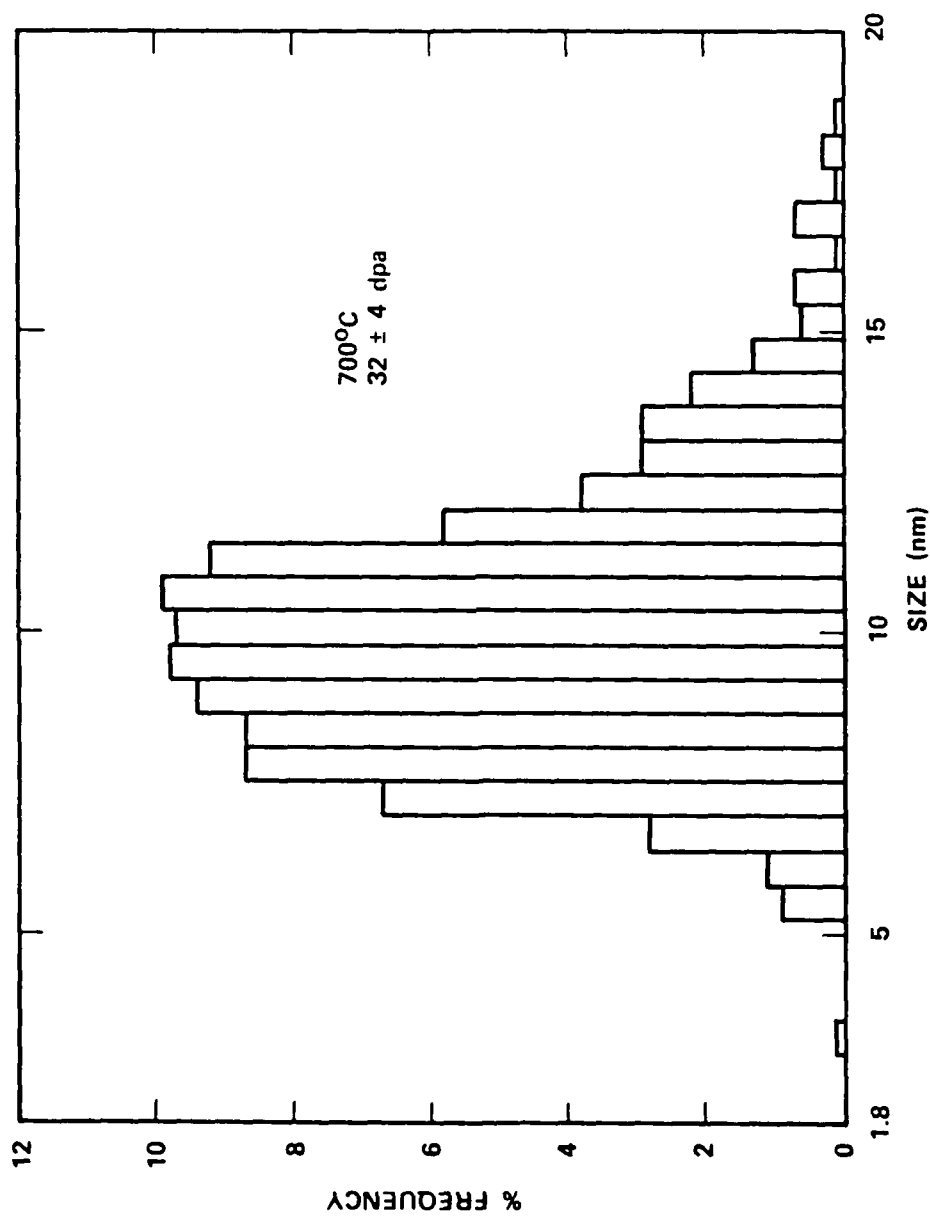
Fig. 24. Void size distribution in niobium irradiated at 700°C to 32 ±4 dpa. NOTE: Incidence angles were 10° and 45° for equal times.
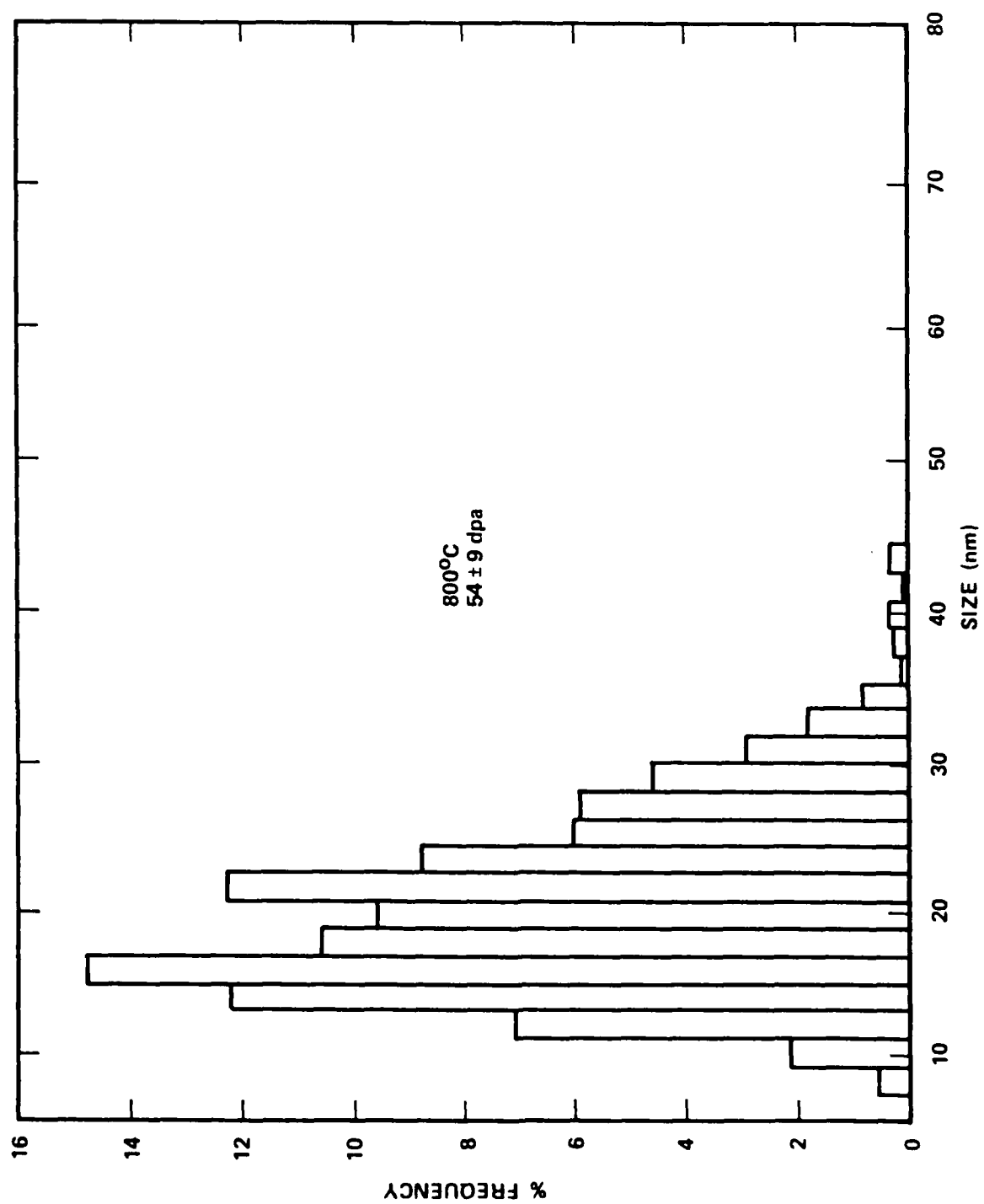
Fig. 25. Void size distribution in niobium irradiated at 800°C
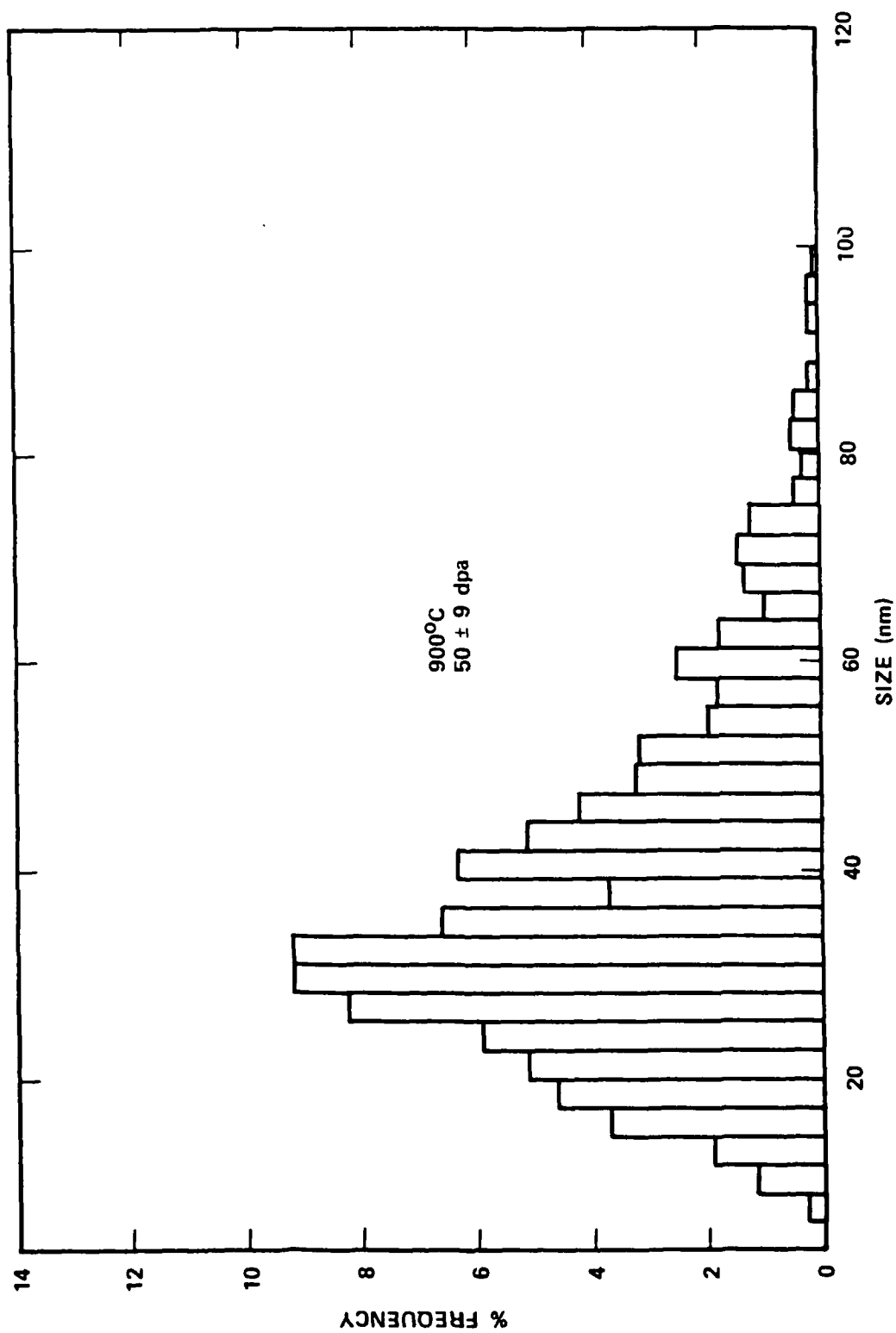
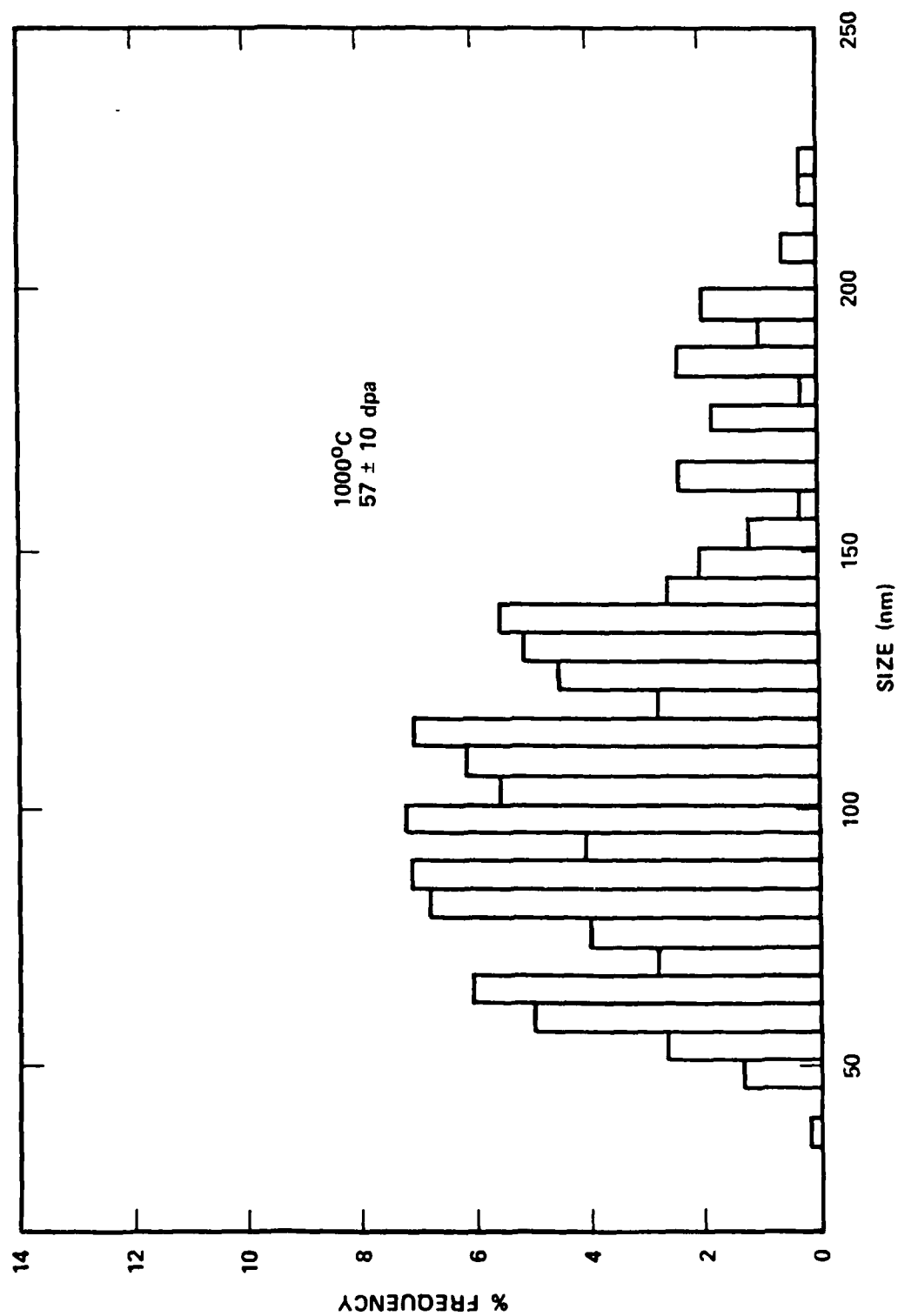Fig. 26. Void size distribution in niobium irradiated at 900°C

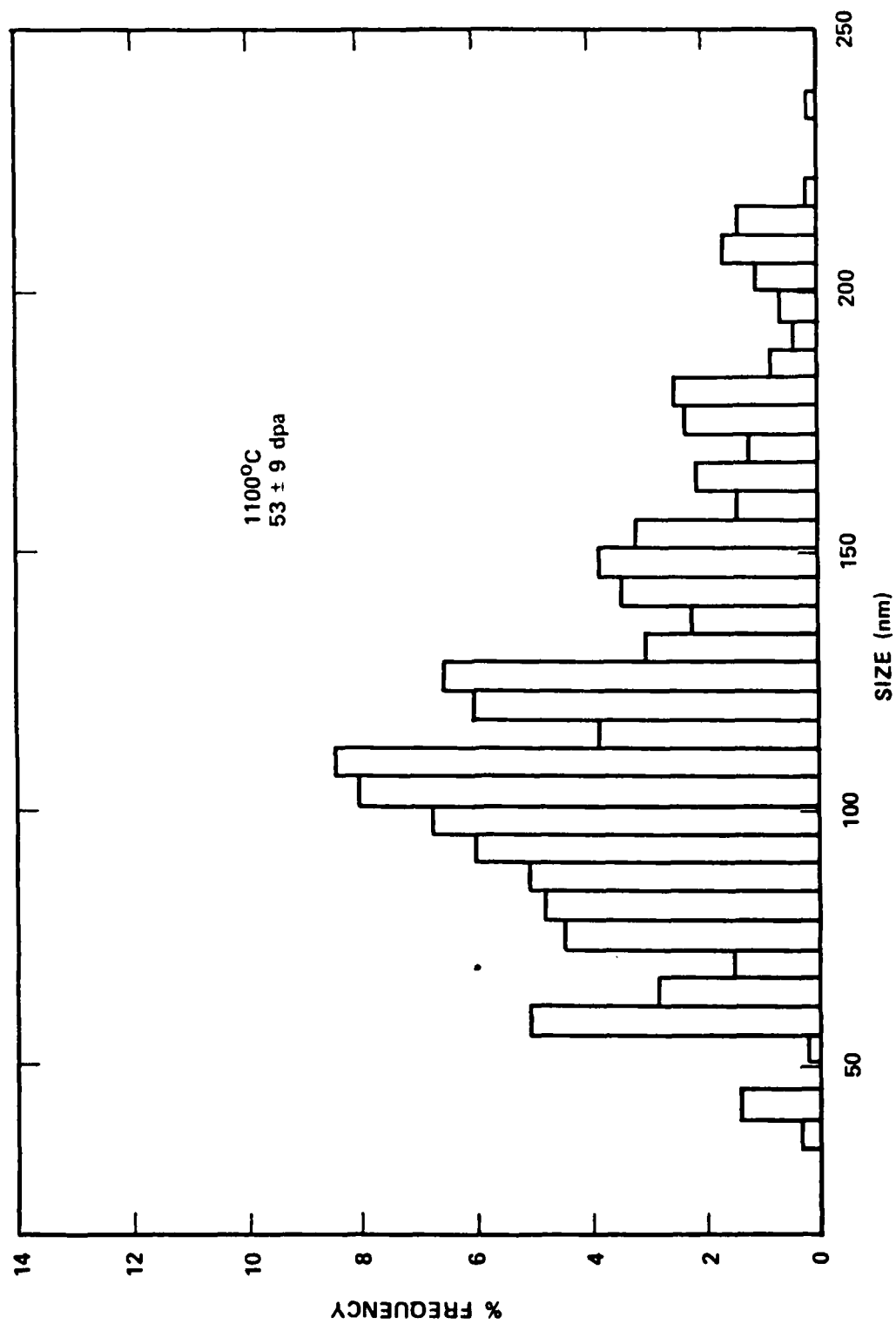Fig. 27. Void size distribution in niobium irradiated at 1000°C

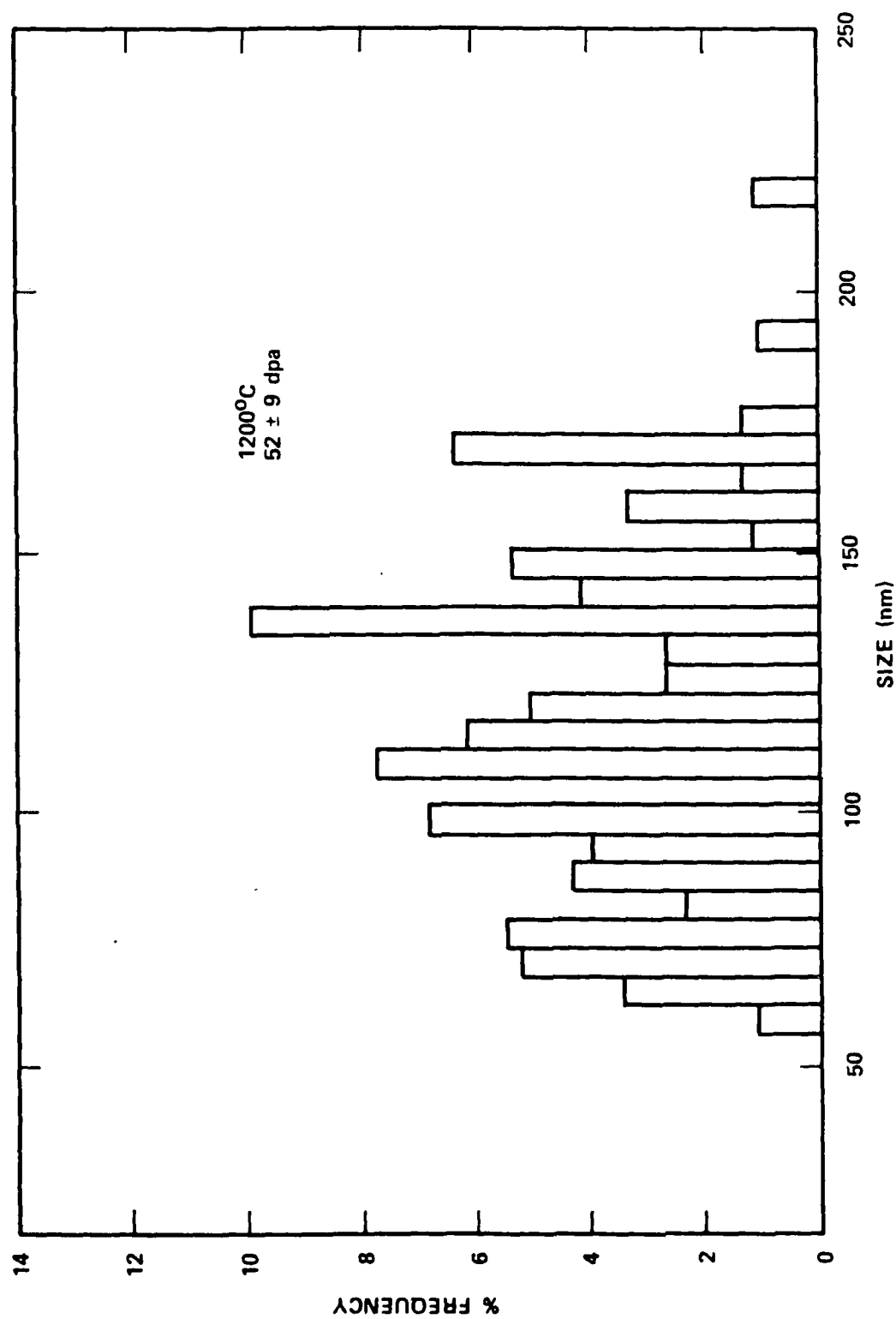Fig. 28. Void size distribution in niobium irradiated at 1100°C

75

Fig. 29. Void size distribution in niobium irradiated at 1200°C

76

loops (vacancy vs. interstitials) produced at this temperature. The dose was reduced to obtain a small density of loops. However, as seen in Fig. 30 a high density (1.2×10^{17} cm^{-3}) of small loops (40 nm) was observed which was very difficult to analyze. It appears that the damage level of 10 dpa was too high to permit loop analysis. Although a lower damage level may increase the probability of this analysis the small loop size will still pose a problem. Therefore, experiments will be designed where the specimens will be irradiated to very low dose levels (0.1-0.5 dpa) and subsequently annealed at higher temperatures (e.g. 1000°C) to increase the loop size by thermal agglomeration prior to the loop analysis. To this end, an ultra high vacuum annealing furnace capable of annealing up to 1100°C has been assembled.

In the specimen irradiated to 10 dpa at 700°C, voids were also observed. Figure 31 shows the micrograph of voids in this specimen. The density of voids was estimated to be 6×10^{16} cm^{-3} and the average void size was 6 nm. The size and density of voids observed indicates that at 700°C the swelling incubation dose has been exceeded.

9.0 DISCUSSION

9.1 Comparison of Results of Present Study with Existing Data

As stated in section 3.0, no data exist on the swelling of self-ion irradiated Nb; therefore, a comparison can only be made with Nb irradiated with ions other than self-ions. Loomis and Gerber[23] have irradiated Nb over comparable temperature and dose ranges with Ni ions. They have also studied the influence of oxygen on the swelling in Nb. These data are compared with the present work. In this comparison, the data of Loomis and Gerber corresponding to an oxygen content of 0.07 a/o were utilized, since vacuum fusion analysis of our material indicated an oxygen concentration of 115 wppm (660 appm, 0.066 a/o).

Figure 32 shows a comparison of swelling data obtained in the two studies. Although the peak swelling values were comparable, significant differences occur in the temperature dependence of swelling. In this study, maximum
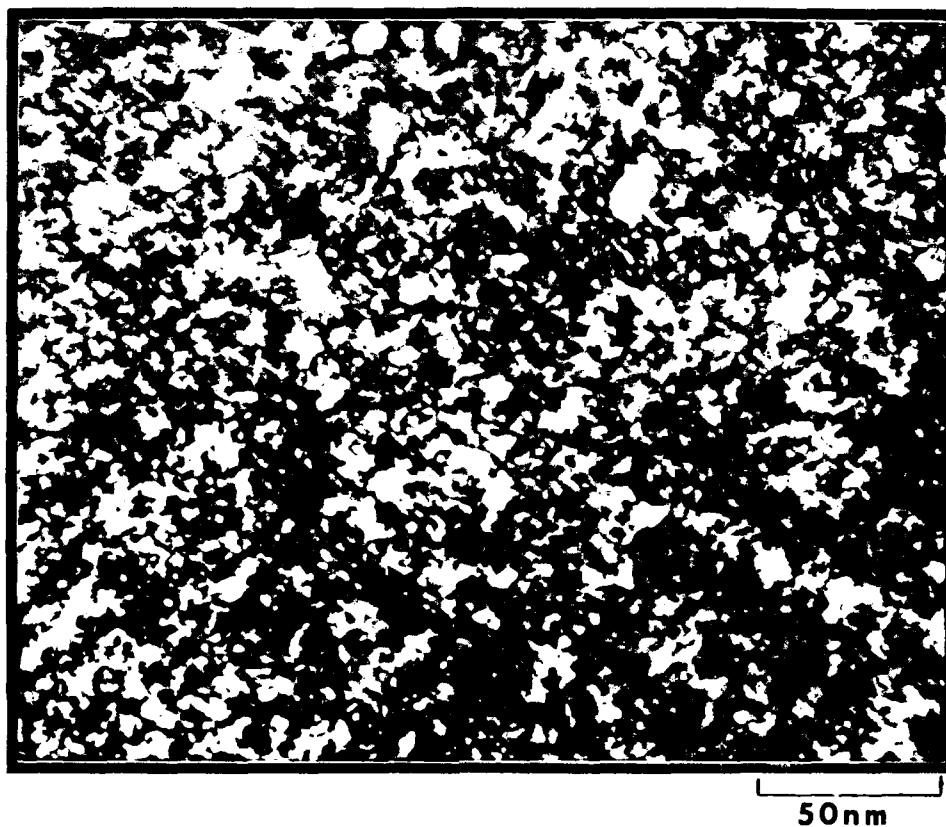
Fig. 30. Loops in weak beam dark field $\vec{g}/3\vec{g}$ Condition in niobium irradiated to 10 ±2 dpa at 700°C $\vec{g}$ = [220]

50nm

Fig. 31. Voids in niobium irradiated to 10 $\pm$2 dpa at 700°C.
$\vec{z} \sim [100]$

Fig. 32. A comparison of swelling data obtained in this work with those of Loomis and Gerber[23]

END
FILMED

DTIC

1·0

2·8   2·5

3·15   2·2

3·5

1·1   4·0   2·0

4·5

1·8

1·25   1·4   1·6

NATIONAL BUREAU OF STANDARDS
MICROCOPY RESOLUTION TEST CHART

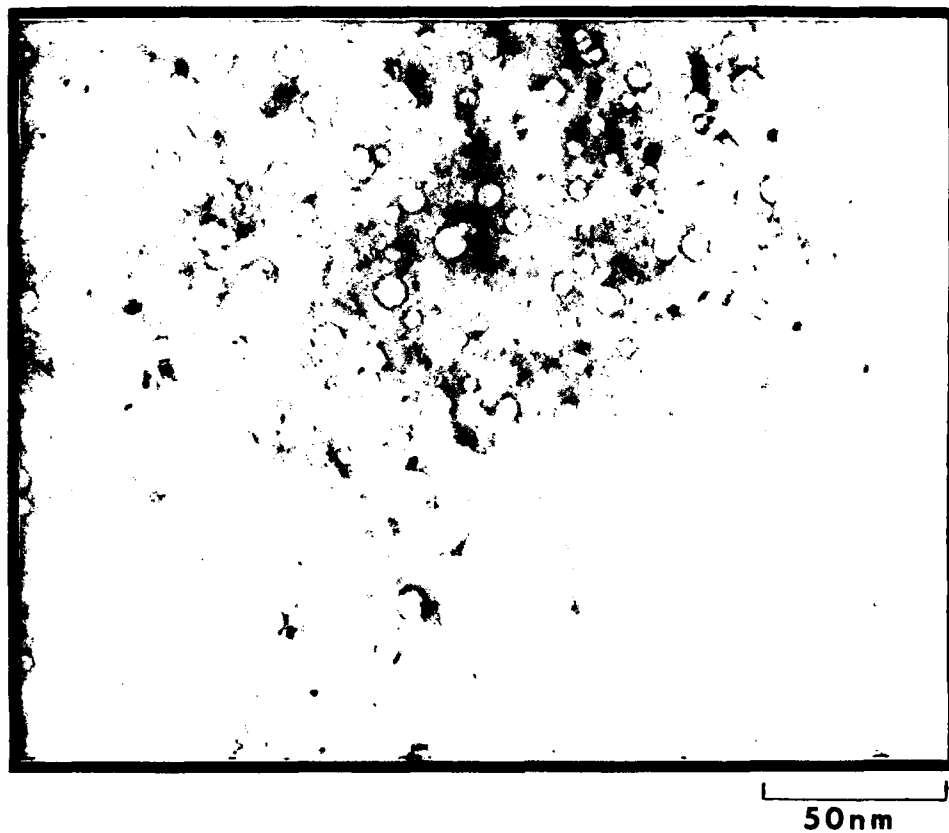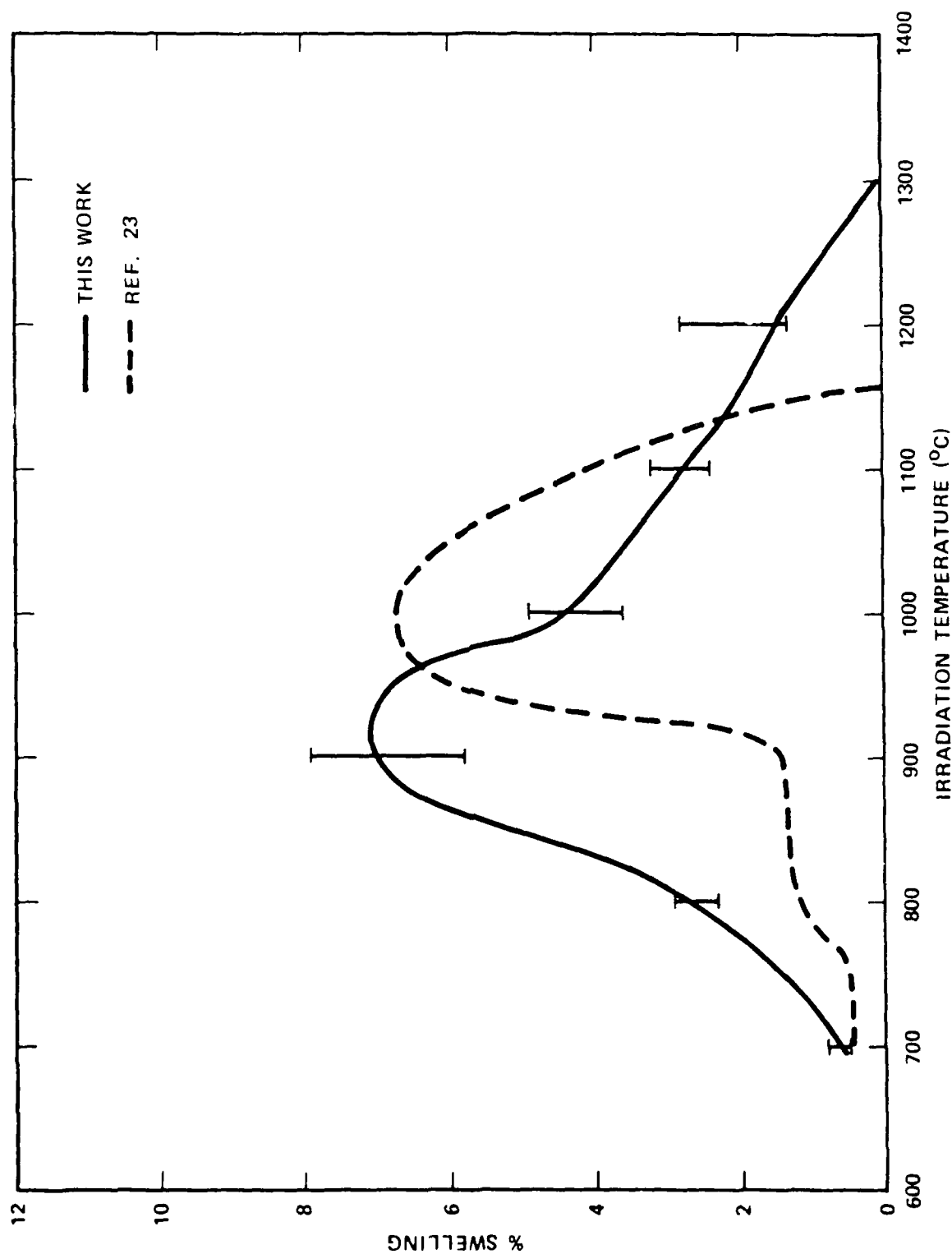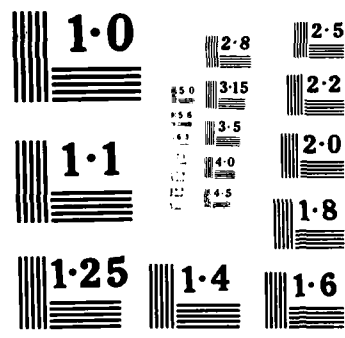swelling occurred at 925°C whereas Loomis and Gerber saw a swelling peak at 1000°C. Also, in their study, swelling occurred over a temperature range of 700° to 1150°C; whereas in this work swelling occurred over a broader temperature range (700°-1300°C). Loomis and Gerber observed no voids at 1150°C, whereas voids were observed at temperatures as high as 1200°C in this work (see Fig. 22). The swelling at 800° and 900°C was also significantly higher.

A comparison of void number densities obtained in the two studies is shown as a function of irradiation temperature, in Fig. 33. A sharp decrease in void number densities as a function of temperature was observed in both studies, although the magnitudes and temperature dependences were different. In this study, the density decreased by a factor 220 over a temperature range of 700°-1000°C, whereas Loomis and Gerber observed a decrease by a factor of 500. The absolute values of the void number densities are significantly different in the two studies. For example, at irradiation temperatures of 800° and 1000°C, the void densities reported here are a factor of 6 lower than those of Loomis and Gerber.

The average void diameters as a function of temperature from the two studies are plotted in Fig. 34. Rapid size increases are observed from 900° to 1000°C in both studies, but the void diameters are significantly higher in the work reported here.

Loomis and Gerber also observed void ordering in niobium containing oxygen in excess of 0.04 a/o and irradiated at 775°C. No void ordering was observed in specimens irradiated at 700° or 800°C in this study.

In an earlier study, Loomis et al[89] observed a double peak in the temperature dependence of swelling in niobium containing 0.006 a/o oxygen, irradiated to 50 dpa with Ni^+ ions. The peaks occurred at ~ 825°C and 1025°C. The maximum void swelling was 12%. The void number densities showed dips at the peak swelling temperatures. At 1100°C the void density increased by an order of magnitude over that at 1000°C. The void diameters also showed two peaks occuring at the peak swelling temperatures. The dislocation
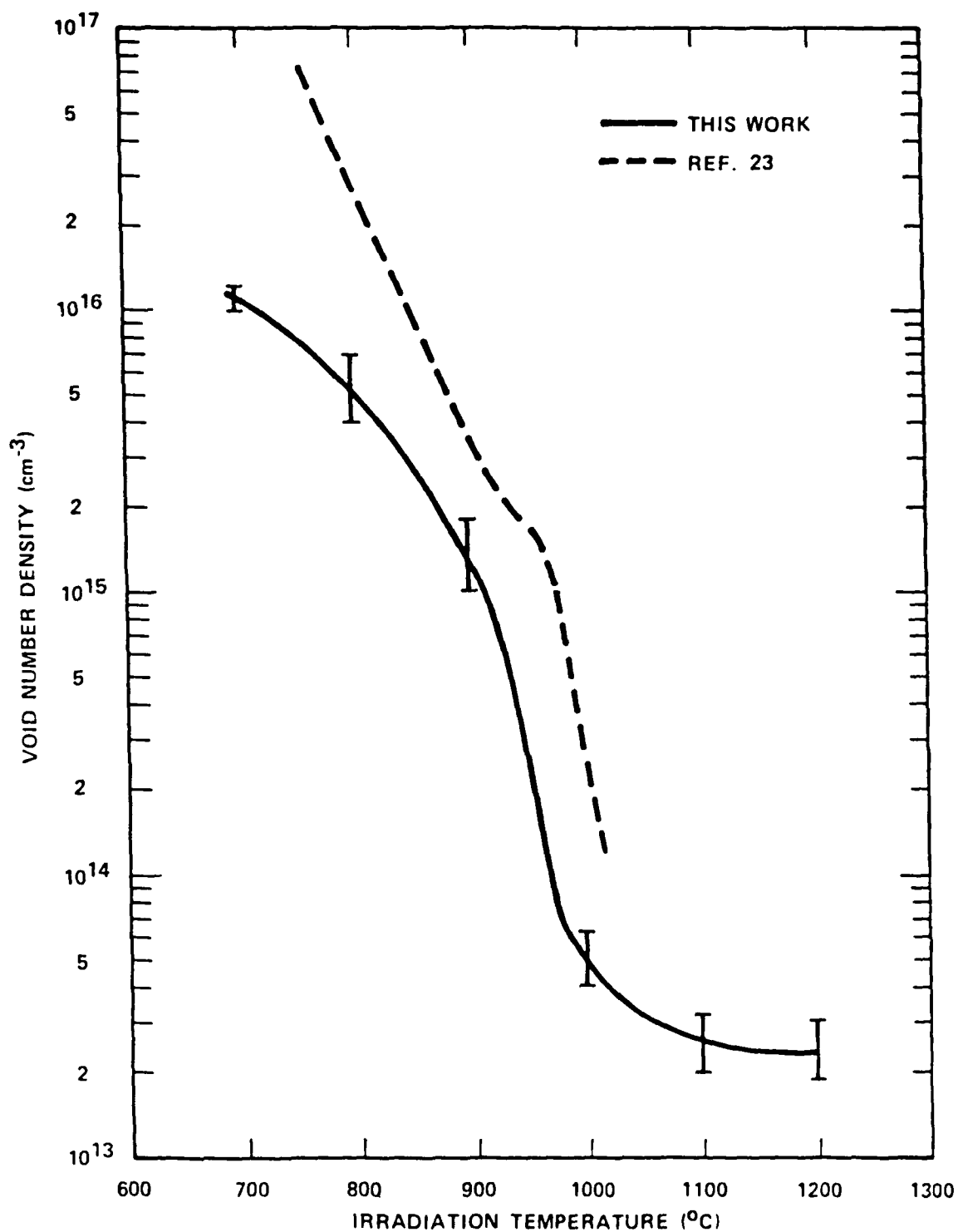
Fig. 33. A comparison of void number densities in this work with those of Loomis and Gerber.[23] Solid line represents data obtained in this work and dotted line shows data of Loomis and Gerber[23]
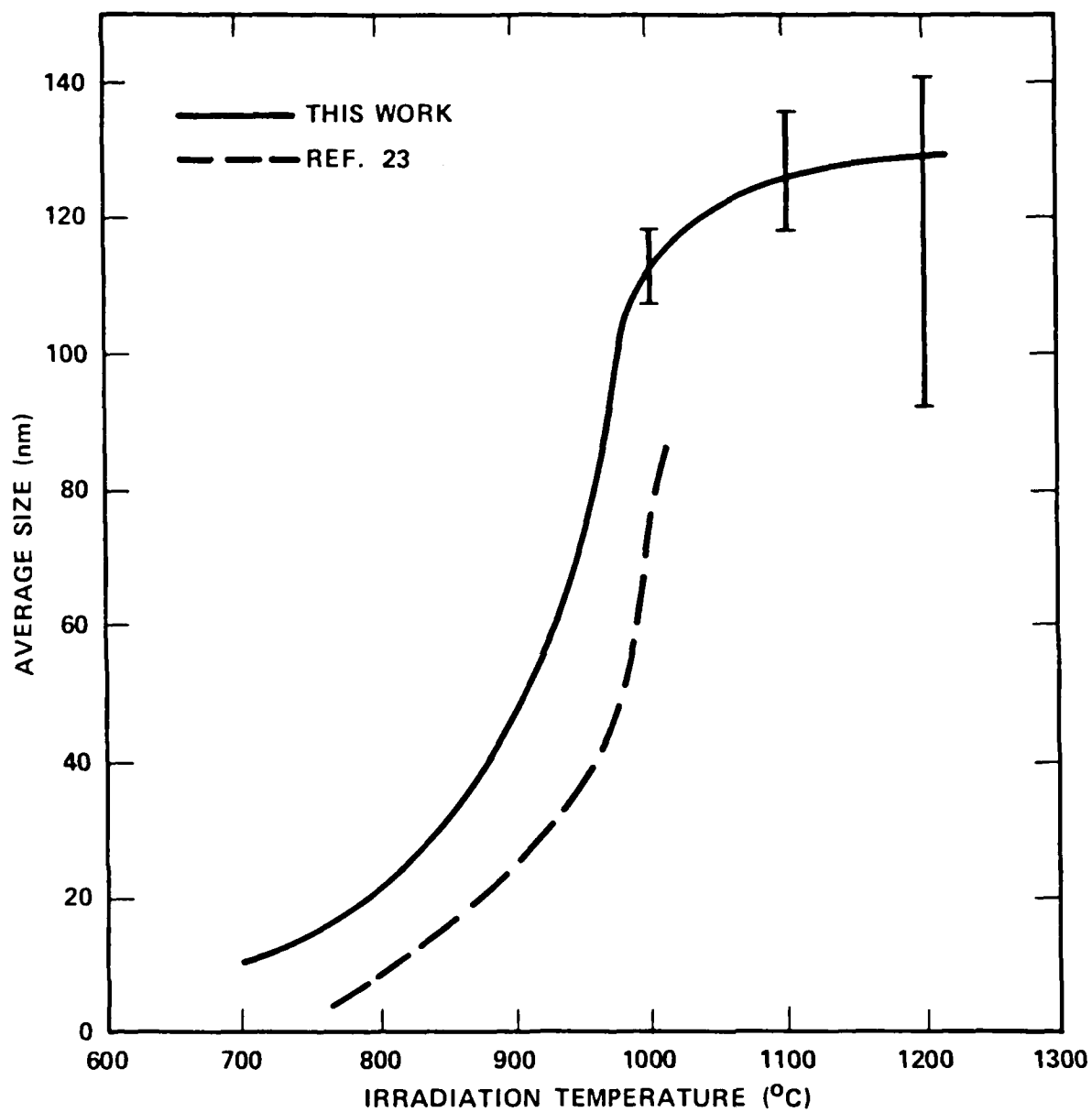
Fig. 34. A comparison of average void sizes in irradiated niobium between this study and that of Loomis and Gerber[23]

densities were of the order of 10^9 cm^{-2} and average dislocation loop and spot diameters varied from 10 nm to 98 nm between 800° and 1100°C. No swelling was observed at temperatures above 1150°C. These data cannot be compared to the data of the present study because of an order of magnitude difference in starting oxygen content and possible continuous oxygen pickup during irradiation as suggested by the authors.

The difference in the results of this study and that of Loomis and Gerber[23], especially with regards to the temperature dependence of swelling, void number densities, and average void sizes, cannot be accounted for by the differences in pre-irradiation oxygen levels and oxygen pickup during the irradiation. This is because, at oxygen levels of 0.08 a/o, saturations in void number densities and average void sizes were observed by Loomis and Gerber[23]. Also, the temperature dependence of swelling was reported to be nearly independent of oxygen content.

The only major difference between the two studies is the ion species used to irradiate the niobium specimens. Loomis and Gerber[23] used ^{58}Ni$^+$ ions whereas in this study self-ions were used. Chemical effects between the nickel ions and either niobium or oxygen or both cannot be ruled out at this time. Injected interstitials are known to influence swelling and micro-structure; the examination of the impact of this effect on the results of this work has not yet been completed.

9.2 Comparison of Experimental Data and Model Calculations

A major objective of this program is development of a model for swelling in body centered cubic metals based on the formalism of chemical reaction rate theory. The basic equations of the model and preliminary calculations for niobium were presented in Section 5. The results of the calculations were used to determine conditions for the first set of experiments. In this section, the experimental results are compared with model calculations in order to test the validity of the theoretical assumptions that have been made, to evaluate values of critical model parameters, and to determine areas where experiments that lead to refinement of the model can be performed.

The results of three sets of calculations are presented. The first set, which is a determination of the critical cavity size required for growth as a function of temperature, provides an explanation for the high-temperature cutoff observed for swelling. Results of the second set, evaluation of sink strength ratios from the experimental data, have implications with respect to the values of the loop bias factors and the temperature dependence of loop growth kinetics. Finally, calculations of swelling as a function of temperature show that swelling depends strongly on interactions of impurities with point defects and development of the dislocation structure before the onset of swelling.

9.2.1 Critical Size for Cavity Growth

The differential equation that describes the rate of change of the cavity radius with time [Eq. (34)] contains two terms which are respectively the rate at which the cavity radius increases due to net vacancy absorption and the rate at which the radius decreases due to interstitial absorption per unit time increment. The magnitudes of these terms depend on the cavity radius; appearing directly in the conversion of defect volume to change in radius and in the thermal vacancy emission term [Eq. (25)] and indirectly because of the dependence of the steady-state point defect concentrations on the total sink strength [Eq. (10)], which includes a term for the cavity sink strength [Eq.(7)].

In order for a cavity to grow, the cavity radius must be greater than the "critical radius" r_v^{crit}, which will be defined here as the radius at which the vacancy and interstitial absorption terms balance. An expression for r_v^{crit} can be obtained from Eq. (34) by setting the derivative to zero and solving:

$$r_v^{crit} = [\frac{kT}{2\gamma\Omega} \quad \ln (\frac{Z_v^C D_v C_v - Z_I^C D_I C_I}{Z_v^C D_v C_{vc}^{th}})]^{-1} \tag{41}$$

The terms in Eq. (41) have been defined previously in Section 5.

85

The value of the critical radius depends on the sink structure, the bias parameters, dose rate, and temperature. Using the average void densities and dislocation densities given in Table IV, and the experimental temperatures and dose rate, the critical radius was calculated as a function of temperature. The results are shown in Fig. 35 (Curve labelled 0). Bias parameters Z_V^C, Z_I^C were assumed to be one, and Z_I^{nd} to be 1.05. Loop density was taken as zero, since the network is established at doses of the order of 10-20 dpa.

Evaluation of the critical radius is important for analysis of the swelling data for several reasons. First, it establishes the end of the nucleation process for a given set of experimental conditions. Once a cavity has attained this size it is assumed to continue growing at a rate defined by Eq. (34). In a practical sense, this means that the value of r_v^{crit} is used as the initial cavity radius when the swelling equation is solved. Second, an estimate of the incubation period for swelling at each temperature can be obtained if the measured swelling values are fit to those calculated using the model equations. The difference between the actual irradiation times and the times at which the model calculations reach the measured values provide these data. Finally, the rapid increase in the critical radius at high temperatures explains the observed absence of cavities and the lack of swelling at 1300°C. No cavity embryo can reach the critical radius at this temperature in the absence of a large quantity of gas acting to stabilize the cavity by reducing thermal emission of vacancies. The cavity nucleation rate therefore drops to zero.

9.2.2 Sink Strength Ratios

The data given in Table IX can be used to estimate sink strength ratios for the microstructure observed in the implanted niobium specimens. Since experimental data for the dislocation loops are not available, values for the loop densities, bias factors, and sizes must be assumed in order to perform the calculations. $Z_I^{\ell 2}$, the bias factor of <111> loops for interstitials, was assumed to lie between 1.0 and 1.1 and $Z_I^{\ell 1}$ was taken to be equal to $b_1 Z_I^{\ell 2}/b_2$. The <111> loop density was assumed to be between 10^{11} and 10^{16} cm^{-3}; the <100> loop density was assumed to be a factor of 10^{-5} lower. The capture area factors, $4\pi r^*$, for both types of loop were taken as 10^{-6} cm.
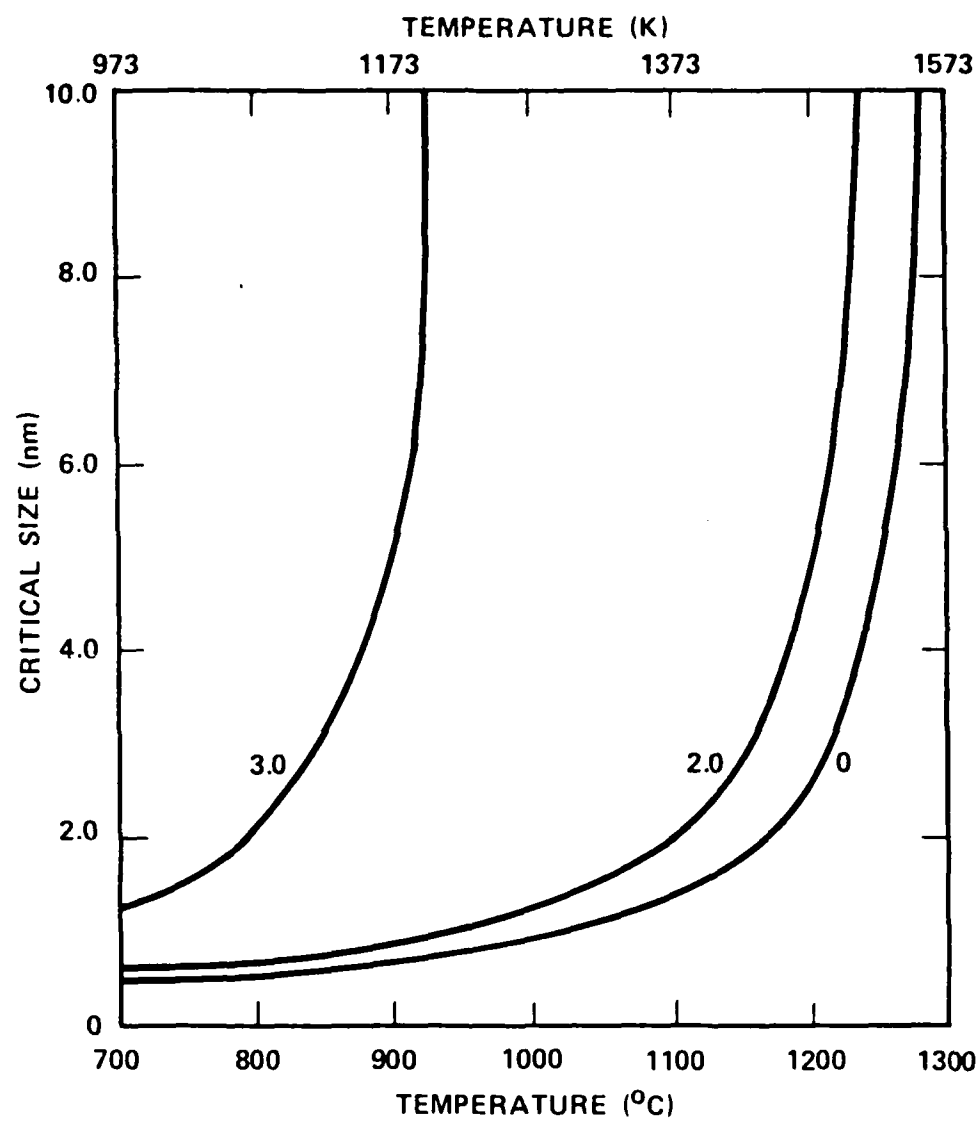
Fig. 35. Critical radius as a function of temperature for three values of the interstitial-oxygen binding energy, E_B. Curves are labelled by E_B in eV.

87

Results of the calculations are summarized in Table X. Specimens are identified by the implantation temperature, given in the first column. The range of values of the sink strength ratio, S_I/S_V, obtained for the range of parameters given above are listed in the second column. The final column contains a bounding value Z_{max} for $Z_I^{\ell 2}$. If $Z_I^{\ell 2}$ is less than Z_{max}, then S_I/S_V is greater than $Z_I^{\ell 2}$ and the condition for shrinkage of <111> loops is met. The value of Z_{max} is independent of the assumed <111> loop density for densities from 10^{11} to 10^{16} cm^{-3}.

Table X. Calculated Sink Strength Ratios

Temperature (°C)	S_I/S_V	Z_{max}
700	1.017-1.021	1.018
700	1.027-1.033	1.029
800	1.020-1.027	1.022
900	1.022-1.033	1.025
1000	1.034-1.057	1.044
1100	1.036-1.059	1.046
1200	1.031-1.062	1.044

A rough estimate of loop densities was made using the micrographs given in Figs. 18-23 and a value of approx. 10^{14} cm^{-3} was obtained. For this density, the calculated sink strength ratio is independent of $Z_I^{\ell 2}$, for $Z_I^{\ell 2}$ between 1.0 and 1.1, at all temperatures, and is given by Z_{max}. In addition, it depends only slightly on temperature, with an average value of 1.023 between 700° and 900°C and 1.045 between 1000° and 1200°C. One implication of this result is immediately apparent; if $Z_I^{\ell 2}$ lies between 1.023 and 1.045, <111> loops will grow at low temperatures and shrink at high temperatures.

9.2.3 Calculated Swelling Curves

Theoretical swelling curves were obtained from the model equations for three different sets of assumptions. Each will be discussed in turn, to indicate how the analysis developed.

For the first calculation, the experimental dislocation density was taken as the value for the network density with bias equal to 1.05. The average cavity density was used for N_c, and loop densities were assumed to be zero. (This set of assumptions is equivalent to assuming that the swelling model used for face centered cubic metals is valid.) The total swelling time was taken equal to the irradiation time; nucleation is thus assumed to occur at t=0. The results of this calculation are given in Fig. 36 (Curve labeled 0). The experimental results are indicated in Fig. 36 by the dashed curve, with the measured points and error bars shown. It is apparent that the calculation does not reproduce the data, overpredicting the low temperature results by an order of magnitude, and the high temperature results by roughly a factor of three.

The first modification of the initial assumptions was the inclusion of an incubation time for swelling. At the onset of irradiation, a sequence of events occurs to set the stage for the swelling phenomenon. This sequence includes establishment of steady-state point defect concentrations, loop nucleation, loop growth, and cavity nucleation. Loop growth and network formation may be completed within the initial transient period, or may extend into the cavity growth regime. (We have assumed that the former is the case, since the network density is equal to the measured dislocation density.) Cavity growth is significant only after this sequence is completed. The extent of the initial transient period depends on temperature, dose rate, and impurity concentrations and requires of the order of 1-10 dpa. A theoretical estimate can be obtained if a full-scale nucleation calculation is performed.

To examine the effect of an incubation period on the calculated swelling, four incubation times, corresponding to doses of 1,5,10, and 15 dpa, were assumed, and the calculations redone. The results are shown in Fig. 36, where the curves are labelled by the incubation dose. As can be seen from the curves, inclusion of an incubation period does reduce the calculated swelling, but the reduction is not large enough to cause agreement between the calculations and the data. For example, with an incubation dose of 10 dpa, the calculated swelling is reduced by roughly 25 to 30 percent over the entire temperature range.
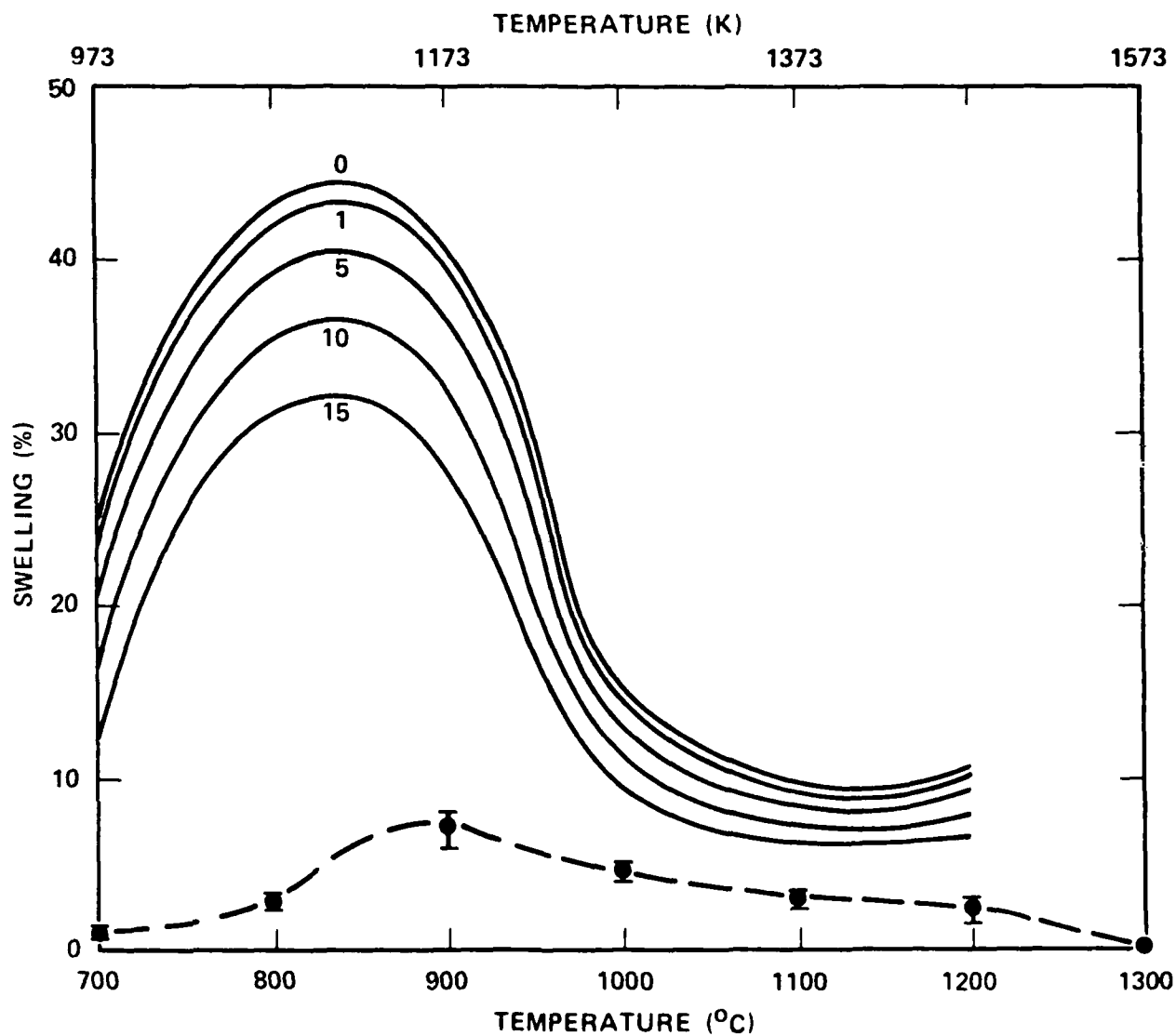
89

Fig. 36. Calculated swelling as a function of temperature. Curves are
labelled by the assumed value of the incubation dose in dpa.
Experimental data are given by the dashed curve.

At this point, two major effects remained to be considered within the context of the model as it has been developed to date: those due to the two types of loops and their differing biases for interstitials, and those due to impurities. At the doses examined, it is apparent from the micrographs that the evolution of the dislocation structure has advanced into the stage where the network dominates the microstructure, and data on loop types, densities, and sizes can not be obtained. Calculation of the impact of loop properties on swelling is therefore difficult and will be deferred until low dose data is available. The third set of swelling calculations focused on impurity effects.

As mentioned previously in Section 5.4, trapping of point defects by impurities can have a significant effect on the cavity growth rate and hence the swelling rate. Measured oxygen concentrations in the material used in this work are roughly 0.07 appm. Work by Loomis and Gerber[23] has shown that concentrations of this order are sufficient to affect swelling, leading to a reduction in swelling relative to that in low-oxygen material. If we assume that the mechanism involved is trapping of niobium interstitials by oxygen, the diffusion coefficient D_I appearing in the model equations must be replaced by the effective diffusion coefficient given in Eq. (40). This introduces the interstitial-oxygen binding energy E_B as a parameter in the model, since its value has not been measured.

Preliminary calculations showed that binding energies of the order of 2 eV are needed to produce calculated swelling curves that correspond to the experimental curves. A series of calculations was then made with the binding energy ranging between 1.75 and 2.1 eV. Two incubation doses were used: 0 and 10 dpa. The results are shown in Figs. 37 through 40 where the calculated swelling is plotted as a function of binding energy for the six experimental temperatures. Each experimental point was then used, along with its error bar, to determine the range of E_B values that would produce a fit. The procedure is illustrated in Fig. 37 for 900°C. Results for all temperatures are given in Table XI for zero incubation dose, and in Table XII for an incubation dose of 10 dpa. As can be seen from the tables, there is some scatter in the results, with an average value of 1.995 eV for 0 dpa and 1.943 eV for 10 dpa. These average values were used in the model equations
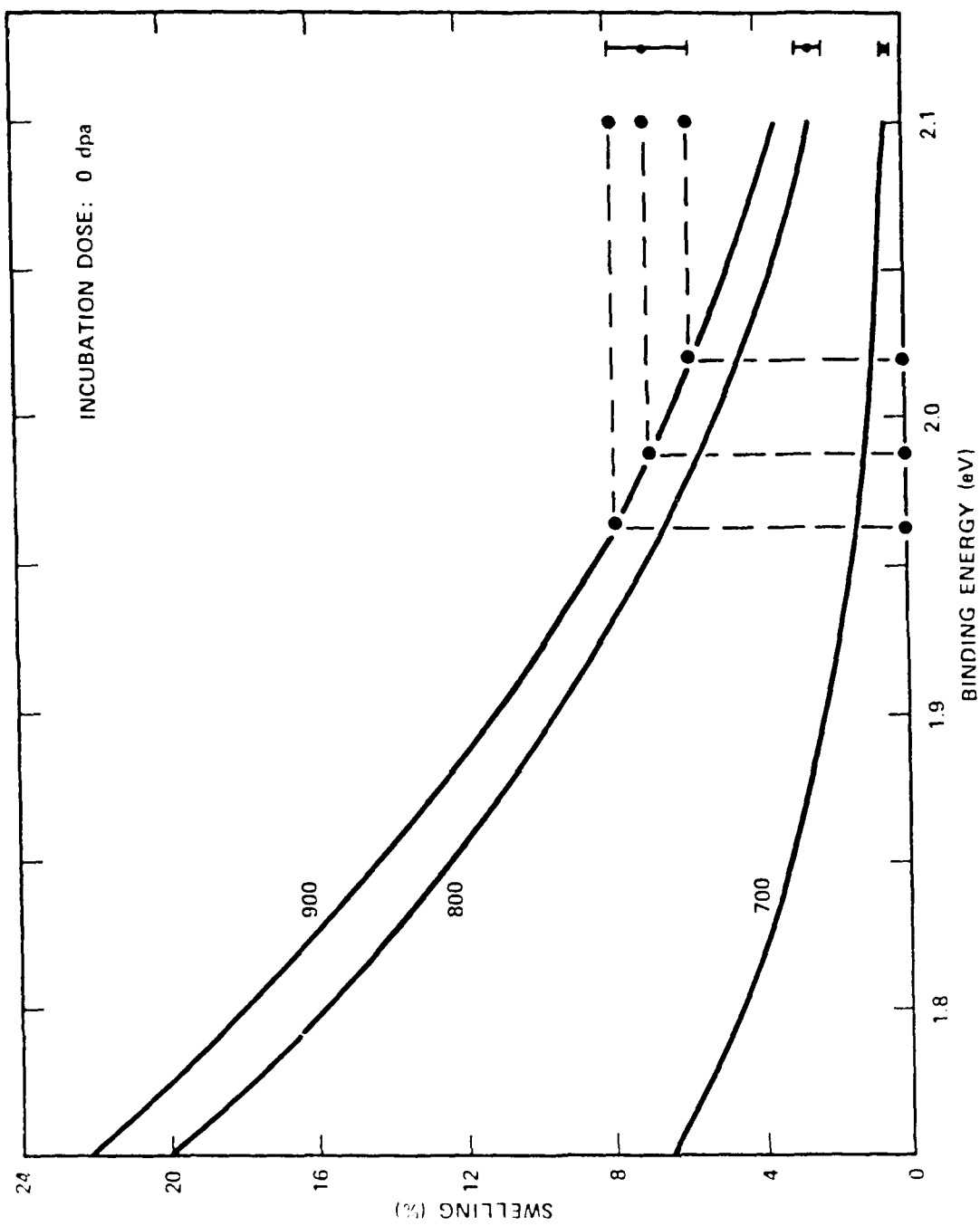
91

Fig. 37. Calculated swelling as a function of interstitial-oxygen binding energy for an incubation dose of 0 dpa. Curves are labelled by temperature in °C. Experimental points are shown near the right margin, for 700°, 800°, and 900°C in ascending order.
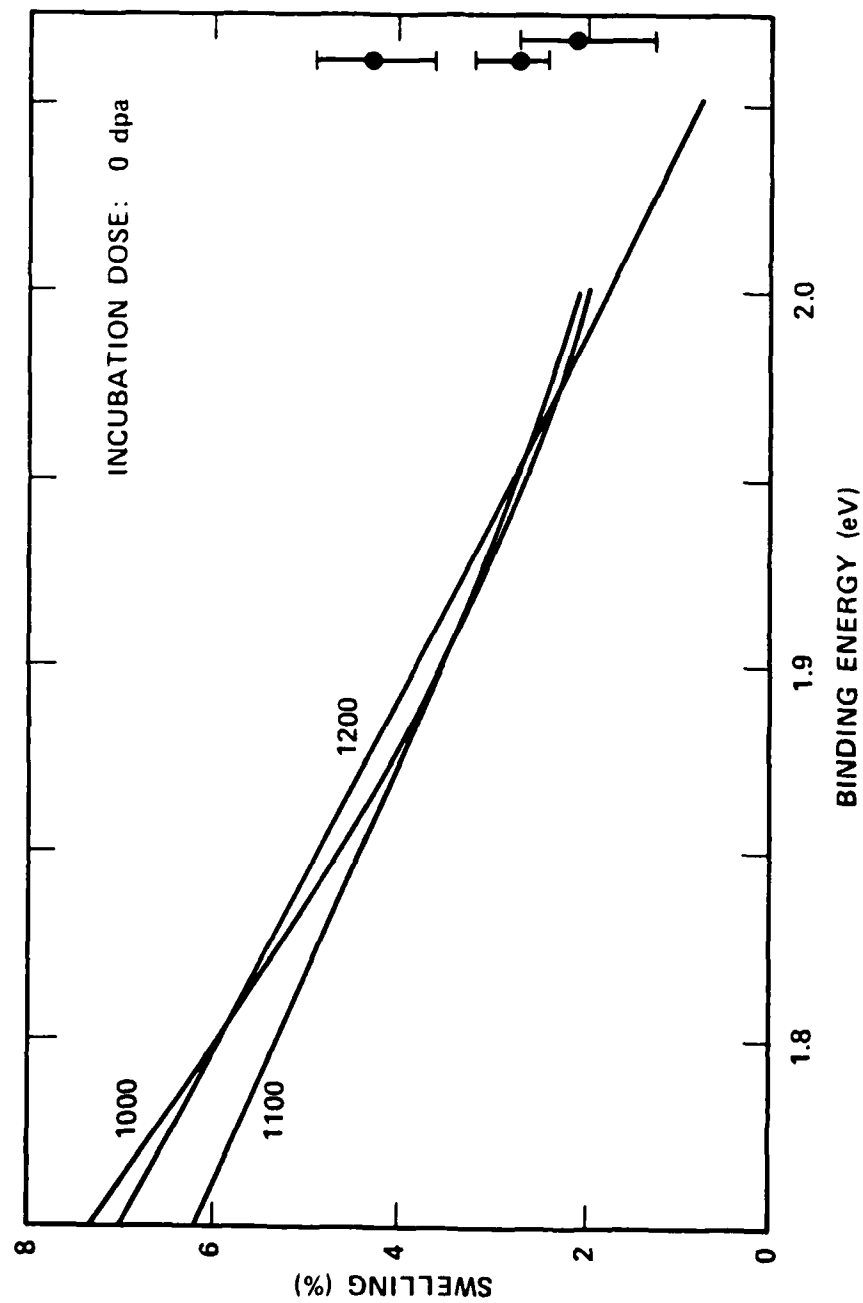
92

Fig. 38. Calculated swelling as a function of interstitial-oxygen binding energy for an incubation dose of 0 dpa. Curves are labelled by temperature in °C. Experimental points are shown near the right margin, for 1000°C, 1100°C and 1200°C in descending order.
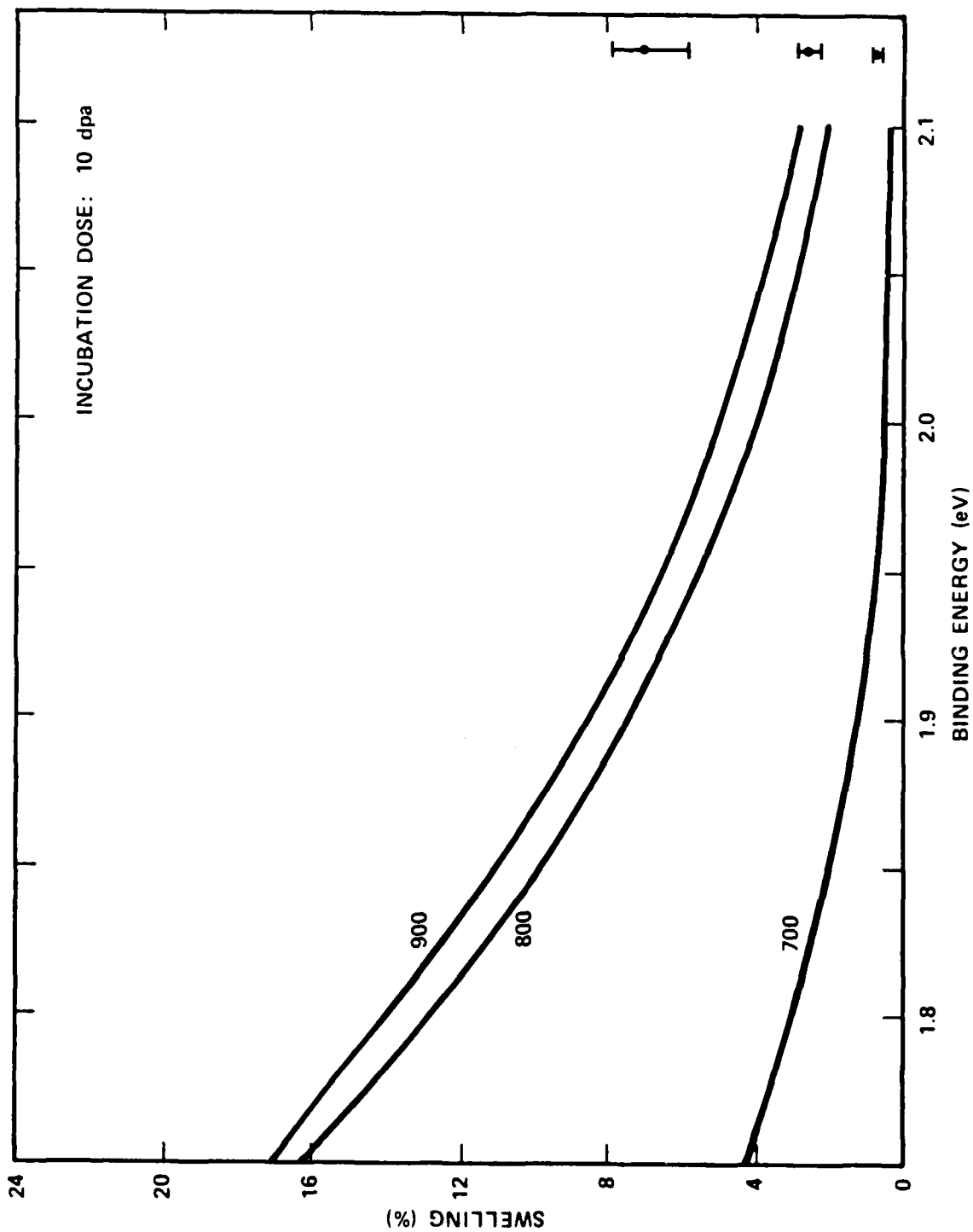
Fig. 39. Calculated swelling as a function of interstitial-oxygen binding energy for an incubation dose of 10 dpa. Curves are labelled as in Fig. 37.
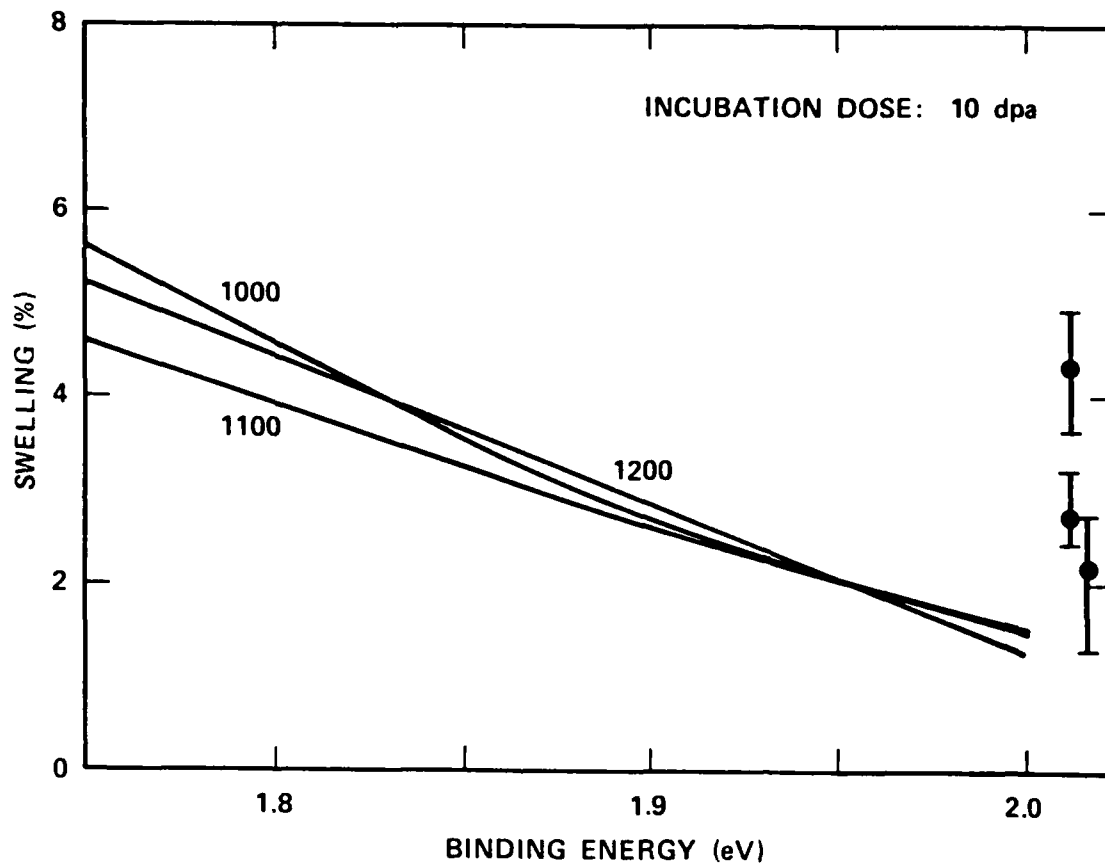
94

Fig. 40. Calculated swelling as a function of interstitial-oxygen binding energy for an incubation dose of 10 dpa. Curves are labelled as in Fig. 38.

and swelling calculated as a function of temperature, as shown in Fig. 41. Triangles are for an incubation dose of 0 dpa, and circles for 10 dpa.

Table XI. Fit of Binding Energies to Swelling Data
Incubation Dose: 0 dpa

Temperature (°C)	Range E_B (eV)	Mean Fit
700	2.088-2.049	2.068
800	2.130-2.094	2.111
900	2.021-1.966	1.987
1000	1.898-1.840	1.866
1100	1.976-1.921	1.954
1200	-1.952	1.982
	Average	1.995

Table XII. Fit of Binding Energies to Swelling Data
Incubation Dose: 10 dpa

Temperature (°C)	Range E_B (eV)	Mean Fit
700	2.026-1.986	2.004
800	2.092-2.055	2.073
900	1.972-1.917	1.939
1000	1.846-1.781	1.810
1100	1.917-1.853	1.892
1200	-1.904	1.942
	Average	1.943

The two combinations of incubation dose and binding energy give approximately the same fit to the data. Significant discrepancies occur at two temperatures, 800° and 1000°C. At the former temperature, the swelling is overpredicted by roughly a factor of two; at the latter, underpredicted by the same factor.
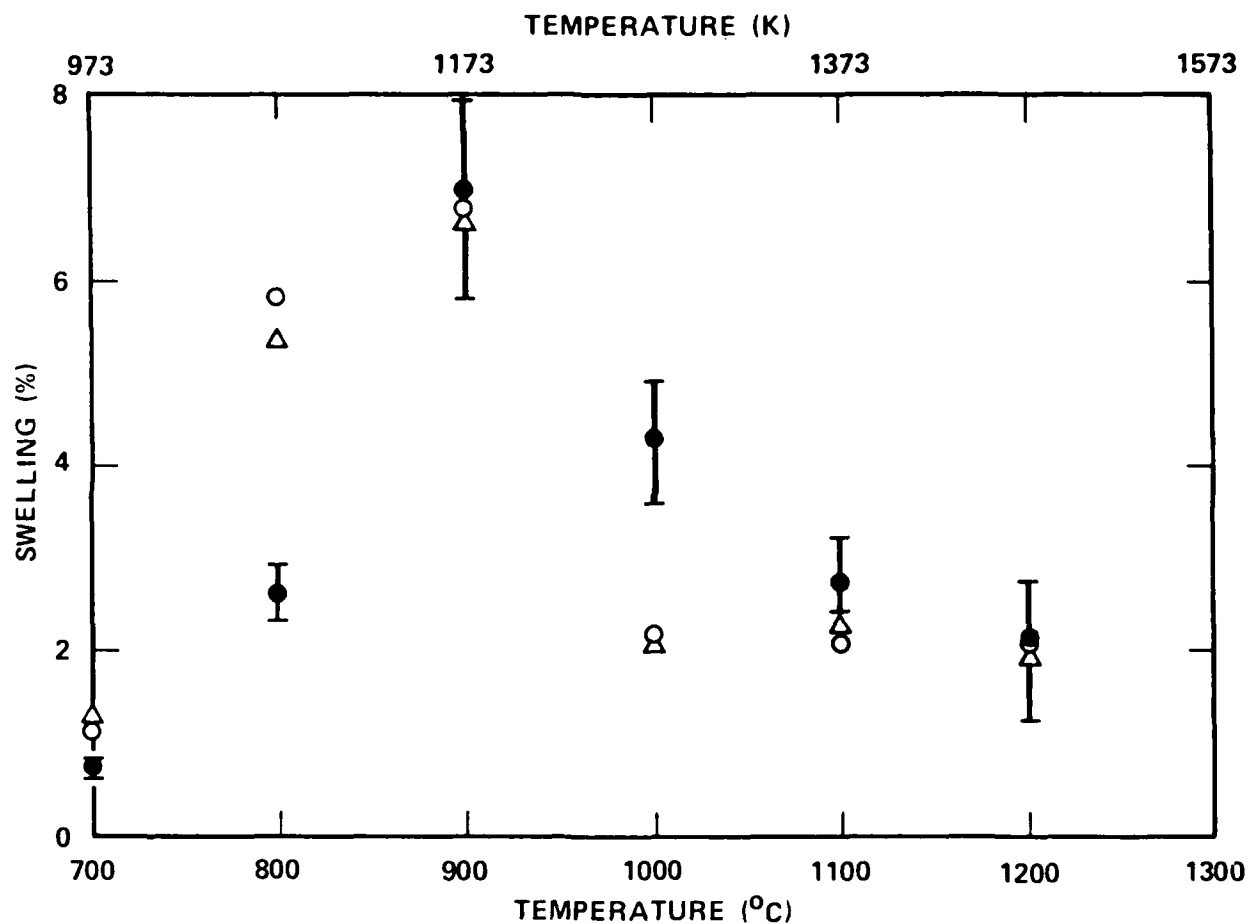
Fig. 41. Calculated swelling as a function of temperature for two
combinations of incubation dose and interstitial-oxygen binding
energy: Δ (0 dpa, 1.995 eV); O (10 dpa, 1.943 eV). Experimental
points are shown with error bars.

97

Whether the values obtained for E_B are reasonable can be tested to a limited extent by looking at the effect of the binding energy on the critical radius. Trapping of interstitials by oxygen reduces the diffusivity of interstitials and changes r_v^{crit} [see Eq. (41)]. Calculations of r_v^{crit} as a function of temperature were done for a range of assumed binding energies, and r_v^{crit} increases as binding energy increases for a fixed temperature. Values of r_v^{crit} are plotted in Fig. 35 as a function of temperature for binding energies of 2 and 3 eV. As can be seen from the figure, there is a large shift of the high temperature portion of the curve toward lower temperatures as the binding energy increases from 2 to 3 eV. The shift when E_B changes from 0 to 2 eV is relatively small in comparison. Any increase in assumed binding energy, which would result in a better fit to the 800°C data point, for example, would result in critical radii at high temperatures that would be unacceptably large. Since cavities are observed at 1200°C, r_v^{crit} must remain relatively small until this temperature is exceeded. For binding energies near 2 eV, r_v^{crit} is 5 nm, a value that is somewhat high. A reduced binding energy is therefore more reasonable than an increased one.

By examination of the cavity distribution after implantation, Horton [91] has recently determined the critical cavity radius in Fe – 10% Cr irradiated at 577°C (.5T_m) with 4 MeV Fe^{++} ions to a damage level of 30 dpa. The value obtained was 2.5 nm, a result that is of the same order as those calculated in the present work for temperatures near 1200°C with binding energies between 0 and 2 eV.

As indicated in the discussions of experimental results, measured dislocation densities in Ni-implanted niobium are roughly an order of magnitude lower than those measured in the present work. Because of possible deformation during sample preparation, the densities given in Table IX may be high. A series of swelling calculations was performed in order to determine the effect of the dislocation density. Reduction of measured values of dislocation density by an order of magnitude led to a significant reduction in the calculated swelling relative to the first series of calculations (see Fig. 36 , curve labelled 0). At 700°C, swelling was reduced by a factor of 5, and at 900°C by a factor of 4. For the three high temperature points, there was only a small reduction, of

the order of 10%. If warranted by measurements of deformation induced during
sample preparation, modification of the experimental dislocation densities and
refitting of the swelling data to the model calculations would give oxygen-
interstitial binding energies that are lower than those determined for the
conditions as given. Determination of preparation-induced deformation, if any,
is therefore important.

9.3 Suggested Areas of Experimental and Theoretical Investigation

The combination of experimental data and calculational results indicate several
areas that can be investigated both theoretically and experimentally to aid in
the development of the theory for swelling in body centered cubic metals.
These include:

- o   Low-dose microstructural evolution

- o   Cavity growth kinetics

- o   Loop and cavity nucleation

- o   Oxygen trapping

The first two would require experimental work, the second two, primarily
theoretical effort.

A series of experiments at low doses could provide data on the development of
the conditions that prevail at the onset of swelling. For example, the data
for 10 and 32 dpa at 700°C indicate that coalescence of small cavities may
occur, since the cavity number density at the lower dose is greater than that
at the higher. The swelling model does not currently include coalescence as
a possible growth mechanism. In addition, data on the dislocation loops,
including types, densities, and sizes, is needed in order to evaluate the
possible effects of the presence of both <100> and <111> loops on swelling.

Data on the growth rate of cavities at moderate doses (between 10 and 50
dpa), obtained from experiments with total dose as a variable, could be
directly compared with predicted growth rates. An outcome of this would be

99

an experimental determination of the incubation dose, which in the present analysis was used as a parameter, independent of temperature.

A theoretical estimate of the incubation dose can also be obtained from a three-component nucleation calculation. Nucleation models based on the chemical-reaction-rate formalism are available, and a calculation that includes <100> and <111> loops as well as cavities is relatively straight-forward. Predictions of low-dose loop growth kinetics would be automatically a part of the output of this type of computation. As can be seen from the data, the cavity density drops significantly between 900° and 1000°C, and the dislocation density flattens out as a function of temperature. As a result, the calculated sink strength also changes. The key to understanding the temperature dependence of the densities lies in understanding what controls cavity nucleation.

From the swelling calculations it is clear that any impurity trapping (in this case oxygen) could be significant in determining swelling behavior. An investigation of oxygen effects in niobium would require extensive experi-mental and analytical work, and is currently not a major focus of the pro-gram. Loomis, however, has done extensive work on oxygen in niobium, and his published data provide a test for any swelling model that includes oxygen as a critical component. As a preliminary to performing experiments involving variable oxygen concentrations, it would be useful to analyze Loomis' data with our model. This could have the additional benefit of explaining the differences between the two data sets.

10.0 SUMMARY AND CONCLUSIONS

During Phase I (first year) of a three year program to investigate irradia-tion swelling mechanisms in refractory metals, a theoretical model based on the chemical reaction rate formalism was developed specifically for body centered cubic metals. Calculations were performed for a selected metal, niobium material, i.e. niobium. A special source preparation method was developed to produce a niobium hydride target material. The use of this target in the ion source resulted in an output of Nb ions of sufficient

energy and flux to permit, for the first time, ion bombardment studies of niobium with self-ions. Irradiated experiments were conducted at the Argonne National Laboratory accelerator facility. Microstructural data obtained from transmission electron microscopy (TEM) were compared with the existing data and with the theory and further experimental directions were developed. The experimental results showed:

1. A peak swelling of 7% was obtained at 900°C in niobium (0.07 a/o oxygen) irradiation with 5.3 MeV Nb^{++} ions at a nominal dose of 50 dpa and a dose rate of 6 x 10^{-3} dpa/s.

2. Swelling occurred over a temperature range of 700° to 1200°C. Swelling was not observed at 1300°C.

3 The dislocation structures were well developed.

A comparison of data from this study and those obtained by Loomis and Gerber on niobium irradiated with nickel ions showed several differences between the data sets. These differences may be due to the use of Ni ions in the earlier studies.

A comparison of model calculations with the experimental results showed a reasonable agreement between the calculated and experimental swelling values when trapping of interstitials by oxygen was included. An interstitial-oxygen binding energy of approximately 2 eV/atom provided the best fit to the data. Microstructural data were utilized to calculate sink-strength ratios whose average values as a function of temperature ranged from 1.018 to 1.046.

The experimental results and their theoretical analysis suggest the following areas for further investigation

(1) Microstructural evolution at low dose
(2) Kinetics of cavity growth
(3) Trapping effects due to oxygen
(4) Self-interstitial effects

11.0 REFERENCES

1. C. Cawthorne and E.J. Fulton, "Voids in Irradiated Metals", Nature, 216, pp. 575-576 (1967).

2. E.A. Little and D.A. Stow, "Void Swelling in Irons and Ferritic Steels -II An Experimental Survey of Materials Irradiated in a Fast Reactor,"Nucl. Mater, 87, pp. 25-39(1979).

3. Proceedings of the 1971 International Conference on Radiation Induced Voids in Metals, Albany, New York, June 6-11, 1971, U.S. Atomic Energy Commission, April 1972.

4. H. Weidersich, "Theory of Defect Clustering and Void Formation" in Radiation Damage in Metals, pp. 157-191, ASM, Cleveland, 1976.

5. M.L. Bleiberg and J.W. Bennett, Eds., Proceedings of International Conference on the Radiation Effects in Breeder Reactor Structural Materials, June 19-23, 1977, Scottsdale, Arizona, Metallurgical Society of AIME, 1977.

6. R. Bajaj, S. Diamond, M.L. Bleiberg, "Optimization of Precipitation Hardened Fe-Cr-Ni Alloys Using Nickel Ion Bombardment Simulation Studies", in Effects of Radiation on Materials, Eleventh Conference, ASTM-STP-782, H.R. Brager and J.S. Perrin, Eds., American Society for Testing and Materials, pp. 856-884, 1982.

7. S. Wood, J.A. Spitznagel, W.J. Choyke, et al, "Microstructural Development in Dual-Ion Bombarded 316 Stainless Steel", Effects of Radiation on Materials: Tenth Conference, ASTM-STP-725, David Kramer, H.R. Brager and J.S. Perrin, Eds., American Society for Testing and Materials, pp. 455-469, 1981.

8. W.G. Johnston, T. Lauritzen, J.H. Rosolowski et al, "The Effect of Metallurgical Variables on Void Swelling", in Radiation Damage in Metals, pp. 227-266, ASTM Cleveland, Ohio, 1976.

9. M.L. Bleiberg, R. Bajaj, I.M. Baron, et al., "Swelling and Gamma-Prime Particle Stability of Ion-Bombarded Iron-Chromium Nickel Alloys", in Irradiation Effects on the Microstructure and Properties of Metal, ASTM-STP-611, American Society for Testing and Materials, pp. 315-336, 1976.

10. W.J. Weber, G.L. Kulcinski, R.G. Lott, et al., "Ion Simulation Study of Void Formation in High Purity Vanadium", in Radiation Effects and Tritium Technology for Fusion Reactors, CONF-750989, pp. I-130-149, March 1976.

11. S.C. Agarwal and A. Taylor, "Dose Dependence of Void Swelling in Vanadium Irradiated with Self Ions", in Radiation Effects and Tritium Technology for Fusion Reactors, CONF-750989, pp. I-150-157, March 1976.

12. S.C. Agarwal, D.I. Potter and A. Taylor, "Effect of Interstitial Solutes on the Microstructures of Self Ion Irradiated Vanadium", in <u>Irradiation Effects on the Microstructure and Properties of Metals, ASTM-STP-611</u>, American Society for Testing and Materials, pp. 298-311, 1976.

13. A.T. Santhanam, A. Taylor and S.D. Harkness, "Charged Particle Simulation Studies of Vanadium and Vanadium Alloys", in <u>Defects and Defect Cluster in B.C.C. Metals and Their Alloys</u>", R.J. Arsenault Ed., pp. 302-320,1973.

14. R.G. Lott, G.L. Kulchisni, P. Wilkes et al, "Effect of Nickel and Nitrogen on Void Formation in Ion Bombarded Vanadium," <u>J. Nucl. Mat. 85-86,</u> pp. 751-755 (1979).

15. J. Bressers and W. Van Witzenberg, "The Influence of Oxygen on Void Formation in Neutron Irradiated Vanadium", <u>J. Nucl. Mater., 85-86,</u> pp. 757-761, (1979).

16. S.K. Tyler and P.J. Goodhew, "Helium Bubble Growth in Vanadium", <u>Effects of Radiation on Materials, Tenth Conference ASTM-STP-725,</u> David Kramer, M.R. Broger and J.S. Perrin, Eds. American Society for Testing and Materials, pp 654-662, 1981.

17. W. Van Witzenberg, A. Mastenbrock and J.D. Elen, "The Influence of Preimplanted Helium on the Microstructure of Neutron Irradiated Vanadium," <u>J. Nucl. Mater. 103-104,</u> pp 1187-1192, (1982).

18. R.E. Gold and D.L. Harrod, "Radiation Effects in Vanadium and Vanadium Base Alloys", <u>Int. Met. Rev., 25, Nos. 5 and 6:</u> pp. 232-254, (1980).

19. M.P. Tanaka, E.E. Bloom and J.A. Horak, "Tensile Properties and Microstructure of Helium-Injected and Reactor Irradiated V-20Ti;" <u>J. Nucl. Mater., 103-104,</u> pp. 895-900, (1981).

20. B.A. Loomis and G. Ayrault, "Cavity Formation in Single and Dual-Ion Irradiated V-1 5Cr 5Ti Alloy", in <u>Quarterly Progress Report, Oct-Dec. 1982,</u> DOE/ER-0046/12, pp. 194-205, Feb. 1983.

21. B.A. Loomis, A.T. Taylor, T.E. Klippert, et al.,"Effect of Oxygen Impurity on Void Formation in Ion Bombarded Niobium", in <u>Defects and Defect Clusters in B.C.C. Metals and Their Alloys,</u> R.J. Arsenault Ed., pp. 332-340, 1973.

22. B.A. Loomis, A.T. Taylor and S.B. Gerber, "Void Swelling of Nb, Nb-1AT%Zr and Nb-0.5At%O Induced by ^{58}Ni$^+$ Bombardment", <u>Radiation Effects and Tritium Technology for Fusion Reactors,</u> CONF-750989-P1, pp. I-93-105, March 1976.

23. B.A. Loomis and S.B. Gerber, "Swelling of $^{58}Ni^+$ and $^3He^+$ Ion-Irradiated Nb and Nb Alloys", J. Nucl. Mater. 103-104, pp. 1193-1197 (1982) and "Similar Dependence on Dilute O Concentration of Void Formation in Ion-Irradiated Nb and Some Properties of Unirradiated Nb", J. Nucl. Mater, 97, pp. 113-125, 1981.

24. H. Jang and J. Moteff, "The Influence of Neutron Irradiation Temperature on the Void Characteristics of Nb and Nb-1/Zirconium Alloy", Radiation Effects and Tritium Technology for Fusion Reactors, CONF-750989-P1, pp. I-106-121, March 1976.

25. A.F. Bartlett J.H. Evans, B.L. Eyre, et al. "High Temperature Irradiation Damage Structures in Fast Reactor Irradiated Niobium and Vanadium Alloys", in Radiation Effects and Tritium Technology for Fusion Reactors, CONF-750989-P1, pp. I-122-129, March 1976.

26. F.W. Wiffen, "The Microstructure and Swelling of Neutron Irradiated Tantalum", J. Nucl. Mater., 67, pp. 119-130 (1977).

27. J.F. Bates and A.L. Pitner, "Dimensional Stability of Tantalum Control Rods in LMFBRS", Nucl. Technol., 16, pp. 406-409 (1972).

28. R.A. Murgatroyd, I.P. Bell, and J.T. Bland, "Dimensional Stability of Tantalum During Fast Neutron Irradiation", in Properties of Reactor Structure Alloys After Neutron or Particle Irradiation, ASTM, STP 570, American Society for Testing and Materials, pp. 421-432, 1975.

29. F. W. Wiffen, "Swelling of Irradiated Tantalum and Tantalum Alloys," in Quarterly Prog. Report Irradiation Effects on Reactor Structural Materials, Aug-Oct. 1972, HEDL-TME-72-144, Dec. 1972.

30. J. L. Brimhall and E. P. Simonen, "Microstructure of Ion Bombarded Single Crystal Molybdenum", in Defects and Defect Clusters in B.C.C Metals and Their Alloys, R.J. Arsenault Ed., pp. 321-331, 1973.

31. E. P. Simonen and J. L. Brimhall, "The Dependence of Swelling on Void Surface Reaction Rate Constants", in Fundamental Aspects of Radiation Damage in Metals, CONF-751006-P2, Vol. II. pp 1196-1202, (1973).

32. E. R. Bradley and J. L. Brimhall, "The Effect of the Free Surface on Void Formation in Ion Bombarded Molybdenum," in Radiation Effects and Tritium Technology for Fusion Reactors, CONF-750989-P1, pp. I-337-351 March 1976.

33. J. L. Brimhall, L. A. Chariot and H. E. Kissinger, "Effect of He on the Swelling/Microstructure Produced in Mo by Ion Bombardment," J. Nucl. Mater., 85-86, pp. 731-734, (1979).

34. K. Y. Liou, P. Wilkes, G. L. Kulcinski et al, "Void Swelling and Phase In Stability in Heavy Ion Irradiated Mo-Zr Alloy" J. Nucl. Mater., 85-86, pp. 735-738, (1979).

35. J. H. Stubbins and J. Moteff, "Swelling Behavior of Mo-0.5Ti and TZM Bombarded with Heavy Ions at Temperatures Between 750 and 1450°C", J. Nucl. Mater. 103-104, pp. 1163-1168 (1981).

36. J. Bentley, B. L. Eyre and M. H. Loretto, "High Temperature Neutron Irradiation Damage in Molybdenum," in Fundamental Aspects of Radiation Damage in Metals, CONF-751006-P2, pp. 925-931, (1973).

37. J. Bentley, B. L. Eyre and M. H. Loretto, "Suppression of Void Formation in Neutron Irradiated TZM", in Radiation Effects and Tritium Technology for Fusion Reactors, CONF-750989-P1, pp. I-297-322 March 1976.

38. A. G. Pard and K. R. Garr, "Damage Structure in Neutron Irradiated TZM", in Radiation Effects and Tritium Technology fr Fusion Reactors, CONF-750989P1, pp. I-312-322, March 1976.

39. J.A. Sprague, F.A.Smidt, Jr., and J.R. Reed, "The Microstructure of Some Refractory Metals and Alloys Following Neutron Irradiation at 650°C," J. Nucl. Mater., 85-86, pp. 739-743 (1979).

40. D. S. Gelles, D. T. Peterson and J. F. Bates, "Void Swelling in Molybdenum Alloy TZM Irradiated to High Fluence", J. Nucl. Mater., 103-104, pp. 1141-1146, (1981).

41. J. Matolich, H. Nahm and J. Moteff, "Swelling in Neutron Irradiated Tungsten and Tungsten-25 Percent Rhenium," Scripta Met. 8, pp. 837-842 (1974).

42. R. K. Williams, F.W. Wiffen, J. Bentley, et al, "Irradiation Induced Precipitation in Tungsten Based W-Re Alloys", Met. Trans. 14A, pp. 655-666 (1983).

43. F. W. Wiffen, Proceedings of the Symposium on Refractory Alloy Technology for Space Nuclear Power Applications, Oak Ridge, Tennessee, Aug. 1983, R. H. Cooper, Jr., and E. E. Hoffman Eds. pp. 252-277, Jan. 1984.

44. J. L. Katz and H. Wiedersich, "Nucleation of Voids in Materials Supersaturated with Vacancies and Interstitials", J. Chem. Phys. 55, pp. 1414-1425, (1971).

45. K. C. Russell, "Nucleation of Voids in Irradiated Metals", Acta Met. 19, pp. 753-758, (1971).

46. J. J. Burton, "Effect of Mobile Interstitials on the Nucleation of Voids", Scripta Met. 5, pp. 449-458, (1971).

47. M. R. Hayns, "The Nucleation and Early Growth of Interstitial Dislocation Loops in Irradiated Materials", J. Nucl. Mater. 56, 267-274, (1975).

48. B. O. Hall, "Point Defect Clustering During Irradiation", J. Nucl. Mater. 91, pp. 63-72, (1980).

49. H. Wiedersich, "On the Theory of Void Formation During Irradiation", Rad. Effects 12, pp. 111-125, (1972).

50. A. D. Brailsford and R. Bullough, "The Rate of Swelling Due to Void Growth In Irradiated Metals", J. Nucl. Mater. 44, pp. 121-135, (1972).

51. B. O. Hall, "Helium Partioning Between Voids and Dislocations", J. Nucl. Mater., 117, pp. 89-95 (1983).

52. W. G. Wolfer and M. Ashkin, "Diffusion, Vacancies and Interstitials to Edge Dislocations", J. Appl. Phys. 47, pp. 791-800, (1976).

53. P. T. Heald, "The Preferential Trapping of Interstitials at Dislocations", Phil. Mag. 31, pp. 551-558, (1975).

54. A. D. Brailsford, R. Bullough and M. R. Hayns, "Point Defect Sink Strengths and Voids Swelling", J. Nucl. Mater. 60, pp. 246-256, (1976).

55. R. Bullough, M. R. Hayns, and C. H. Woo, "The Sink Strengths of Dislocation Loops and Their Growth in Irradiated Materials", J. Nucl. Mater. 84, pp. 93-100, (1979).

56. F. A. Nichols, "Bias Factors for Use in Reaction-Rate-Theory Analysis of Void Swelling and Radiation Creep", Rad. Effects 39, pp. 169-175, (1978).

57. F. A. Nichols, "Bias Factors for Radiation Creep, Growth and Swelling", J. Nucl. Mater. 90, pp. 29-43, (1980).

58. M.E. Downey and B.L. Eyre, "Neutron Irradiation Damage in Molybdenum," Phil. Mag. 11, pp. 53-80, (1965).

59. B. L. Eyre, D. M. Maher, and A. F. Bartlett, "Neutron Irradiation Damage in Molybdenum", Phil. Mag. 23, pp. 439-465, (1971).

60. K. Shiraishi, K. Fukaya, and Y. Katano, "Radiation and Anneal Hardening in Neutron-Irradiated Vanadium", J. Nucl. Mater. 54, pp. 275-285, (1974).

61. J. Narayan and S. M. Ohr, "The Characteristics of 15 MeV and Fission Neutron Damage in Niobium", J. Nucl. Mater. 63, pp. 454-459, (1976).

62. E. A. Little and B. L. Eyre, "The Geometry of Dislocation Loops Generated in Alpha-Iron by 1-MeV Electron Irradiation at 550°C, "J. Microscopy 97, pp. 107-111, (1973).

63. E. A. Little, R. Bullough, and M. H. Wood, "On the Swelling Resistance of Ferritic Steels", Proc Royal Soc. London A, 372, pp. 565-579 (1980).

64. B. L. Eyre and R. Bullough, "On the Formation of Interstitial Loops in BCC Metals," Phil. Mag. 8, #12, pp. 31-39, (1965).

65. R. Bullough and R. C. Perrin, "The Morphology of Interstitial Aggregates in Iron," Proc. Roy. Soc. London A,305 pp. 541-552, (1968).

66. D. J. Bacon and A. G. Crocker, "The Elastic Energies of Dislocation Loops, in "Lattice Defects in Quenched Metals, R. M. J. Cotterill, M. Koyama, J. J. Jackson, and M. Meshii, eds.) (Academic Press, New York, 1965, pp. 667-678.

67. K. C. Russell, "Thermodynamics of Gas Containing Voids in Metals", Acta Met. 20, pp. 899-907, (1972).

68. J. L. Katz and H. Wiedersich, "Effect of Insoluble Gas Molecules on Nucleation of Voids in Materials Supersaturated with Both Vacancies and Interstitials", J. Nucl. Mater. 45, pp. 41-45, (1973).

69. J. A. Spitznagel, S. Wood and N.J. Doyle, et al., "Helium Partioning to Extended Defects in Dual Ion Bombarded 304 and 316SS", J. Nucl. Mater. 103-104, pp. 1463-1468, (1981).

70. B. O. Hall, "Trap Theory of Helium Partioning at Low Doses", J. Nucl. Mater. 103-104, pp. 1391-1396, (1981).

71. P.R. Okamoto, N.Q. Lam, and H. Wiedersich, "Effects of Defect Trapping and Radiation-Induced Segregation on Void Swelling", in Proc. of Workshop on Correlation of Neutron and Charged-Particle Damage, CONF-760673, pp. 111-146, (1973).

72. H. Wiedersich, P. R. Okamoto, and N. Q. Lam, "Solute Segregation During Irradiation", in Radiation Effects in Breeder Reactor Structural Materials, M. L. Bleiberg and J. W. Bennett, Eds. pp. 801, The Metallurgical Society of AIME, 1977.

73. B. O. Hall and D. I. Potter, "Microstructural Development During Low Dose Irradiation" in Effects of Radiation on Structural Materials, ASTM-STP-683, J.A. Sprague and D. Kramer, Eds. pp-32-45 (1978)

74. A. C. Hindmarsh, "GEAR: Ordinary Differential Equation System Solver," UCID-3001 (Rev. 3), December 1974.

75. C. Kittell, Introduction to Solid State Physics, 3r ed. Wiley London, p. 29, 1968.

76. J.P. Hirth and J. Lothe, Theory of Dislocations, McGraw Hill, New York, p. 762, 1968.

77. R.W. Balluffi, "Vacancy Defect Mobilities and Binding Energies Obtained from Annealing Studies", J. Nucl. Mater., 69-70, pp. 240-263, 1978.

78. N.L. Peterson, "Self Diffusion in Pure Metals", J. Nucl. Mater., 69-70, pp. 3-37, 1978.

79. F.W. Young, Jr., "Interstitial Mobility and Interactions," J. Nucl. Mater., 69-70, pp. 310-330, 1978.

80. D.J. Reed, "A Review of Recent Theoretical Developments in the Understanding of the Migration of Helium in Metals and Its Interaction with Lattice Defects," Rad. Effects, 31, pp. 129-147, 1977.

81. M. H. Yoo and J. O. Stiegler, "Growth Kinetics and Preference Factor of Frank Loops in Nickel During Electron Irradiation", Phil. Mag. 36, pp. 1305-1315, (1977).

82. R. Bullough, B. L. Eyre, and R. C. Perrin, "The Growth and Stability of Voids in Irradiated Metals", Nucl. Applic. Technol. 9, pp. 346-355, (1970).

83. W. G. Wolfer, "Correlation of Radiation Creep Theory With Experimental Evidence," J. Nucl. Mater, 90, pp. 175-192 (1979).

84. J. T. Buswell and S. B. Fisher, "Interstitial Loop Growth in Electron Irradiated Vacuum-Remelted FV448," CEGB-RD-B-N-4564, May 1979.

85. ASTM Proposed New Standard Recommended Practice for Neutron Radiation Damage Simulation by Charged Particle Irradiation Part II. Post Irradiation Examination (1975).

86. J. A. Spitznagel, S. Wood, and W. J. Choyke, "Irradiation Response of Materials", Damage Analysis and Fundamental Studies, Quarterly Progress Report, DOE/0046-April-June 1980, pp. 103-114, August 1980.

87. J.A. Spitznagel, Westinghouse Research and Development Center, Unpulbished Work 1980.

88. J. Greggi, Westinghouse Research and Development Center, Private Communication, 1984.

89. B.A. Loomis, A. Taylor and S.B. Gerber, "Void Swelling of Nb and Nb-1% Zr Induced by ^{58}Ni$^+$ Bombardment," J. Nucl. Mater., 56, pp. 25-37, 1975.

90. L. L. Horton, "Experimental Determination of the Critical Cavity Radius in Fe-10% Cr For Ion Irradiation" CONF-840848-6, pp. 6-7, 1984.

12.0 ACKNOWLEDGEMENTS

1. **SECURITY CLASSIFICATION:** None

2. **REPORT NO.:** WAESD-TR-85-005

3. **PROPRIETARY CLASS:** None

4. **AVAILABILITY:** AESD-WM Library

5. **ORIGINATING SOURCE:** AESD-L

6. **CONTRACT NO.:** F49620-83-C-0120

7. **FUNDING SOURCE:** Air Force Office of Scientific Research

8. **NOTES:**

9. **AUTHOR(S):** R. Bajaj

10. **TITLE:** An Investigation of Irradiation Swelling Mechanisms in Refractory Metals at High Temperatures

11. **DATE--YYMMDD:** 850131

12. **PAGES, REF., ILLUS.:**

13. **DOCUMENT TYPE:** Report

14. **KEYWORDS:** Irradiation, Swelling, Refractory Metals, Niobium

15. **ABSTRACT--PURPOSE, SCOPE, APPROACH, RESULTS, CONCLUSIONS, SIGNIFICANCE:**
(MAXIMUM: 200 WORDS)

The objective of this work is to achieve an understanding of the elevated temperature swelling of refractory metals by a close coupling of theory and experimentation. A theoretical swelling model based on chemical reaction rate formalism was developed, specifically for bcc metals and calculations were performed for niobium.

A special source was developed at ANL which produced Nb ions of sufficient energy and flux level to permit self-ion irradiation of Nb. A series of irradiations was performed at the ANL Accelerator Facility. Swelling was observed, at a nominal dose of 50 dpa, between 700°C and 1200°C with a peak of about 7% at 900°C. Comparison of the data with published work using Ni ions suggests that the published results may have been influenced by chemical action of the Ni atoms.

Comparison of data with the theoretical model suggests a strong influence of oxygen.

DOCUMENT DISTRIBUTION LIST

INTERNAL AESD				EXTERNAL AESD		
NAME, DEPT. LOCATION	FULL TEXT*	RSF ONLY+	COPY NO.●	NAME AND ADDRESS	NO. OF COPIES	COPY NO.●
R. Bajaj Tech. L	5			Major Henry Pugh, Jr.	16	
S. Shiels Tech. L	1			AFOSR/NP		
M. Bleiberg Tech. L	3			Directorate of Physical &		
R. Buckman Tech. L	1			Geophysical Science		
A. Boltax Tech. L	1			Building 410		
R. Morgan Nuc Pro WM	1			Bolling AFB, DC 20332		
P. French Mrktg. WM	1			B.O. Hall WR&D	5	
Library WM	3			G.R. Fenske	5	
				Argonne National Lab		
				9700 S. Cass Avenue		
				Argonne, IL		

* INDICATE NUMBER OF COPIES OF FULL TEXT

+ REPORT SUMMARY FORM ONLY

● CONTROLLED DISTRIBUTION, IF APPLICABLE

END

FILMED

7-85

DTIC